

©2009

MATTHEW DAVID TREISER

ALL RIGHTS RESERVED

PROFILING OF CELL-SUBSTRATE INTERACTIONS USING SINGLE CELL
FLUOROREPORTER IMAGING & MODELING

By

MATTHEW DAVID TREISER

A Dissertation submitted to the

Graduate School-New Brunswick

Rutgers, The State University of New Jersey

University of Medicine and Dentistry of New Jersey

Graduate School of Biomedical Sciences

in partial fulfillment of the requirements

for the degree of

Doctor of Philosophy

Graduate Program in Biomedical Engineering

written under the direction of

Joachim Kohn and Prabhas V. Moghe

and approved by

New Brunswick, New Jersey

October, 2009

ABSTRACT OF THE DISSERTATION

PROFILING OF CELL-SUBSTRATE INTERACTIONS USING SINGLE CELL FLUOROREPORTER IMAGING & MODELING

By MATTHEW DAVID TREISER

Dissertation Directors:

Joachim Kohn and Prabhas V. Moghe

This dissertation advances the field of biomaterials-based tissue engineering via the development of a single cell imaging approach to profile and predict cellular responses. The methodology at the core of the dissertation characterizes cellular behaviors via the extraction and quantification of cell shape, intensity, textural and spatial distribution features of molecular fluororeporters, referred to as high-content cell imaging.

First, we highlight the use of high-content imaging of cell-based fluororeporters to establish and correlate quantifiable metrics of intracellular cytoskeletal features (e.g., descriptors of actin organization) on a set of model biomaterial substrates. The high-content imaging approach is then applied to spatially graded polymer blend substrates of both continuous roughness and discrete chemical compositions in parallel with high-throughput analyses. The imaging approach allowed us to identify the "global" and "high content" structure-

property relationships between cell adhesion and biomaterial properties such as polymer chemistry and topography. The approach also identifies features of the actin-based cytoskeleton that respond to minute chemical modifications of the polymer backbone of a combinatorially derived library. In combination with decision tree and artificial neural network analyses, these 24-hour descriptors are used to predict 3-week material-mediated mineralization.

The high-content imaging approach is complemented with multi-dimensional scaling (MDS) modeling efforts to project amplified variations in cytoskeletal organization that forecast human mesenchymal stem cell lineage commitment before it is detected via traditional assays. Utilizing early quantitative measures of cytoskeletal morphology (morphometrics) and MDS allows the identification of distinct subpopulations of stem cells that emerge from non-linear combinations of cell shape, texture, density and cytoskeletal organizational features. These clusters allow the prediction of long-term differentiation behaviors of stem cells that manifest days to weeks later than the time of morphometric analysis. The proposed platform represents an ideal approach to probe cell-responses to complex microenvironments as it provides: real time measures of stem cell fates and material induced cell responses, cell-by-cell based analysis that captures the heterogeneity of sample populations, and the ability to parse out lineage commitment in stem cells resulting from multiple stimuli.

Acknowledgment

First and foremost I would like to express my great appreciation to my two mentors, Drs. Joachim Kohn and Prabhas Moghe. Without their constant guidance, scientific input, recommendations and, most importantly, faith, none of this would have been possible. Under their tutelage I have learned the art of being a fundamental scientist and the science behind the art of medicine. I am most appreciative that as mentors they have provided me with role models that I strive to someday emulate, as lofty a goal as that may seem. Acknowledgment is also warranted to Simon Gordonov, whose diligence and dedication to the project surpassed my highest expectations. I would like to thank all members of the Kohn and Moghe groups past and present. While too numerous to be named individually, their contributions to my success cannot be overstated. To those administrators who, at times, I am sure I drove to edge of insanity, I hope you realize it was only because I enjoyed the company. Kathy Piano, Melissa Aranzamendez, Linda Anthony, Julia Haque and, most importantly, Perry Dominguez, thank you for your tireless efforts in helping me navigate the bureaucratic waters that I so often felt were minutes from drowning me. To Drs. Kinzy and Shreiber, I thank you for the mentorship and outside perspective when I needed it most. Our conversations often offered me peace of mind, and in that respect I would acknowledge your mentorship, but more so your friendship. To Gary Monteiro and Shirley Masand, simply, thank you. At the best of times you made the process fun, and at the worst of times, bearable. To my family who relentlessly reminded me that light at the end of the tunnel was not the train

coming to get me. Arlene Lebovic, Diana Kogan, Jessica Kogan, Mia Kogan and Israel Kogan, without your love and support I would truly be lost, or worse, a lawyer. To my brother the lawyer, thank you for being the best brother a man could ever ask. Few people are lucky enough to admit that their brother is also their best friend; I am truly one of those few. To this day it still amazes me that my weakest attributes only seem so weak when compared to the lack of yours. I am glad that there was someone in my life to remind me that every life needs a little bit of fun and self-indulgence. To my parents, words cannot and never will describe your impact in my life. First, thank you for the funding. Truly no institution has supported this work more than the Susan and Murray Treiser lifetime scholarship fund. Few parents would be as supportive of a child's lifelong endeavor to remain a student permanently. All that I am and will ever be is because of your love, dedication, confidence, honesty and hard work. I thank you for lifting me up in the lows and lifting me higher in the highs. Last but not least, to Jenevieve Duron. You are evidence that sometimes the best parts in yourself are only visualized through the eyes of another. Through nine years you have been there every step of the way. Although you may feel that your contributions are often minimized, I promise you that they were not, are not and never will be. Thank you.

Dedication

Pigmaei gigantum humeris impositi plusquam ipsi gigantes vident

-Sir Isaac Newton (1676)

This dissertation is dedicated to those “giants” upon whose shoulders I have stood all my life. To my grandparents who lifted us all above a past filled with horrors beyond imagining, it is within the mold of your diligence to provide, your refusal to fail, and your relentless pursuit of perfection that I have tried to live. For the opportunity I was afforded that you never were, I dedicate this dissertation to you. To my parents, I do not share but gift this work as a tribute to your tireless and endless efforts to raise a son that brings you pride. Finally, to my Zeidi, we began this journey together, but as is life, I must finish it alone. Every step I take I keep your embrace in my heart and your voice in my ear. Never has a man been more righteous, loving or honest. For these reasons and more, I hope that this small token of appreciation can somewhat settle the endless debt of gratitude of which you are all owed.

It is not the critic who counts, nor the man who points how the strong man stumbled or where the doer of deeds could have done them better. The credit belongs to the man who is actually in the arena; whose face is marred by dust and sweat and blood; who strives valiantly...who knows the great enthusiasms, the great devotions, and spends himself in a worthy cause; who, at best, knows the triumph of high achievement; and who, at the worst, if he fails, at least fails while daring greatly, so that his place shall never be with those cold and timid souls who know neither victory nor defeat.

-Theodore Roosevelt (1910)

Table of Contents

ABSTRACT OF THE DISSERTATION	ii
ACKNOWLEDGMENT	iv
DEDICATION	vi
TABLE OF CONTENTS	viii
LIST OF TABLES	xi
LIST OF FIGURES	xii
1 INTRODUCTION	1
1.1 TISSUE ENGINEERING AND REGENERATIVE MEDICINE – THE NEED FOR NEW TOOLS TO DEFINE STRUCTURE-FUNCTION RELATIONSHIPS	1
1.2 MESENCHYMAL STEM CELLS FOR TISSUE ENGINEERING	9
1.3 A NEED FOR RATIONALLY DESIGNED NOVEL POLYMERS	19
1.4 THE NEED FOR HIGH-THROUGHPUT AND HIGH-CONTENT SCREENING OF CELL-BIOMATERIAL INTERACTIONS	21
1.5 THE CYTOSKELETON AS A REGULATOR OF CELL BEHAVIOR	24
1.6 HYPOTHESIS AND AIMS OF THE DISSERTATION	29
2 DEVELOPMENT OF A “HIGH-CONTENT” IMAGING PLATFORM FOR STUDYING CELL-MATERIAL INTERACTIONS	31
2.1 INTRODUCTION	31
2.2 MATERIALS AND METHODS	33
2.2.1 POLYMER SYNTHESIS AND FABRICATION	33
2.2.2 CELL CULTURE AND TRANSFECTION	36
2.2.3 IMAGING	38
2.2.4 MORPHOMETRIC ANALYSIS	38
2.2.5 APOPTOSIS STUDIES	41
2.2.6 STATISTICAL ANALYSIS	41
2.3 RESULTS	42
2.3.1 BIOMATERIALS-RESPONSIVE CELL GFP REPORTERS	42
2.3.2 "HEAT MAP" REPRESENTATION OF CELL DESCRIPTORS FOR COMBINATORIAL BIOMATERIALS	45
2.3.3 MORPHOMETRIC DESCRIPTORS OF CELL FUNCTIONAL FATES ON BIOMATERIALS	48
2.4 DISCUSSION:	50
2.5 CONCLUSION:	56

3 HIGH-CONTENT PROFILING OF CELL RESPONSIVENESS TO GRADED SUBSTRATES BASED ON COMBINATORIALLY VARIANT POLYMERS.

57

3.1 INTRODUCTION	57
3.2 MATERIALS AND METHODS	61
3.2.1 POLYMER SYNTHESIS AND GRADIENT FABRICATION	61
3.2.2 ANNEALING GRADIENT PREPARATION	61
3.2.3 ATOMIC FORCE MICROSCOPY (AFM)	62
CELL CULTURE AND TRANSFECTION.	65
3.2.4 CONFOCAL MICROSCOPY AND IMAGING	66
3.2.5 DEGREE OF CELL ATTACHMENT	67
3.2.6 DEGREE OF CELL ADHESION STRENGTH	67
3.2.7 GFP-FARNESYLATION BASED MORPHOMETRIC DESCRIPTORS OF SINGLE CELLS	68
3.2.8 STATISTICAL ANALYSIS	69
3.3 RESULTS AND DISCUSSION	70
3.3.1 TWO-DIMENSIONAL GRADIENT FABRICATION	70
3.3.2 CELLULAR ATTACHMENT AND ADHESION EVALUATION	74
3.3.3 HIGH-CONTENT SINGLE CELL IMAGING ON SUBSTRATES WITH ROUGHNESS GRADIENTS	81
3.4 CONCLUSION	91

4 HIGH-CONTENT IMAGING OF SAOS-2 RESPONSE TO TYROSINE-DERIVED POLYCARBONATES

92

4.1 INTRODUCTION	92
4.2 MATERIALS AND METHODS	96
4.2.1 POLYMER NOMENCLATURE	96
4.2.2 DESIGN OF COMBINATORIAL POLYMER LIBRARY	96
4.2.3 PREPARATION OF SPIN-COATED POLYMER FILMS	99
4.2.4 CULTURE OF SAOS-2 CELLS ON POLYMER COATED GLASS SUBSTRATES	99
4.2.5 DETERMINATION OF SAOS-2 CELL PROLIFERATION	100
4.2.6 DETERMINATION OF SAOS-2 CELL MINERALIZATION ON THE POLYCARBONATES.	100
4.2.7 ENGINEERING OF GREEN FLUORESCENT PROTEIN (GFP) SAOS-2 CELL	101
4.2.8 IMAGING OF ENGINEERED CELLS ON POLYMER FILMS	101
4.2.9 IMAGE PROCESSING	102
4.2.10 DECISION TREE FOR IDENTIFICATION OF MATERIAL RESPONSIVE DESCRIPTORS.	104
4.2.11 ARTIFICIAL NEURAL NETWORK (ANN) TO PREDICT POLYMER INFLUENCED SAOS-2 CELLULAR BEHAVIORS FROM EARLY MORPHOLOGY.	105
4.3 RESULTS	108
4.3.1 PROLIFERATIVE RESPONSE OF SAOS-2 CELLS TO POLYMER FILMS	108
4.3.2 MATERIAL-MEDIATED MINERALIZATION OF SAOS-2 CELLS	110
4.3.3 HIGH-CONTENT IMAGING AND “HEAT MAP” REPRESENTATION OF SAOS-2 CELLS CULTURED ON A COMBINATORIALLY-DERIVED FAMILY OF POLYMERS	112
4.3.4 DECISION TREE MODELING TO PARSE CHEMISTRY RESPONSIVE MORPHOMETRIC DESCRIPTORS	119
4.3.5 COMPUTATIONAL MODELING EFFORTS TO PREDICT 3 WEEK POLYMER-MEDIATED MINERALIZATION BASED ON 24 HOUR HIGH CONTENT MORPHOMETRICS	119
4.4 DISCUSSION	126
4.5 CONCLUSION	135

5	<u>CYTOSKELETON-BASED FORECASTING OF STEM CELL LINEAGE FATES</u>	136
5.1	INTRODUCTION:	136
5.2	MATERIALS AND METHODS:	139
5.2.1	HUMAN MESENCHYMAL STEM CELL CULTURE	139
5.2.2	HMSC DIFFERENTIATION ON FIBRONECTIN-COATED GLASS SUBSTRATES	139
5.2.3	POLYMERASE CHAIN REACTION (PCR) OF HMSCs UNDER INDUCTION MEDIA	140
5.2.4	HIGH-CONTENT IMAGING OF HMSC ON GLASS AND FIBRONECTIN-COATED GLASS	141
5.2.5	COMPUTATIONAL METHODS TO PARSE CYTOSKELETON-ENCODED STEM CELL FATES	141
5.2.6	PREPARATION OF SPIN-COATED POLYMERIC SUBSTRATES	144
5.2.7	HMSC MORPHOMETRICS AND DIFFERENTIATION ON POLYMERIC SUBSTRATES	144
5.3	RESULTS:	149
5.3.1	HMSC ADOPT DISTINCT DIFFERENTIATION OUTCOMES THAT ARE NOT APPARENT FROM EARLY CELL SHAPE/MORPHOLOGY	149
5.3.2	EARLY PCR OF CHARACTERISTIC GENES OF DIFFERENTIATION FAIL TO SHOW DIFFERENCES IN AD VERSUS OS TREATED CELL CULTURES.	150
5.3.3	HIGH CONTENT CYTOSKELETAL IMAGING AND COMPUTATIONAL MODELING YIELD MORPHOLOGICALLY DISTINGUISHABLE STEM CELLS	152
5.3.4	MDS ANALYSIS OF CYTOSKELETAL DESCRIPTORS DISCERNS BONE PRECURSORS WITHIN THE FIRST 24 HOURS	157
5.3.5	CYTOSKELETAL DESCRIPTORS CAPTURE THE SUBSTRATE-GOVERNED TIME EVOLUTION OF LINEAGE COMMITMENT	158
5.3.6	24 H FORECASTING OF HMSC OSTEOBLASTIC LINEAGE OUTCOMES AT TWO WEEKS VIA HIGH CONTENT MORPHOMETRIC DESCRIPTORS	162
5.4	DISCUSSION:	169
5.5	CONCLUSION:	175
6	<u>RESEARCH SUMMARY AND FUTURE DIRECTIONS</u>	176
6.1	RESEARCH SUMMARY	176
6.2	FUTURE DIRECTIONS	180
6.2.1	CYTOSKELETAL DESCRIPTOR PATHWAY ELUCIDATION	180
6.2.2	THREE DIMENSIONAL HIGH-CONTENT DESCRIPTOR CALCULATION	181
6.2.3	ANALYSIS OF OTHER INTRACELLULAR MOLECULES FOR DESCRIPTOR GENERATION	183
7	<u>REFERENCES</u>	186
8	<u>CURRICULUM VITA</u>	212

List of Tables

TABLE 2.1: GFP-BASED PLASMID REPORTERS USED FOR PROFILING CELL-BIOMATERIAL INTERACTIONS	37
TABLE 2.2: DEFINITIONS OF MORPHOMETRIC DESCRIPTORS THAT CAN BE QUANTIFIED FROM THE DIGITIZED IMAGES OF FLUOROREPORTER CELLS ON BIOMATERIALS.	40
TABLE 4.1: LIST OF POLYMERS FOR SAOS-2 HIGH CONTENT STUDY	98
TABLE 4.2: DECISION TREE RESULTS OF TOP 3 SAOS-2 24 HOUR MORPHOMETRIC DESCRIPTORS RELATING TO 3 WEEK MINERALIZATION.	124
TABLE 4.3: SUMMARY OF 10-FOLD CROSS VALIDATION ARTIFICIAL NEURAL NETWORK USED TO PREDICT SAOS-2 3 WEEK MINERALIZATION ON POLYMERS BASED ON SOLELY 24-HOUR ACTIN MORPHOMETRICS.	125
TABLE 5.1: TABLE OF 43 ACTIN FLUOROREPORTER-DEFINED MORPHOMETRIC FEATURES FOR INDIVIDUAL HMSCs.....	145
TABLE 5.2: THE SINGLE CELL MORPHOMETRIC METHODOLOGY CAN BE USED TO ASSESS HMSC DIFFERENTIATION ON A WIDE ARRAY OF BIOMATERIALS.	164

List of Figures

FIGURE 1.1: HUMAN MESENCHYMAL STEM CELL OSTEOBLASTIC DIFFERENTIATION	14
FIGURE 1.2: HUMAN MESENCHYMAL STEM CELL ADIPOCYTIC DIFFERENTIATION	17
FIGURE 1.3: KEY INTERACTIONS OF THE ACTIN CYTOSKELETON WITH SIGNALING MOLECULES THAT GOVERN CELL BEHAVIORS.	28
FIGURE 2.1: CHEMICAL STRUCTURE AND NOMENCLATURE SCHEME FOR TYROSINE DERIVED POLYCARBONATES.....	35
FIGURE 2.2: CONFOCAL MICROGRAPHS OF GFP-ENGINEERED SAOS2 CELLS ON TWO POLYMERIC SUBSTRATES WITH DIFFERENT BACKBONE COMPOSITIONS LEADING TO DIFFERING HYDROPHOBICITIES.	44
FIGURE 2.3: CELL RESPONSES TO A COMBINATORIAL VARIATION IN SUBSTRATE PROPERTIES CAN BE DISCERNED USING HIGH CONTENT IMAGING OF CELL GFP- REPORTERS AND A "HEAT MAP" REPRESENTATION OF VARIATIONS IN MORPHOMETRIC DESCRIPTORS.	46
FIGURE 2.4: MORPHOMETRIC DESCRIPTORS QUANTIFIED FOR CELL FLUORESCENT REPORTERS CAN BE USED TO PROFILE CELL FUNCTIONAL FATE ON BIOMATERIALS, FOR EXAMPLE, CELL APOPTOSIS.....	49
FIGURE 2.5: LIVING CELL REPORTERS OFFER CLEAR ADVANTAGES OVER FIXED CELLS TOWARD EFFECTIVE COMPUTATION OF CELL DESCRIPTORS ON BIOMATERIALS	54
FIGURE 3.1: FABRICATION OF 2D ORTHOGONAL COMPOSITION/ROUGHNESS GRADIENT PLATFORM.....	63
FIGURE 3.2: SURFACE ROUGHNESS CHARACTERIZATION OF GRADIENT SUBSTRATE WITH AFM TAPPING MODE.....	72
FIGURE 3.3: DEGREE OF CELL ADHESION (24 H) WAS PLOTTED VERSUS RMS ROUGHNESS ON THE SUBSTRATES WITH ROUGHNESS GRADIENTS.	77
FIGURE 3.4: CELL ADHESION (24 H) WAS PLOTTED VERSUS THE SPECIFIC GRADIENT STEEPNESS OF ROUGHNESS, AN INDEX THAT CORRECTS FOR VARYING DEGREES OF ROUGHNESS IN DIFFERENT REGIONS OF THE GRADIENT STEEPNESS.	78
FIGURE 3.5: SAOS-2 GFP-F CELL ADHESION FORCE MEASUREMENT USING HIGH THROUGHPUT IMAGING.	79
FIGURE 3.6: NORMALIZED CELL AREA VERSUS ROUGHNESS.	82
FIGURE 3.7: QUANTITATIVE CHARACTERIZATION OF CELL SHAPE DESCRIPTORS AND MORPHOLOGIC EXPRESSION OF GFP-FARNESYLATION USING CELL MORPHOMETRIC DESCRIPTORS.....	88
FIGURE 4.1: SEGMENTATION PROCEDURE TO COMPUTE MORPHOMETRIC DESCRIPTORS OF SAOS-2 CELLS.....	103
FIGURE 4.2: COMPUTATIONAL APPROACH TO HIGH-CONTENT MORPHOMETRIC DESCRIPTOR PREDICTION OF SAOS-2 CELLULAR BEHAVIORS.	107
FIGURE 4.3: SAOS-2 PROLIFERATIVE RESPONSE TO TYROSINE-DERIVED POLYCARBONATES AND POLY(α -HYDROXY ESTER)S.	109
FIGURE 4.4: SAOS-2 3 WEEK MINERALIZATION RESPONSE TO TYROSINE-DERIVED POLYCARBONATES AND POLY(α -HYDROXY ESTER)S.	111
FIGURE 4.5: REPRESENTATIVE CONFOCAL LASER SCANNING MICROSCOPE IMAGES OF EGFP-ACTIN ENGINEERED CELLS ON TYROSINE-DERIVED POLYCARBONATES AND POLY(α -HYDROXY ESTER)S.....	114

FIGURE 4.6: “HEAT-MAP” REPRESENTATION OF THE STATISTICAL DIFFERENCE OF IN MORPHOLOGICAL DESCRIPTOR VALUE AS A RESULT OF CULTURE ON POLYMERS OF DIFFERENT CHEMISTRY.	118
FIGURE 4.7: POLYMER CHEMISTRY RESPONSIVE DESCRIPTORS DETERMINED BY DECISION TREE ANALYSIS.	123
FIGURE 5.1: SCHEMATIC OF MULTI-DIMENSIONAL SCALING (MDS) APPROACH TO SEGMENT CELLS BASED ON ACTIN CYTOSKELETAL ORGANIZATION.	147
FIGURE 5.2: PERFORMING MDS UPON A RANDOM NEGATIVE CONTROL YIELDS NO CLEAR IDENTIFIABLE STRUCTURE.	148
FIGURE 5.3: hMSCs DISPLAY GROWTH FACTOR DEPENDENT DIFFERENTIATION BEHAVIORS AT 2 WEEKS THAT ARE NOT APPARENT AT 24 HOURS.	153
FIGURE 5.4: : hMSCs DISPLAY GROWTH FACTOR DEPENDENT DIFFERENTIATION BEHAVIORS THAT ARE NOT DETECTABLE BY GENE TRANSCRIPTION ANALYSES WITHIN THE FIRST 24 HOURS OF CULTURE.	155
FIGURE 5.5: THE DEVELOPMENT OF DESCRIPTOR-BASED COMPUTATIONAL MODELING APPROACHES TO PARSE hMSCs AT 24 HOURS IN CULTURE.	156
FIGURE 5.6: CYTOSKELETON-BASED DESCRIPTORS SEGMENT AND IDENTIFY INDIVIDUAL OSTEOBLASTIC CELLS WITHIN hMSC CULTURES EXPOSED TO SOLUBLE FACTORS.	159
FIGURE 5.7: CYTOSKELETAL BASED MORPHOMETRIC SEGMENTATION KINETICS OCCUR IN A LIGAND-DEPENDENT MANNER.	161
FIGURE 5.8: ALTERED hMSC OSTEOBLASTIC COMMITMENT RESULTING FROM SUBSTRATE MAY BE PREDICTED BASED ON MDS AT 24 HOURS.	167
FIGURE 5.9: hMSCs CULTURED ON SYNTHETIC/ECM SUBSTRATES DEMONSTRATE TWO SEPARATE DEFINABLE CLUSTERS WITHIN A SINGLE IMAGE.	168

1 INTRODUCTION

1.1 Tissue Engineering and Regenerative Medicine – The Need for New Tools to Define Structure-Function Relationships

Tissue loss and end organ failure present an enormous social and economic strain on the afflicted individuals and society at large. In the United States, the treatment of these patients costs over \$400 billion per year (1) with over 8 million surgical procedures performed annually to treat these disorders (2). While “tissue loss and end organ failure” represents a heterogeneous grouping of pathologic conditions ranging from liver failure to musculoskeletal injury, current surgical interventions often may fail to provide curative solutions. Traditional treatment strategies depend on extracorporeal devices, such as kidney dialysis machines, or operative interventions, such as the allografting of organs from living/cadaveric donors. Although these approaches have provided positive patient outcomes for some, many patients fail to receive viable long-term cures. Mechanical interventions lack adequacy because they treat symptoms of the organ failure, not the failure itself. This requires that patients maintain permanent application of these devices resulting in extreme morbidity and economic loss. For example, in a 2008 survey, over 500,000 patients were diagnosed with end-stage renal disease (ESRD) at a cost of nearly \$23 billion to Medicare with a majority receiving some form of hemodialysis (3). While hemodialysis can provide some relief of the symptoms associated with ESRD, because dialysis cannot recapitulate the entire function of the organ, patients on

hemodialysis have a 5-year survival rate of only 33% in contrast to their transplanted counterparts with a 5-year survival rate of 74% (3). Unfortunately, current transplantation approaches suffer from extreme shortages in donor organs. In 2008, 108,747 patients were listed for organ transplants, while only 12,934 organs were donated (4). Non-transplantation-based surgical reconstructions also frequently fail due to their associated post-operative complications. For example, patients who undergo total hip arthroplasty often suffer from heterotopic ossification (the abnormal formation of bone within extraskeletal soft tissue), which occurs in 50% of patients (5). These numbers demonstrate that current surgical and mechanical interventions fail to provide adequate curative solutions to tissue loss and organ failure. The ideal solution would recreate whole organ function in a corporeal device that is biocompatible and easily integrated into the patient's anatomy.

Tissue engineering and regenerative medicine seek to facilitate the healing of tissues and organs lost to pathological processes via the development of devices/biologics that stimulate, supplement or act in lieu of the body's natural regenerative abilities. The term tissue engineering was defined at an NSF meeting in 1988 as, the "application of the principles and methods of engineering and life sciences toward the fundamental understanding of structure-function relationships in normal and pathological mammalian tissues and the development of biological substitutes for the repair or regeneration of tissue or organ function."(6) Although the terms "tissue engineering" and "regenerative medicine" are often used synonymously, it is important to note that while they

share the same end purpose, the terms imply subtly different approaches. Tissue engineering focuses on the creation and formation of biological substitutes, whereas regenerative medicine seeks to utilize the naturally regenerative properties of cells to repair the body, whether by direct tissue formation or by the release of trophic factors to induce endogenous healing (1, 7). To clarify, regenerative medicine functions by stimulating cells to repair damaged tissue, whereas tissue engineering utilizes engineered constructs to reform solid tissue or organs (8). These strategies are not mutually exclusive, and often a given approach for tissue repair represents a combination of both tissue engineering and regenerative medicine. Proponents of these strategies believe they can address the clinical needs of patients suffering from organ/tissue loss by developing biologically derived constructs that maintain the entire functionality of the original organ. These organs will reduce the need for whole organ donation and surgical repair by providing artificial surrogates that are non-immunogenic and effectively perform the functions of endogenous tissue (9).

Historically, attempts by physicians to artificially induce tissue regeneration date back to 1500 BC (10). These early attempts at nasal reconstruction utilized autologous grafted skin in conjunction with wood scaffolds to reform the nose. In its modern formulation, tissue engineering currently employs three main strategies: (1) implantation of isolated or cultured cells for injection and subsequent healing; (2) in situ directed tissue regeneration; and (3) implantation of ex vivo assembled constructs containing cells and scaffolds (11).

The interest in injectable cell therapies, particularly injectable stem cell therapies, derives from: their avoidance of a surgical procedure and associated complications, the enormous availability of cell sources in the form of aspirates from donors, and the replacement of only damaged tissue rather than whole organs (1). Studies have shown some success in both animal models and clinical applications with this strategy for repair of cardiac function in heart disease (12, 13). However, the true feasibility and effectiveness of this approach remains unclear. While injection of stem cells appears to improve cardiac function, a clinical review published by Collins et al. indicates that few of the injected cells are retained in the heart and that most improvements in cardiac function are more likely a result of stimulated angiogenesis via secreted cytokines than via reparation of cardiac tissue (14). This review highlights some of the greatest criticisms of the injectable approach. First, while some cells may localize to the wound site, the lifetime of those cells and the location and consequences of the remainder of the injected cells within the body remain concerns. Second, the benefit of injecting stem cells may be artifactual, with the greatest benefit derived from secreted soluble factors as opposed to tissue reformation (12). Finally, while this approach may be adequate for the repair of focally damaged tissue, it is not expected to provide restoration of whole organ failure because it is believed that isolated cells cannot themselves form new tissues in the absence of a supporting material (15).

In situ tissue regeneration depends on the ability of the native cells within the body to synergize with an acellular implanted device. This device may be

permanent or degradable, and the material may be natural (e.g., fibrin, gelatin, thrombin, or collagen) (16) or synthetic. In contrast to prostheses where the ultimate goal is to provide an artificial replacement, here the device acts as a scaffold for endogenous cell repair. The scaffold provides the mechanical support necessary to maintain functional form. The material may include bioactive or biomimetic factors to promote cellular attachment, proliferation and/or differentiation thereby increasing tissue regeneration (17-19). In situ tissue engineering devices have shown clinical promise in applications such as sutures (20-23), orthopedic devices (24-29), tissue sealants (30-32), and hernia repair devices (33). Interestingly, most of the work performed involving in situ tissue regeneration focuses on the repair of focal defects in connective tissues (i.e., bone, cartilage, tendons and skin) (34). Investigators focus on focal defects because, in situ, avascular scaffolds only allow cells to penetrate 100 μm due to oxygen diffusion limitations (35). While some work has been attempted to simultaneously promote cell migration and angiogenesis within a scaffold, to date, the creation of micro-vasculature networks in situ remains suboptimal (34). Therefore, in the absence of a previously established vascular network or an angiogenic material, tissue engineering strategies that utilize acellular constructs focus on applications where oxygen diffusion is non-limiting.

The most commonly studied tissue engineering strategy utilizes cells seeded within a porous implant to create a cell-material hybrid (36). In these constructs, cells are isolated from donors (autologous or allogeneic) and seeded onto biomaterial scaffolds in vitro. The cells are cultured on the scaffolds within a

bioreactor until they assemble an organized tissue similar to that of the damaged tissue the device is intended to repair. Once implanted, this artificially engineered organ functions as native tissue. This approach interests researchers because it addresses many of the weaknesses of the other two. Unlike both the injectable and in situ regeneration paradigms, the cell-material hybrid strategy, in theory, allows for the construction of a whole living organ ex vivo. Assembling the tissue ex vivo allows researchers to construct complex structures that mimic the natural biology of endogenous tissue. For example, utilizing micro patterning and machining, vascular networks (37, 38) can be assembled and combined with the cell-material hybrid to provide adequate perfusion of the construct. Additionally, as opposed to in situ differentiation, the ex vivo approach allows for the assembly of spatially controlled tissue analogs of multiple cell types (39) within scaffolds that are seeded uniformly with viable cells (40, 41). Finally, the cell-material hybrid approach allows for the testing of the engineered tissue before implantation to ensure that it functions properly.

Regardless of the strategy, tissue engineering, in its current form, has not delivered as billed. In 1995, US-based market analysts predicted that tissue engineering would generate \$3 billion by 2002. In reality, the total tissue engineering market in 2002 was less than \$50 million (36, 42-44). Recently, the tissue engineering sector underwent increased growth, with \$1.3 billion in sales in mid-2007 (45). However, even with this recent spurt, tissue engineering is still far from reaching its full potential. While many factors contribute to the current inability for tissue engineering to provide “off-the-shelf” tissues, perhaps the

greatest is the lack of fundamental understanding regarding cells, materials and how they interact. Since the two main components of tissue engineered constructs are the cells and scaffolding material, these two factors and their interactions must be understood and optimized to maximize the efficacy of the approach (11). A 2007 study performed by Johnson et al. surveyed 24 leaders of the tissue engineering field to determine the best paths to obtain clinically viable products (46). Their findings indicated that one of the most needed areas is the understanding and control of stem cell behavior by measuring responses at the molecular level. Using these structure-function responses of stem cells probed at the molecular level may enable the identification of biomarkers for guidance in the design of tissue engineered products. To that end, a strategic assessment of the field from the MATES group of federal agencies provides a list of the critical priorities to identify these structure-function-relationships, some of which are listed here: “(1) understanding the cellular machinery; (2) identifying, validating biomarker and assays; (3) advancing imaging technologies; (4) defining cell/environment interactions; and (5) establishing computational modeling systems” (47). The MATES assessment indicates that these 5 priorities, along with those not listed here, are essential to accomplishing what they consider the 4 overarching goals of the field: (1) understanding and controlling the cellular response; (2) formulating biomaterial scaffolds and the tissue matrix environment; (3) developing enabling tools (i.e., high-throughput assays, instrumentation, imaging modalities, and computational modeling); (4) promoting scale-up, translation and commercialization” (46, 47). This dissertation seeks to

address these goals and priorities via the development of a novel methodology to characterize stem cell response to biomaterials for their use in tissue engineering strategies. This will be accomplished via high content, imaging-based profiling that: captures quantitative information of stem cell whole cell and cytoskeletal morphology; uses computational models to predict long-term differentiation behaviors of stem cells; and correlates stem cell interactions with the application of soluble factors and tailored biomaterials.

1.2 Mesenchymal Stem Cells for Tissue Engineering

Fully differentiated somatic cells and stem cells represent the two most commonly used cell sources for tissue engineering. Somatic cells demonstrate the potential for tissue regeneration when seeded in artificial scaffolds. Examination of review articles within the literature shows that these cells have been applied in organs such as cartilage (48), the pancreas (49), bone (50), skin (51), and liver (52). While these reviews highlight the potential terminally differentiated cells provide, these cells suffer from difficulty in balancing differentiation with proliferative ability (53). Cell proliferation provides the cell numbers that are critical for tissue construction. Ideally, a small amount of donor cells expand to homogenously populate the scaffold. Unfortunately, as explained by Strehl and coauthors, terminally differentiated somatic cells often lose their ability of self-renewal. While methods exist to reinitiate cell proliferation in these cells, this process may result in the down regulation of differentiation behaviors. In an attempt to find a cell source that maintains both proliferative and differentiation potentials, researchers have turned to stem cells. Stem cells are pluripotent cells (i.e., have the ability to differentiate into a number of terminal cell types) that display self-renewal in their stem-like states. These stem cells may be isolated from human embryonic tissues (54), or from niches within adult tissues such as but not limited to the bone marrow (55-57), liver (58, 59), the skin (60, 61), adipose tissue (62, 63) and the brain (64-66). This dissertation focuses on adult stem cells.

Although adult stem cells can be derived from a number of tissues, the most extensively used in cell-therapies are those derived from the bone marrow, also known as human mesenchymal stem cells (8). Human mesenchymal stem cells (hMSCs) have gained interest in the scientific community because of their pluripotency, specifically their ability to differentiate into a multitude of cell phenotypes including but not limited to: smooth muscle cells, chondrocytes, osteoblasts and adipocytes (56, 67-69). Bone marrow aspirates from donors provide a readily available supply of these stem cells, with a number of isolation and propagation procedures to enrich this population (70). hMSCs are a self-renewing cell population allowing for their use in tissue engineering strategies that utilize the ex vivo expansion and seeding of cells onto scaffold materials intended for implantation. However, the successful creation of constructs that integrate scaffold materials and hMSCs requires the expression of the appropriate differentiated cellular phenotypes post-seeding.

Perhaps one of the most investigated cell phenotypes of hMSCs is the osteoblastic. The process of osteoblastic differentiation is believed to proceed largely via stimulation with soluble factors (**Fig. 1.1**). In vitro, osteogenic induction of hMSCs is generally achieved via application of media containing dexamethasone, ascorbate and β -glycerophosphate (DAG). This combination of soluble factors can achieve high levels of bone differentiation when applied to hMSC seeded at low seeding densities (68, 71). It is believed that osteoblastogenesis proceeds via transcription and subsequent activation of the osteoblast specific core binding factor $\alpha 1$ (Cbfa1), also commonly referred to in

the literature as runt-related transcription factor 2 (RUNX2). (72, 73). Cbfa1 is the earliest and most specific marker of osteoblastogenesis and induces cells to produce type I collagen and alkaline phosphatase, both early markers of osteoblastic differentiation signifying the preosteoblastic stage (74-76). The expression of alkaline phosphatase, type I collagen and the markers of a mature osteoblast (i.e., osteocalcin, mineral, and other non-collagenous proteins) are linked to the expression of distal-less 5 (Dlx-5), which acts as a transcription factor (77-79). This transcription factor promotes the transcription of osterix (OSX) (80), which along with Cbfa1 are the main determinants of osteoblastogenesis (72, 81). Osteoblastogenesis has also been shown to act via the Wnt/ β -catenin pathway via differentiation of precursor cells to the early but not late osteoblastic phenotype (82-85). While soluble factors play a dominant role in osteoblastogenesis, they are not the only signals involved. Cell adhesion molecules such as integrins, selectins, cadherins, and the RGD binding sequence found in collagen, fibronectin, osteopontin, thrombospondin, bone sialoproteins, and vitronectin have all been shown to be required for differentiation (86-88). Finally, material mechanics can influence stem cell differentiation towards the osteoblastic phenotype, with the greatest osteoblastogenesis occurring when hMSCs are cultured on stiffer materials (89, 90). Thus, the production of osteoblasts from a MSC is a complicated and robust process requiring a number of chemical and mechanical cues.

Another hMSC terminal cell phenotype commonly examined in the literature is the adipocytic lineage. The interest in this lineage stems from its

relevance to disease models for obesity, diabetes, and other lipodystrophic disorders (91), as well as its relationship with the osteoblastic lineage as a model of general stem cell behavior. MSCs in both human and animal models demonstrate that molecular changes involved in adipogenesis inhibit osteoblastogenesis (92-95) and that the converse is true as well (96-99). For example, activation of the Wnt signaling pathway in MSCs in vitro stimulates osteogenic differentiation while inhibiting adipogenic differentiation (99). It remains possible that this antagonistic relationship is not only relevant in bone versus fat differentiation of MSCs, but central to differentiation behaviors of stem cells in general. Interestingly the maintenance of the multipotency of MSCs requires a careful balance of pro-adipogenic versus pro-osteogenic factors. Factors of one lineage repress factors of the other, thereby maintaining the undifferentiated state (100).

The process of adipogenesis is generally considered to occur in two phases: the determination phase and the terminal differentiation phase (**Fig. 1.2**) (100). As described by Rosen and MacDougald, the determination phase is temporally the first phase and describes the process of adipocytic lineage commitment of a pluripotent MSC. While this phase is not identifiable morphologically, the cell at this point is considered a pre-adipocyte and has lost some of its pluripotent abilities. In the terminal differentiation phase the cell acquires the molecular machinery to transport and synthesize fat. It is in this phase that the cell can be distinguished morphologically by its characteristic accumulation of intracellular lipids. Unlike in bone where there are many factors

that drive osteoblastogenesis, in adipogenesis, peroxisome proliferating activated receptor- γ (PPAR γ) constitutes the key regulator. PPAR γ is both necessary (101, 102) and sufficient (100, 103) for adipogenesis. PPAR γ is a ligand-regulated transcription factor (104) that regulates the expression of numerous genes of proteins involved in adipogenesis and lipid metabolism including: fatty acid-binding protein aP2 (FABP aP2) (105, 106), phosphoenolpyruvate carboxykinase (PEPCK) (107), acyl-CoA synthase (108) and lipoprotein lipase (LPL) (109). In MSC adipogenesis coincides with increased expression of PPAR γ (110). Another key player in adipogenesis is the C/EBP family of transcription factors. In hMSCs, C/EBP induction occurs in both the early and late stages of adipogenesis indicating a role for these proteins in both lineage commitment and terminal differentiation (110, 111). Members of the C/EBP family directly activate several adipogenic genes, including the master regulator, PPAR γ . Interestingly, once activated, PPAR γ and C/EBPs act synergistically increasing each other's expression through commitment to terminal differentiation (110, 111). While C/EBPs are able to promote adipogenic differentiation when they are up-regulated in non-adipose cells (112), in the absence of functional PPAR γ adipogenesis is not observed (113).

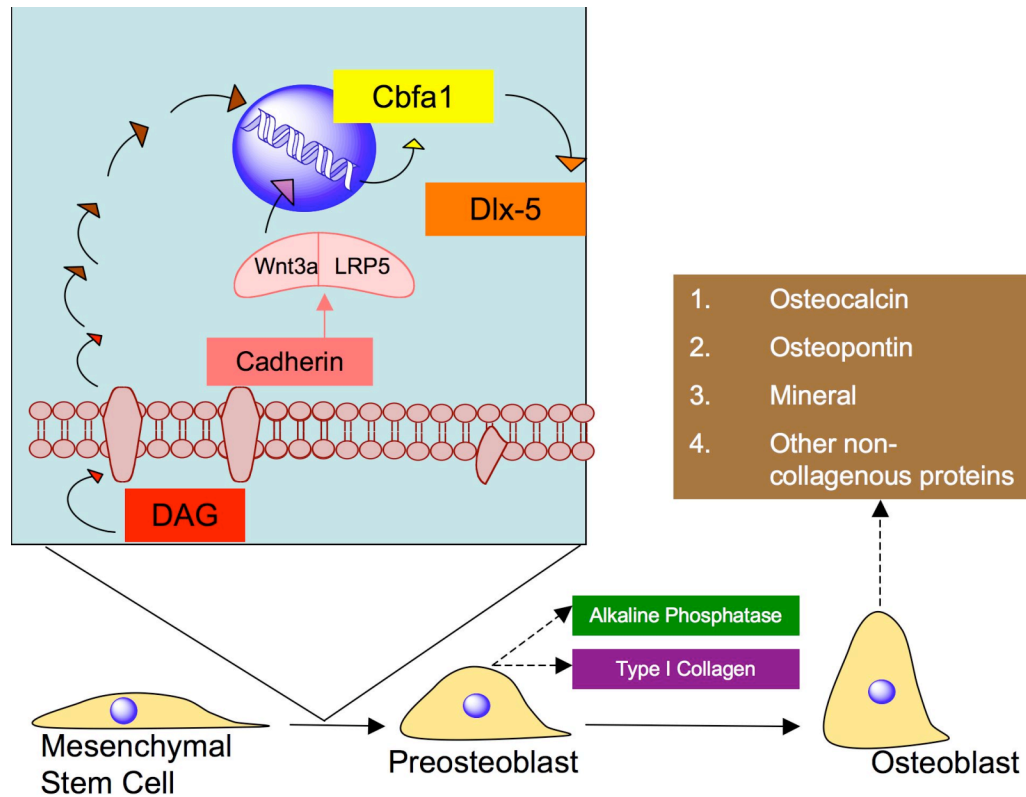


Figure 1.1: Human mesenchymal stem cell osteoblastic differentiation

MSC, in vitro, differentiate to osteoblasts via application of dexamethasone, ascorbate and β -glycerophosphate (DAG). DAG activates a cascade resulting in the up regulation of the earliest osteoblastic marker, Cbfa1. Osteoblastogenesis has also been shown to act via the Wnt pathway, in which Wnt3a, an active form of β -catenin, forms a complex with LRP5, which also results in up regulation of Cbfa1. Up regulation of Cbfa1 induces the expression of Dlx-5, which coincides with differentiation to the preosteoblastic stage signified by production of alkaline phosphatase and Type I collagen. Terminal differentiation to the osteoblastic

phenotype is characterized by production of late osteoblastic markers including: mineral, osteocalcin, osteopontin and other non-collagenous proteins.

Adipogenic induction of MSCs represents a complicated process that depends on many factors. Perhaps the greatest determinant of adipogenesis in vitro is the soluble cocktail applied. Most commonly, adipocytic induction occurs via application of an adipogenic induction media to hMSCs seeded at high seeding densities. This media contains dexamethasone, isobutylmethylxanthine (IBMX), insulin and indomethacin as its active ingredients (68). Serum has also been shown to modulate adipogenesis. Janderova et al. demonstrated that changing the cell culture media supplementation from 5% fetal bovine serum to 15% rabbit serum results in enhancement of adipocytic differentiation in hMSC (114). While soluble factors dominate the literature in terms of modulators of adipogenesis, non-soluble cues also play a role. Cell shape (87) and the extra-cellular matrix environment (115) can have strong effects on hMSC differentiation. Interestingly in these studies, the extra-cellular matrix and cell shape parameters that promote adipogenesis are generally the exact opposite of those that promote osteoblastogenesis. Therefore, like osteoblastic differentiation, adipogenesis represents a complex integration of soluble, matrix and mechanical cues, where often the cues act at in opposition to either promote adipogenesis or osteoblastogenesis.

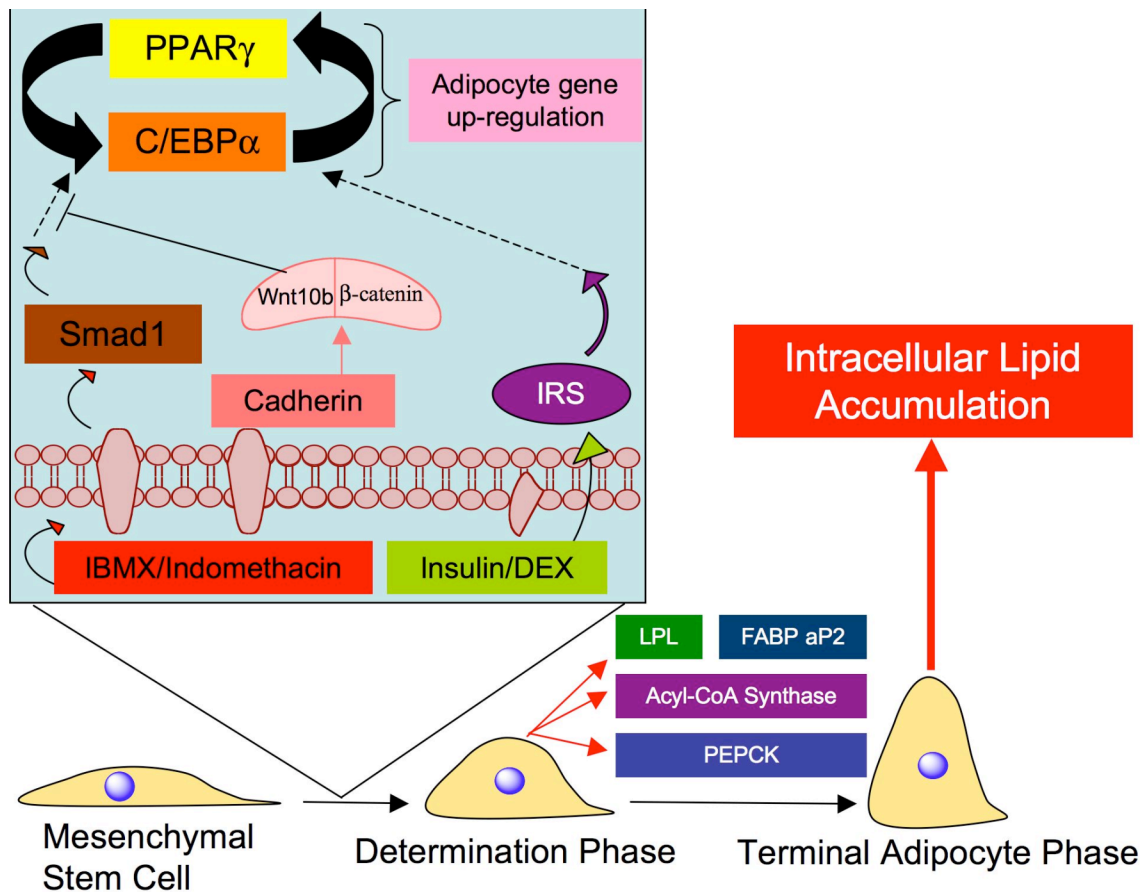


Figure 1.2: Human mesenchymal stem cell adipocytic differentiation

MSC differentiation toward adipocytic lineages occurs in two distinct phases: (1) the determination or lineage commitment phase, and (2) the terminal differentiation phase. Growth factors including but not limited to, dexamethasone (DEX), insulin isobutylmethylxanthine (IBMX), and indomethacin activate a number of intracellular pathways that promote increases in PPAR γ expression. The transcription factor PPAR γ is both necessary and sufficient to induce adipogenesis. In combination with C/EBP α , PPAR γ results in the transcription of genes for proteins characteristic of early adipocytes such as: lipoprotein lipase (LPL), fatty acid binding protein aP2 (FABP aP2), acyl-coA synthase and

phosphoenolpyruvate carboxykinase (PEPCK). Increased lineage progression results in the terminally differentiated adipocyte, which is characterized by its intracellular lipid accumulation. Note in the figure solid black lines indicate direct interactions, dashed lines correspond to signaling cascades and solid red lines indicate protein production.

1.3 A Need for Rationally Designed Novel Polymers

The most commonly attempted strategies in tissue engineering utilize biomaterials as tissue scaffolds. A degradable and resorbable material is desired so that once the defect is repaired, only native/implanted tissue remains (116, 117). Optimally, the degradation and resorption rate of such a scaffold should be tuned so that the falloff in scaffold strength is compensated with an increase in tissue growth (118). Furthermore, polymeric scaffolds are promising candidates for engineering new tissues because they offer a wide array of materials with: three-dimensionality, tunable surface chemistry and degradation rates, an assortment of physical parameters, incorporation of bioactive substances (i.e., growth factors, cytokines, adhesive proteins) and various scaffold architectures (119).

Polymeric biomaterials utilized for clinical needs today, like the poly(α -hydroxy ester)s, were not created explicitly for tissue engineering, but were adapted from pre-existing materials (120, 121). Unfortunately, the implementation of biomaterials that were not designed a priori to meet biologic applications often results in materials that have nonspecific or unidentified reactions with tissues, decreasing the efficacy of the implant (121). The ability to tailor materials to promote cellular functions such as motility, proliferation, and MSC differentiation provides the prospect of composing complex multicellular tissues in vitro, and represents one of the first steps in the realization of engineered whole organ regeneration (122). Unfortunately, the rate-limiting step

in the discovery of new biomaterials is not in the synthesis of new material chemistries, but in the characterization of the biological response elicited by these materials (36, 123).

1.4 The Need for High-Throughput and High-Content Screening of Cell-Biomaterial Interactions

In an attempt to facilitate the progress of tissue engineering and regenerative medicine, scientists have focused their efforts on developing new methods to characterize and understand stem cell responses (47). Essential to this task is the elucidation of the role material scaffolds and soluble factors play in stem cell behavior. To that end, high-throughput and high-content approaches have attracted some of the greatest interest because of their ability to rapidly screen a number of experimental conditions and/or increase the information gain per unit experiment. By increasing the quantity and quality of information gained, these approaches may facilitate the creation of structure-function relationships to guide tissue engineers.

Current trends in high-throughput approaches for the discovery of novel polymeric biomaterials are centered on either the creation of large combinatorially derived libraries that can be systematically analyzed for relevant biological properties or on the creation of single substrates with spatially resolved chemistries, roughness and microstructures (124-137). Once these biologically relevant properties are obtained, computational modeling methods may be employed to determine polymer structure/biological function relationships that can provide predictive insight into novel polymer sets of potential interest (138-148). Recent advances in instrumentation for the synthesis of polymers in

parallel fashions allow for the rapid creation of large polymer libraries, while current methods for the assay of biological properties lack these efficient, high-throughput capabilities (123, 149). Technologies including extracellular matrix microarrays (150), protein chips (151), fluorescence based polymer-screening methods (152), and microfluidics (153) have all been proposed as possible solutions. While these techniques have greatly enhanced the ability for high-throughput biological screening, limitations with regard to the polymer chemistries amenable to the techniques and restrictions on the number of different chemistries able to be screened at once have limited their usefulness in biomaterials discovery. Additionally, while these high-throughput methodologies increase the number of samples that may be assayed, most provide only a single piece of information per unit assay. Therefore, a technique that may be coupled or performed in parallel with these approaches to provide high-throughput screening with detailed molecular biological insight is desired.

High-content morphometric analysis may provide a new approach to increase the quantity and quality of information gained. Currently, morphometric analysis of cellular response in tissue engineering constructs has been a key aspect of the biological characterization. To date, these methods lack reproducible, quantifiable results and largely remain in the domain of qualitative observations (134, 154-159). High-content cell-based screening approaches have been developed for the screening of potential pharmaceuticals and biologically active small molecules (160-164). These assays focus on utilizing quantitative descriptors to screen biological compounds of potential interest in a

high-throughput manner through multivariate statistical analyses. Recent advances in confocal laser scanning microscopy (CLSM), multi-photon microscopy (MPM) and image processing have likewise provided the tools to adapt this “high-content” imaging to cells cultured on biomaterials (165-169) for tissue engineering applications. Perhaps the greatest challenge in adapting these high-content imaging methods to screening stem cell behaviors in tissue engineering approaches results from the difficulty in defining the intracellular molecules and behaviors to target. The ideal molecules will provide early assessment of essential cell behaviors (e.g., stem cell differentiation) that demonstrate long-term predictive value.

1.5 The Cytoskeleton as a Regulator of Cell Behavior

One group of candidate molecules is the proteins that constitute the cytoskeleton. Cells have been described as structures supported by cytoskeletal elements in tension rather than supported by hydrostatic compressional continuity (170-173). In these models, the cytoskeleton of the cell couples the nucleus to integrins providing a path for the propagation of mechanical cues from the extra-cellular matrix (ECM) to the control centers of the cell (174). While a number of cytoskeletal elements are involved in the integrin mechanical coupling, actin filaments remain one of the most studied and integrative elements (175-177). Actin filaments have been implicated in the localization of enzymes, ion mediated signaling, signal propagation to the nucleus and cellular function regulation as reviewed by Janmey (178).

Current studies suggest that the actin-mediated cell shape and the generation of cytoskeletal tension are key regulators of cell function and signaling (**Fig. 1.3**). Cell adhesion to biomaterial substrates induces focal adhesion (FA) assembly. Additionally, changes in cytoskeletal arrangement that promote increased tension result in local FA assembly with the structure of FA's linked to actin filament distribution patterns (179). This bidirectional relationship of FA's and actin is critical as clustering of integrins is mediated by actin, while actin dynamics are modulated by integrin activated Rho GTPases (180). Cell studies by Chen et al., Huang et al. and Mammoto et al. have highlighted mechanisms

by which the actin-based cytoskeleton regulates cell cycle progression and apoptosis (181-183). The proposed mechanism by Mammoto et al. centers on the actin-cell shape based activation of RhoA and its downstream effectors Rho-associated kinase (ROCK) and mDia. ROCK and mDia are antagonistic cell cycle mediators of the Skp2 F-box protein, with increased mDia to ROCK ratio resulting in increased Skp2 protein and mRNA levels. Skp2 protein up regulation promotes the ubiquitination and subsequent degradation of the cell cycle arresting cyclin dependent kinase (CDK) inhibitor p27, therefore promoting cell-cycle progression. Studies that utilized micropatterned selectively adhesive substrates to control cell morphology highlighted cell shape as the dominant factor dictating cell cycle progression when soluble growth factors and insoluble ECM proteins are optimally primed (184, 185). The role of cell shape, actin cytoskeletal tension, Rho, and ROCK in cellular processes is not limited to cell cycle progression. Previously, studies have shown that cell shape affected the differentiation of partially committed precursor adipocytes, osteoblasts, and chondrocytes (186-188). Sordella et al. showed that Rho modulates the insulin growth factor 1 (IGF-1) induced cell fate decision of partially committed adipocytes and myocyte precursors (189). While the above studies highlighted the importance of cell shape in cell differentiation, Mcbeath et al. proposed a detailed mechanism for how the actin based cell shape, Rho, ROCK and cytoskeletal tension influence hMSC differentiation (87). These studies demonstrated that the up regulation of RhoA and ROCK in spread cells resulted in preferential commitment of hMSCs to osteoblastic rather than adipocytic

lineages. However, since RhoA activity only modulated differentiation in the presence of ideal shape configuration (spread for osteoblastic differentiation and round for adipocytic differentiation), it was determined that both cell shape and RhoA activity are needed to steer commitment. In contrast, constitutively active ROCK activity was enough to ensure osteoblastic differentiation regardless of cell shape, thus indicating ROCK as a regulatory unit downstream of both RhoA and cell shape in the commitment process. Thus, the actin cytoskeleton plays an influential role in the governing of cellular processes as it is intimately linked to Rho, ROCK, mDia and their downstream effectors, which in turn function as signaling modulators to differentiation and the cell cycle.

While actin mediates Rho, mDia and ROCK activity within the cell, conversely Rho, mDia and ROCK regulate the generation of the actin cytoskeleton (180, 190). Activation of Rho and its downstream effectors result in the generation of contractile actin-myosin stress fibers and FA assembly (191-194). RhoA activation triggers ROCK activity and phosphorylation of myosin light chain kinase resulting in generation of the cytoskeletal contractility necessary for the formation of thick actin stress fibers and focal adhesions (195-197). Generation of actin contractility has also been shown to be affected by p120 catenin, which when activated through cadherins decreases the activity of RhoA (198). ROCK promotes actin filament assembly via the phosphorylation/inactivation of cofilin, a protein that promotes actin depolymerization (199-201). Concurrent to ROCK's formation of thick actin fibers via increased force generation, mDia1 promotes the assembly of thin actin

filaments (202). mDia1 promotes thin actin filament assembly via nucleation of profilin bound actin monomers that bind to the Formin Homolgy 1 (FH1) domain of mDia1 orienting actin monomers for efficient nucleation (203). Thus, since ROCK and mDia1 promote thick and thin actin fiber formation respectively, different ratios of their activities or spatiotemporal regulation allow for the configuration of a diverse range of actin structures, and subsequently cell shapes (202).

The integration of the actin cytoskeleton into a number of cellular processes demonstrates its utility as a reporter of cell function. Actin filament assembly represents one of the first responses to cell-substrate interactions, occurring even before FAK phosphorylation (204). The actin based cell shape acts as an initial stimulator of Rho, ROCK and mDia, with different cellular morphologies resulting in differential activation of these molecules (87, 205). Additionally, while actin represents one of the initial events in activation of Rho, mDia and ROCK, the morphogenesis of individual actin filaments is a downstream function of the relative expression level of these molecules. Given the importance of Rho, mDia, CDC42 and ROCK in governing stem cell differentiation, apoptosis, and cell cycle progression, actin represents an interesting single molecule that integrates and possibly reports on numerous cellular processes.

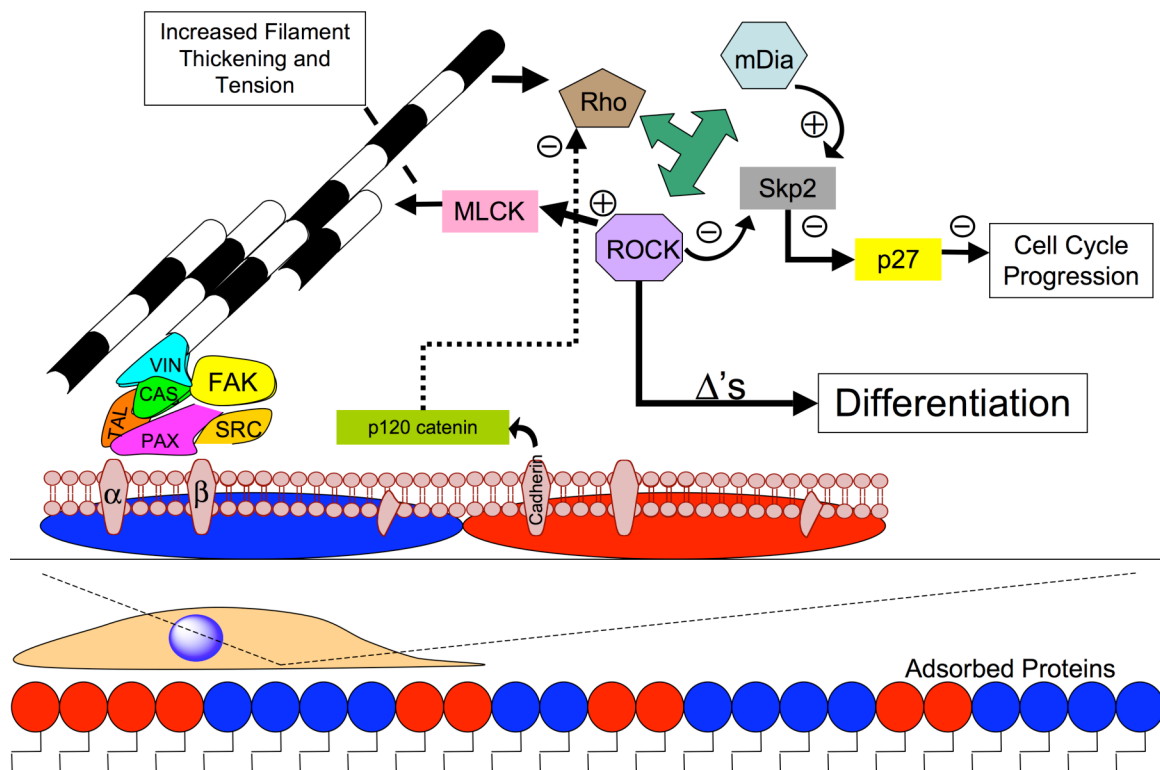


Figure 1.3: Key interactions of the actin cytoskeleton with signaling molecules that govern cell behaviors.

Cell contact with a biomaterial surface is mediated via a protein layer. Attachment of the cell to the adsorbed protein layer initiates signaling cascades, which mediated through actin, result in cell cycle progression and differentiation. Additionally, activation of these signaling molecules feeds back to alter actin filament morphology and tension generation via myosin light chain kinase (MLCK).

1.6 Hypothesis and Aims of the Dissertation

This dissertation was motivated by the need to accelerate the pace of design and screening of regenerative materials using quantitatively rigorous yet biologically grounded methods. This study proposes the development of a high-content imaging approach to characterize and predict cellular responses to soluble factors and biomaterials. If successful, these efforts will ultimately address the top three priorities of the tissue engineering field as described by the MATES group of federal agencies: (1) to understand and control the cellular response; (2) to formulate biomaterial scaffolds and tissue matrix environments; and (3) to develop enabling tools (i.e., high-throughput assays, instrumentation, imaging modalities, and computational modeling) (47). This high-content methodology will characterize cellular response to tailored biomaterials and soluble factors that are involved in the modulation of cell behavior. The developed profiling platform described in this dissertation captures quantitative descriptors of whole cell and cytoskeletal morphology and identifies correlations between these morphologies and cellular responses to soluble factors and synthetic biomaterials. The central premise of the study is that quantitative measures of cytoskeletal morphology can be used to forecast long-term differentiation behaviors of stem cells that occur days to weeks later than the early times at which the morphometric analysis is conducted. The proposed study could serve as a platform to evaluate cells/biomaterials within a complex milieu as it provides: predictive measures of long-term cell behaviors at early time points, real time measures of stem cell fates, cell-by-cell based analysis that

is capable of capturing the heterogeneity of sample populations, and the ability to parse out lineage commitment in stem cells resulting from multiple stimuli.

The cytoskeleton serves as a regulator for the “outside-in” cellular signaling that underlies a wide range of cell behaviors. The hypothesis is that the actin cytoskeletal organization embodies a cellular “fingerprint” that when quantified provides one of the earliest markers and/or predictors of cell behavior. The behaviors of interest in this study will ultimately focus on human mesenchymal stem cell (hMSC) lineage commitment and differentiation. This dissertation will develop the descriptors necessary to define this fundamental cytoskeletal based profiling approach and ascertain their utility via four aims:

1. The establishment of a "high content" imaging platform for extracting quantitative cell morphologic descriptors.
2. The application of the platform developed in aim 1 to identify cell descriptors that are responsive to chemistry and roughness of a gradient-based polymer substrate.
3. The extension of the “high-content” imaging platform to a systematically varied library of polymer materials to identify material responsive descriptors and predict long-term cell behaviors based on early morphologic descriptors.
4. The determination how early substrate induced morphological descriptors may encode the decision making of stem cells cultured in response to varying soluble factors, protein ligands of the extracellular matrix and surface properties of polymeric substrates.

2 Development of a “High-content” Imaging Platform for Studying Cell-Material Interactions

Note: This chapter is reproduced from the following publication:

Treiser, M.D., E. Liu, R.A. Dubin, H.J. Sung, J. Kohn, and P.V. Moghe. 2007. “Profiling cell-biomaterial interactions via cell-based fluororeporter imaging.” *Biotechniques* 43:361-366, 368. © 2008 BioTechniques. Used with permission.

2.1 Introduction

Cell-based therapies, combined with tissue engineering, have the potential to bring regenerative medicine to the clinic. A major challenge is the development of selective substrates that are permissive and instructive for the growth of complex functional tissue in vitro. The requirements for selective cell attachment, survival, migration, growth, and differentiation will require an integrative understanding and application of cellular and molecular responses to the chemical, mechanical, and topological properties of substrates.

A wide range of natural and synthetically designed materials have been employed to culture and expand mammalian cells within tissue culture substrates, bioreactors, and implantable scaffolds. Despite their reduced bioactivity, synthetic biomaterials offer advantages over natural substrates, including reduced risk of immunological response and disease transmission, and controlled properties. For example, the ability to manipulate structure through chemistry and fabrication provides opportunities to engineer specific properties, including biodegradation, fouling, drug elution and biofunctionalization, which are desirable for introducing tissue-specific targeting, and tissue regeneration and

remodeling. The characterization of newer generation cell-interactive materials requires complex considerations, and is further hampered by the lack of integrated data on extracellular matrix and protein conditioning, cell adhesion, motility, apoptosis, and differentiation processes, as well as the mechanisms of outside-in signaling on biomaterials. While rapid methods for quantifying protein adsorption have been developed (152, 153, 206, 207), the characterization of cell–biomaterial interactions at the cellular and subcellular level remains time consuming and expensive (138). A need exists for qualitative and quantitative tools that can rapidly assess cellular response to biomaterial substrates.

The green fluorescence protein (GFP) technology has revolutionized the detection and analysis of dynamic structural and biochemical changes in living cells (208, 209). We have developed genetically engineered cell lines expressing a series of GFP fusion genes that visually report on a variety of physiological properties in living cells. The present study describes a new way to utilize these GFP fusion genes as visual live reporters for quantitative characterization of cell-biomaterials interaction. Using quantitative image analysis, the reporter information can be further dissected to yield molecular level metrology of the cell-material interactions.

2.2 Materials and Methods

2.2.1 Polymer Synthesis and Fabrication

Biomaterials used in this study were from the family of tyrosine-derived polycarbonates synthesized utilizing previous published procedures (210-214). Polymers derived from desaminotyrosyl tyrosine alkyl ester monomers were named poly(DTR carbonate)s with R = ethyl (E) or octyl (O). Copolymers of x mole% desaminotyrosyl tyrosine alkyl ester with y mole% desaminotyrosyl tyrosine with a free acid (DT) and z % Poly(ethylene glycol) (PEG) blocks of 1000 units were identified as poly(x %DTE-co- y %DT-co- z %-PEG₁₀₀₀ carbonate). Finally, copolymers of x mole% iodinated desaminotyrosyl tyrosine alkyl ester with y mole% iodinated desaminotyrosyl tyrosine (DT) and z % PEG blocks of 1000 units were simplified as poly(x %I₂DTE-co- y %I₂DT-co- z %-PEG₁₀₀₀ carbonate) (**Fig. 2.1**). This library of polymers was used to evaluate the sensitivity of cell reporters to changes in substrate hydrophobicity (hydrophobicity is increased with length of alkyl chain; thus, DTO is more hydrophobic than DTE) (215, 216); stiffness (increased with iodination; decreased with PEG incorporation) (213, 214), charge (incorporation of DT adds negative charge at physiologic pH) (210, 217, 218), and protein-repulsive character (increased PEG levels lower protein adsorption) (219, 220). Two-dimensional polymer films were spin-coated (Photo-Resist Spinner; Headway Research, Inc., Garland, TX) onto 15 mm glass coverslips with 100 μ L of a 0.2 μ m pore PTFE-filtered, 1% polymer

solution in 98.5% methylene chloride / 1.5% methanol (v/v). All polymer surfaces were sterilized by exposure to UV.

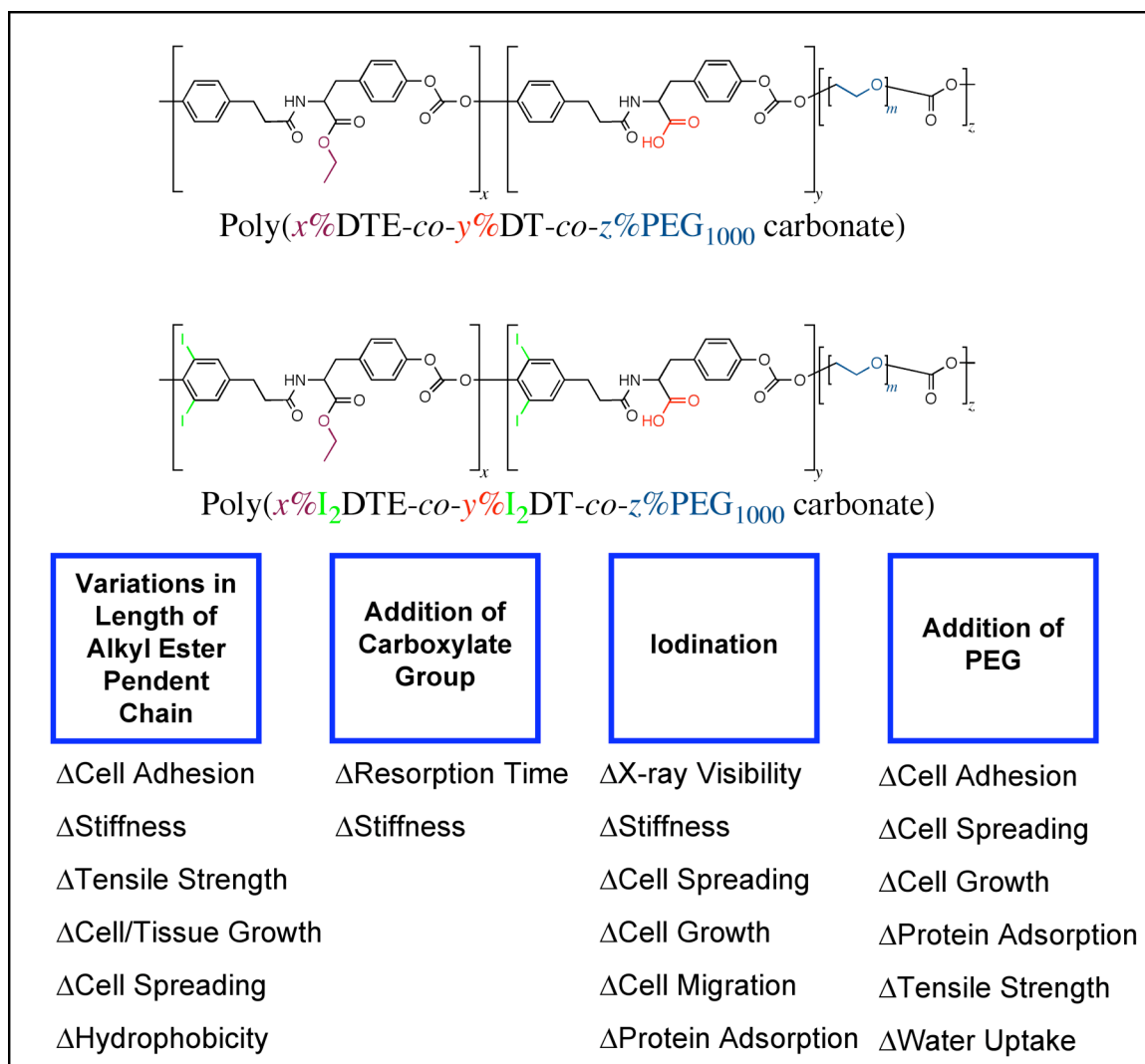


Figure 2.1: Chemical Structure and nomenclature scheme for Tyrosine Derived Polycarbonates.

Changes in biological and material responses to the polymer from alterations of the chemical formula are shown.

2.2.2 Cell Culture and Transfection

GFP-based plasmids were obtained from academic laboratories (221, 222) and commercial sources (Clontech, Mountain View, CA). Plasmids were targeted to specific organelles through the addition of a short localization signal (such as GFP-f for farnesylation) and to specific cytoskeletal proteins (such as GFP-actin) (**Table 2.1**). Several model cell lines were employed, including CHO-K1 (ATCC; Manassas, VA) and Saos-2 (a gift from David Denhardt; Rutgers University). The cells were propagated in F12H (Invitrogen; Carlsbad, CA) supplemented with glutamine, penicillin-streptomycin, and 10% fetal bovine serum (Sigma; St. Louis, MO). Cells were transfected with Lipofectamine supplemented with PLUS reagent (Invitrogen) and stable lines were selected using 0.5 mg/ml (Saos-2) or 1 mg/ml (CHO-K1) G-418 (Sigma). Utilizing G-418 selection, cell populations with as high as 80% of total cells expressing the fluorescent reporters were achieved. Where indicated, cells were fixed via treatment with a 4% paraformaldehyde solution for 15 minutes at room temperature.

Table 2.1: GFP-based plasmid reporters used for profiling cell-biomaterial interactions

Plasmid	Cellular Targeting Sites	Sources
pEGFP-Farnesylation	Plasma Membrane	Clontech
pEGFP-actin	Microfilaments ((β -actin)	Clontech
pEGFP-tubulin	Microtubules (α -tubulin)	Clontech
pEGFP- α -actinin	Focal Adhesion (α -actinin)	Edlund et al. (2001) (221)
pEGFP-paxillin	Focal Adhesion (paxillin)	Laukaitis et al. (2001) (222)
pGAPDH-GFP	cytoplasm→nucleus	Shashidharan et al. (1999) (223)

2.2.3 Imaging

For lower resolution imaging, cells were seeded at a density of 3,000 to 7,400 cells per cm² and imaged with a Nikon Eclipse TE 2000-S inverted fluorescence microscope with digital photomicrographs obtained using Image Pro-Plus software (Media Cybernetics, Silver Spring, MD). High content confocal imaging was performed using the same above cell seeding densities with a TCS SP2 laser-scanning spectral confocal microscope (Leica Microsystems; Exton, PA).

2.2.4 Morphometric Analysis

Morphometric descriptors were quantified using high-resolution, single cell, confocal images obtained from cells expressing GFP-fusion proteins through Image Pro Plus (Media Cybernetics, Silver Spring, MD) (**Table 2.2**). Individual cell images were processed with commercially available software. Raw images were exported to Image Pro Plus Version 5.1 for windows (Media Cybernetics). Images first underwent image enhancement optimization (image contrast, brightness and gamma value adjusting) to equalize image intensity histograms. Contrast enhanced images were then filtered utilizing a ten pass Gaussian filter and then a series of Flatten filters. A pseudo-automated adaptive thresholding process was then employed allowing the whole cell and individual cytoskeletal proteins to be separately segmented based on the image intensity histogram. Once either the whole cell or individual cytoskeletal elements were segmented, shape and higher order moment descriptors were calculated utilizing the count

object menu in Image Pro Plus on the segmented objects. Multiple cells examined for each polymer substrate were used to calculate a population distribution for each descriptor. Descriptors included 1) cellular morphologic parameters: area, perimeter, length of major and minor axes of the ellipse with the same geometric area of the cell, mean radius, mean diameter, roundness, protrusions, and protrusion length, mean feret length, maximum feret length and minimum feret length; 2) cytoskeletal parameters; fractal dimension, margination, heterogeneity, clumpiness, and average fiber length/width; 3) focal adhesion parameters; integrated optical density, heterogeneity, margination, clumpiness, focal adhesions per cell, strength of focal adhesion region, and total area of actinin/paxillin rich structure per cell; 4) texture metrics; and 5) higher order moments; skewness and kurtosis (**Table 2.2**).

Table 2.2: Definitions of morphometric descriptors that can be quantified from the digitized images of fluororeporter cells on biomaterials.

The descriptor definitions were adapted from those available in Image Pro Plus (Media Cybernetics, MD).

Descriptor	Descriptor Definitions
Area	Contiguous area of each object minus any holes
Area/Box	Ratio between area of object and area of its bounding box
Aspect	Ratio between the major and minor axis of object-equivalent ellipse (i.e., an ellipse with the same area and first and second degree moments)
Axis (major, minor)	Length of the major/minor axis of object-equivalent ellipse
Box X/Y	Ratio between the width and height of object's bounding box
Clumpiness	Fraction of heterogeneous pixels remaining after erosion
Diameter (max, min and mean)	Length of the longest/shortest/mean line passing through the centroid joining two outline points
Feret (min, max and mean)	Longest/shortest/average caliper length
Fractal dimension	Dimension of the object's outline calculated as 1 minus the slope of the regression line obtained when plotting the log of the perimeter against the log of the stride length
Heterogeneity	Fraction of pixels that vary more than 10% from the average intensity of the object
Integrated Optical Density	Average intensity/density of each object
Margination	Distribution of intensity between center of object and its edge
Perimeter	Length of the outline of object using a polygonal outline
Radius (max, min)	Length of the longest/shortest line between the object centroid and its perimeter
Radius Ratio	Ratio between the maximum and minimum radius
Roundness	Square of object perimeter divided by 4π times object area

2.2.5 Apoptosis Studies

Two approaches were used to quantitatively track apoptosis in Saos-2 cells cultured on selected biomaterials. Cells were labeled either with a mitochondrial transmembrane potential-sensitive cationic dye (Mitocapture Mitochondrial Apoptosis Detection Kit, Biovision, Mountain View, CA), or transfected with Saos-2 /GFP-GAPDH, and imaged after 3 days in culture. The mean pixel intensity of apoptotic green fluorescence minus background was determined in mitocapture labeled cells using ImageJ software (NIH) (224), and normalized to the number of nuclei counter-stained with Hoechst (Sigma) in each image field. For GFP-GAPDH expressing cells, the total pixel intensity of nuclear regions was determined separately from the total intensity of cytoplasm after subtracting background using ImageJ (NIH). The ratio of the nuclear-associated intensity compared to that within the cytoplasm was quantified from eight single cell-images obtained through four independent experiments (n=8, where n is the total number of cells examined) (224, 225).

2.2.6 Statistical analysis

Statistical analysis was performed on morphometric parameters using SPSS software (SPSS inc. Chicago, IL), and included ANOVA with Tukey's HSD post hoc method, principal component analysis, and other multivariate statistical tools. All the other comparisons were performed using Student's t-test. A p-value <0.05 was considered significant. Results are mean \pm SEM.

2.3 Results

2.3.1 Biomaterials-Responsive Cell GFP Reporters

Immortal cell lines engineered to express GFP fusion proteins (**Table 2.1**) were used as probes to identify differential cellular and molecular morphologies induced by variations in composition and processing of biodegradable, polymer substrates.

First, we sought to demonstrate the utility of the live reporter imaging for detecting changes in material hydrophobicity. As shown in **Fig. 2.2**, live cell imaging of GFP-f transfected Saos-2 cells allowed the discrimination of several cellular morphologic differences in response to two different biomaterials; poly(DTE carbonate) and the more hydrophobic poly(DTO carbonate) (Water contact angles of 73° and 90° respectively as by goniometry (215)). The extent of cell spreading was quantified following digital image analysis using cells expressing GFP-f, a farnesylated variant that confers fluorescent demarcation and resolution of the plasma membrane. Morphometric descriptors of average cell area, perimeter, length of major and minor axes, and diameter of Saos-2/GFP-F cells demonstrated reduced cell spreading on poly(DTO carbonate) relative to poly(DTE carbonate). These differences correlated with organizational differences in the cytoskeleton and focal adhesions. Morphometrics of focal adhesions, quantified by analyses of Saos-2/GFP-actinin and Saos-2/GFP-paxillin cells, showed different margination, clumpiness, the number of focal adhesions per cell, integrated optical density, and total area of actinin/paxillin rich regions between the two polymers. These results demonstrated that

hydrophobicity of poly(DTO carbonate) might reduce the number and strength of paxillin-rich structures, and restrict their localization to the cell periphery. Visual observation also confirmed that Saos-2 exhibited fewer and shorter stress fibers, and significantly fewer, less well organized focal adhesions, on poly(DTO carbonate) in comparison to the cells on poly(DTE carbonate).

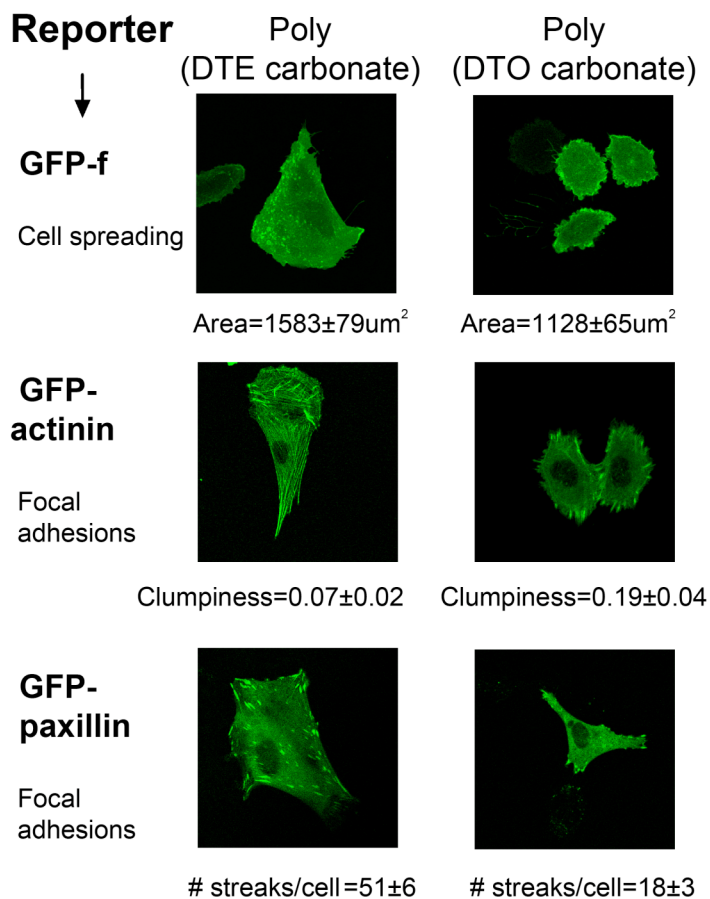


Figure 2.2: Confocal micrographs of GFP-engineered SaOS2 cells on two polymeric substrates with different backbone compositions leading to differing hydrophobicities.

While qualitative differences in cell spreading are apparent, fluorescent reporter variations are clearly discerned through morphometric analysis. Significant differences were observed in just three, simple morphometric parameters estimated for each reporter. This highlights the ability of higher resolution imaging of GFP-reporter cells and image processing to probe cell responsiveness to minute variations in polymer substrates.

2.3.2 "Heat Map" Representation of Cell Descriptors for Combinatorial Biomaterials

Morphometric image analysis can be a powerful tool in identifying cellular responses to biomaterials that may seem qualitatively difficult to distinguish. As indicated in **Fig. 2.3**, Saos-2/GFP-actin cells grown on poly(DTE carbonate), poly(DTE-co-4%PEG carbonate), poly(DTE-co-10%DT carbonate), and poly(DTE-co-4%PEG-co-10%DT carbonate) were nearly indistinguishable through visual observation. However, through quantitative morphometry it was possible to expose polymer-dependent differences in cell shape based descriptors. Selected descriptors of cellular morphology showed statistical variations on the different substrates. Certain material discriminating descriptors (MDD's) are sensitive to the addition of PEG (Perimeter), charge (Radius and Radius Ratio), or both PEG and charge to the polymer backbone. While the addition of PEG or charge alone to the polymer backbone did not result in significant changes in cellular shape, the combination of both charge and PEG had a profound effect. From the color-coded "heat map", descriptors can be identified that are responsive to single elements of chemical change within a combinatorial library. For example, the radius ratio of a cell is statistically different with the addition of charge to the polymer backbone, regardless of the presence of PEG. Because radius ratio appears sensitive to the addition of charge to the substrate, it therefore functions as one cellular morphological reporter of the presence of charge to the polymer.

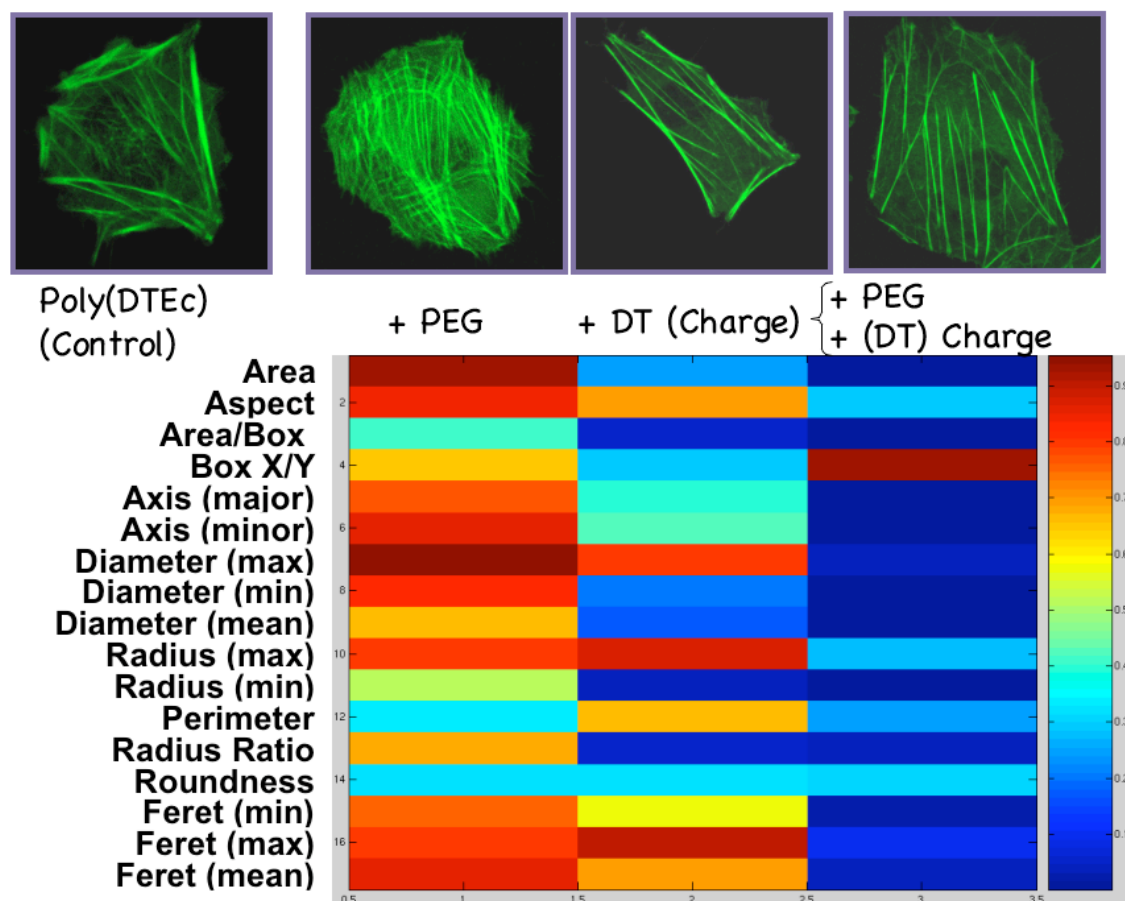


Figure 2.3: Cell responses to a combinatorial variation in substrate properties can be discerned using high content imaging of cell GFP-reporters and a "heat map" representation of variations in morphometric descriptors.

This figure illustrates the representative cell images (top) and the corresponding heat map for the morphometric analysis (bottom) of Saos-2 / GFP-actin cells on poly(DTE carbonate) polymer substrates with additions of charge, PEG or both PEG and charge. It is challenging to resolve the qualitative differences between cells on the multiple substrates. However, the heat map representation of the quantitative descriptors allows such differences to be determined. A strong

statistical difference in descriptor value (Student's T-test P value \rightarrow 0) is represented by blue, a moderate difference by turquoise, a minor difference by orange and no statistical difference (P value \rightarrow 1) by red. Note that the colors do not indicate whether the descriptor value is higher or lower than the descriptor value for cells cultured on Poly(DTE carbonate).

2.3.3 Morphometric Descriptors of Cell Functional Fates on Biomaterials

In addition to morphological features, GFP-based signaling reporters were used to characterize functional differences in cellular response to constitutive difference in the substrates. For example, it has been demonstrated that GFP-GAPDH translocates from the cytoplasm to the nucleus during early stages of apoptosis (223) in a wide variety of cell types. A significant increase in apoptosis (measured via Mitocapture assay) was seen in Saos-2/GFP-GAPDH cells grown on poly (I₂DTE carbonate) compared to growth on poly(DTE-co-10%DT carbonate) ($p < 0.05$). We quantified the inverse "margination" descriptor of Saos-2 / GFP-GAPDH distribution within cells grown on poly(DTE carbonate), poly(DTE co-10% DT carbonate), and poly(I₂DTE carbonate), which is indicative of the cytoplasmic to nuclear distribution of GFP-GAPDH. This descriptor correlated well with independent measures of cell apoptosis (**Fig. 2.4**).

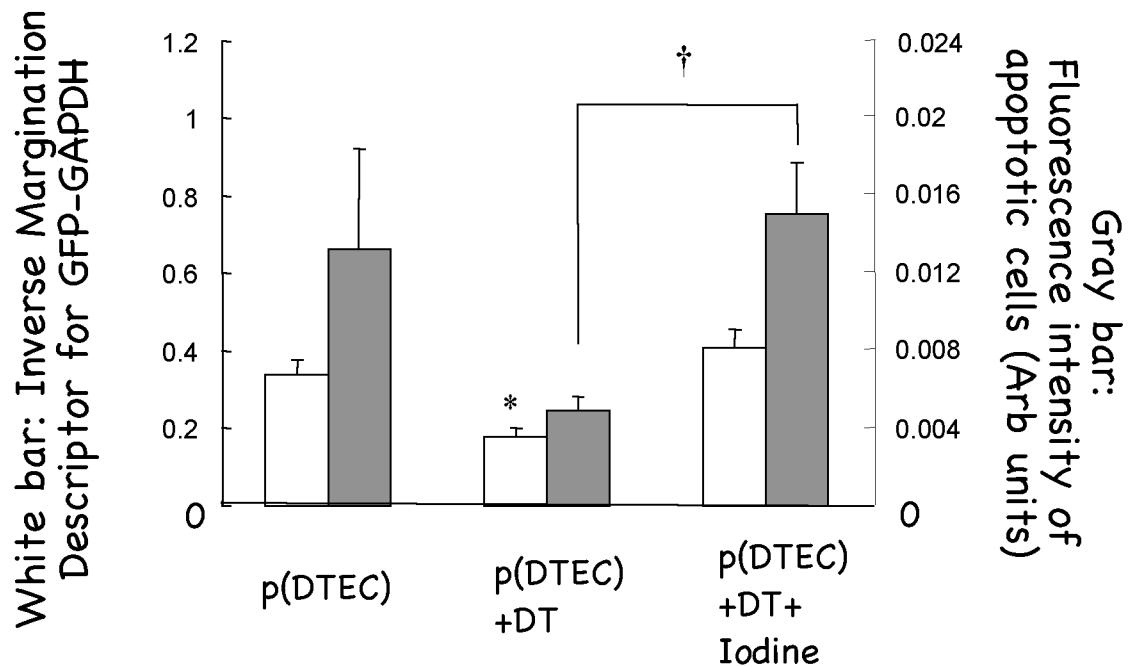


Figure 2.4: Morphometric descriptors quantified for cell fluorescent reporters can be used to profile cell functional fate on biomaterials, for example, cell apoptosis.

GFP-GAPDH transfected Saos-22 cells were cultured for 72 hours on control films of poly(DTE carbonate) and poly(DTE carbonate) incorporating charge (DT), and both charge and a heteroatom, iodine. The inverse margination (nuclear to cytoplasmic ratio) of Saos-2/GFP-GAPDH (white) was correlated with fluorescence intensity from Mitocapture assay (gray) and Saos-2 cells (gray)

* $p < 0.05$ vs. others among white bar groups.. † $p < 0.05$ between the lined gray bar groups (figure supplied by Dr. Hak Joon Sung).

2.4 Discussion:

Cell interactions with biomaterials have been traditionally examined in terms of cellular functions, which are then correlated to biomaterial properties. However, many cell functions do not respond systematically to variations in biomaterial chemistry or physical features, confounding the elucidation of the underlying structure-function relations. This challenge gets compounded for the next-generation biomaterials that are combinatorially designed and synthesized. Such polymeric materials present a wide range of chemical, structural and physical properties, which can interact in multiple ways with biological systems including extracellular matrix components and cells. The present report offers a simple approach to quantitatively "profile" biomaterials in terms of intracellular descriptors of the morphometric organization of GFP-engineered cells.

The current development of GFP-based expression markers has proceeded largely following the emphasis on detecting on and off molecular expression and interaction involved in intracellular events. Examples include GFP-based protein-protein interactions, histone methylation, and tyrosine kinase activity (226-228). The present study highlights methodologies to utilize these GFP fusion genes as visual live reporters for quantitative characterization of cell-biomaterials interactions. Using polymer members of a recently established library of biomaterials, we have demonstrated that the integrated use of GFP reporter cells, live (confocal) imaging, and simple morphometric analysis, can be used as a basis to (a) elucidate quantitative changes in cell responses to minute

variations in biomaterial substrates; (b) help codify cell descriptors that report on specific variations in biomaterial properties; and (c) relate cell morphometrics to cell functions.

The major advantage of using GFP-based live reporters to profile biomaterials is the ability to easily obtain dynamic imaging over time compared with the need for multiple, fixed preparations inherent to immunocytochemical methods, and the introduction of artifacts related to the use of vital stains (229-231). In addition, by eschewing fixation of tissue or cell specimens, artifacts related to possible differential cell adhesion to chemically and structurally diverse biomaterial surfaces can be avoided. For instance, we have observed that cell morphologic descriptors in fixed cells are altered in relation to those of unfixed, reporter cells (**Fig. 2.5**). While heterogeneous cell morphologies were observed on substrates both with and without fixation, population distributions of live cells imaged on particular substrates were highly reproducible. When cells underwent fixation, not only were calculated morphometrics incongruent with those attained in live cell imaging, but the relative trends of the descriptors based on polymer chemistry were skewed. For example, the calculated average cell area for live cells cultured on poly(DTE-co-10% DT carbonate) was indistinguishable from those cultures on poly(DTE carbonate). However, when cells were fixed, the average cell area on the charge (DT) containing polymers doubled relative to those on DT-deficient poly(DTE carbonate) (**Fig. 2.5**). Cell fixation and subsequent processing (washes) allows only the most adherent cells to be imaged and evaluated, skewing the complete range of morphogenetic response

of cells to the substrate. The practical limitation posed by the GFP-reporter approach is the challenge of generating specific GFP fusion genes and their introduction into a variety of different cell types. This problem is magnified by the low frequency of transfection often associated with primary cells, which are coincidentally just the cells whose responses to polymer substrates are of most interest to biomaterials scientists and bioengineers. For this reason the cell types employed in this study for method development were the CHO-K1 and Saos-2. Their immortalized nature facilitated the development of reporter cells because they demonstrated high transfection efficiencies with the ability to undergo numerous stable line selection passages without perturbation of cellular behavior. However, the method presented may be adapted to primary cell lines of interest given that the desired fusion genes can be incorporated into the primary cell lines, albeit with low efficiency. The morphological screening method presented is amenable to low transfection efficiencies because not every cell need be imaged, just enough cells to provide a representative population distribution. Thus, while this study utilizes immortalized cell lines for method development, the method is robust in that it can be adapted for the characterization of primary cells cultured on biomaterial substrates.

Our studies using cell fluorescent reporters demonstrated differences in cellular response associated with polymer constitutive and surface properties. For example, increased substrate hydrophobicity generated by side chain extension or the inclusion of iodine into poly(DTE carbonate) reduced cell spreading descriptors and altered the organization of structural components of

the cytoskeleton and focal adhesions. Using the distribution descriptors for GFP-GAPDH, we confirmed that polymers-incorporating iodine stimulated apoptosis in Saos-2 cells. Although mechanisms of apoptosis on our substrates are not clear, these results are consistent with previous studies that have shown that molecular iodine (232) and excess iodide in the form of KI (233) can stimulate apoptosis in vitro in breast and thyroid cells, respectively, and that hydrophobic substrates elicited increased apoptosis in the human osteosarcoma cell line, MG63 (234).

The "heat map" representation of the calculated descriptors represents a powerful tool for the efficient analysis of cell-biomaterial interactions. Combinatorial-based libraries with large numbers of polymers are particularly well suited to this method of analysis. The heat map representation may facilitate the rapid identification of polymer substrates of interest because polymers that elicit statistically different cell population morphologies are readily identifiable. Through our "heat map" analysis, we identified poly(DTE-co-4%PEG-co-10%DT carbonate) as a polymer that induces large morphological changes in cellular functions. Previously, Weber et al. identified polycarbonates containing PEG and DT as those that invoked desired cellular and protein adsorption responses for use in blood contacting polymer stents (235). This finding was ascertained via the systematic and time-consuming study of copolymer systems, but might have benefited from a more "high-throughput" cellular based "heat-map" approach that could have isolated cell profiles for polymer compositions of interest.

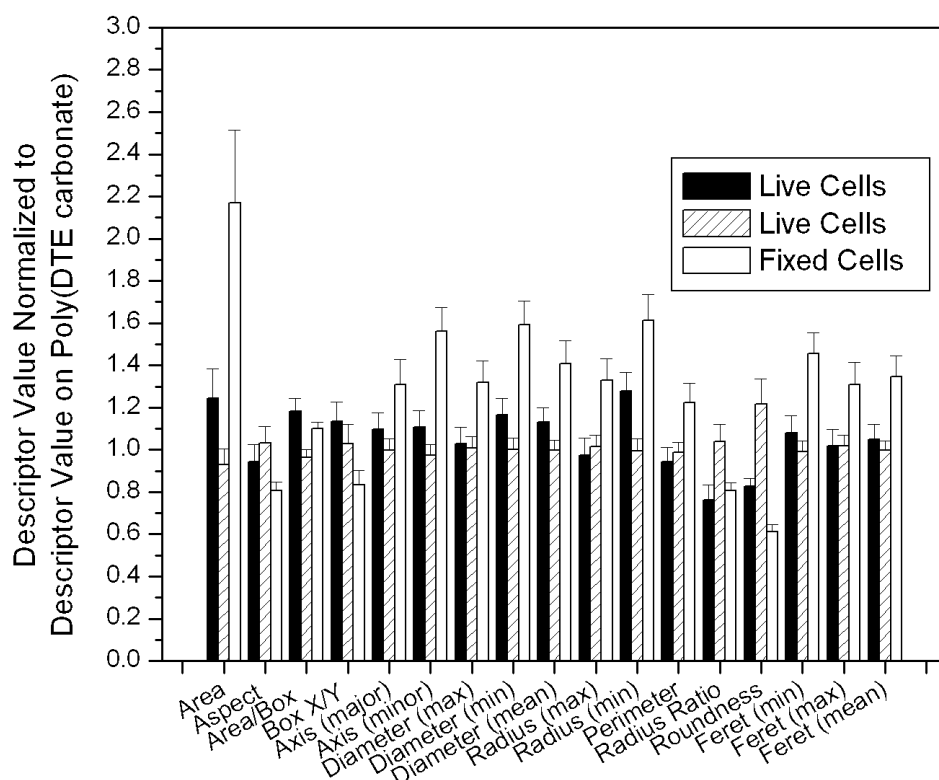


Figure 2.5: Living cell reporters offer clear advantages over fixed cells toward effective computation of cell descriptors on biomaterials

Morphometric descriptors were compared for 17 cell shape descriptors of cells cultured on poly(DTE-co-10%DT carbonate). Descriptors were calculated for individual cells, with statistics shown representative of the sampled population of cells. Trials were performed where cells were fixed to determine if fixation alters computed descriptors. The descriptors for fixed cells were skewed toward descriptors of the more adherent cell subpopulation. Multiple trials were performed to ascertain the consistency of the living cell descriptors on the different polymers and are represented by the two experimental “Live Cell” data sets within the figure. These two “Live Cell” groups represent two independent

experiments of morphometric analysis of populations of engineered living cells cultured on the aforementioned polymer substrate. Living cell morphometric descriptors were found to be highly reproducible.

2.5 Conclusion:

In conclusion, we present an imaging and image analysis based approach to decode the simplest morphologic cell responses to biomaterials. These approaches can be easily extended to other two-dimensional substrates as well as three-dimensional materials. The descriptors defined in this study are morphometric in nature, but can, in theory, be extended to other aspects of the cytoskeletal organization, as well as to its dynamics. More rigorous modeling approaches will be necessary to relate the cell descriptors to biochemical "signal inputs" from the substrate, on the one hand, and to the "downstream" cell functions, on the other. Taken together, these experimental approaches coupled with computational approaches for mining and modeling the data may have the potential to advance the field of biomaterial informatics (123) and to piece together the biological data necessary to put together "material biointeractomes".

3 High-content profiling of cell responsiveness to graded substrates based on combinatorially variant polymers.

Note: This chapter is reproduced from the following publication:

Liu, E., M.D. Treiser, H. Patel, H.J. Sung, K.E. Roskov, J. Kohn, M.L. Becker, and P.V. Moghe. 2009. "High-content profiling of cell responsiveness to graded substrates based on combinatorially variant polymers". *Combinatorial Chemistry and High-throughput Screening - Special Issue on Combinatorial and High-Throughput Screening of Cell Response to Biomaterials* 12(6). © 2009 Chemistry and High-throughput Screening. Permission pending.

3.1 Introduction

Polymer substrates differing in chemical properties, post-processing physical properties, and geometries have been shown to cause variable changes in cellular processes by way of alterations in protein adsorption, cell adhesion and spreading, and extracellular matrix production (236, 237). Parameters such as hydrophobicity, physicomaterials, architecture, and differential ligand conditioning represent strong determinants of both cell function and phenotypic expression (155, 219, 238, 239). Most of the studies to date depend on traditional characterization assays and a limited number of material conditions. This limitation on potential physical parameter space represents a significant shortcoming as interesting behaviors elicited in response to incremental but unselected experimental conditions may be overlooked.

Current trends in polymeric biomaterials discovery have expanded from the synthesis of a few potential materials to the design of relatively large libraries

of combinatorially derived materials (123, 124, 126). These libraries permit the exploration of a large physico-chemical "property" space while simultaneously promoting the development of detailed relationships that relate cellular actions to material parameters (129, 138, 240). Advances in instrumentation for the synthesis and assembly of large polymer libraries have expanded the size and complexity of available material arrays (127). The advantage of such sizeable material test sets lies in the more thorough examination of cell-material behaviors that would have otherwise gone unnoticed when investigating smaller libraries. However, the full impact of combinatorial polymer libraries will be realized only with the development of methods that are able to evaluate material performance on the scale of the synthesis (123). Unfortunately, traditional approaches to the characterization and the biological screening of materials are not amenable to the rapid evaluation of large member material sets and therefore, necessitate the development of novel screening approaches.

One technique that has garnered significant interest involves the creation of single substrates with spatially resolved chemistries, roughness, and/or microstructures (128, 134, 241-243). Single substrate approaches allow for the assay of cellular response to materials of differing properties with equivalent processing conditions and faster data acquisition, thereby providing lower experimental error (131, 132). Additionally, studies that vary both chemistry and temperature and utilize gradient-based technology permit the simultaneous study of continuous ranges of chemical and topographical properties (128, 129, 243, 244). These methods represent great potential as they map the near complete

compositional and processing experimental space of binary blends. This matrix of chemistries and surface physical properties further facilitates the identification of potentially new structure-function relationships that may help biomaterial scientists to rationally design materials to meet specific applications.

To establish cell-material relationships, it is necessary to isolate individual material parameters and their effects on specific responses. Zapata et al. employed continuous temperature gradients to assess osteoblast response to demixed polymer blends (243). Previously, Bailey et al. utilized discrete binary blends of two tyrosine-derived polycarbonates, poly(DTE carbonate) and poly(DTO carbonate) (abbreviated as pDTEc and pDTOc, respectively, throughout this manuscript) and used phase separation-induced topography to determine how changes in material surface energetics and roughness affect cells grown on these surfaces (242). These studies demonstrated that surface microstructure and topography strongly influenced cell attachment, spreading, and proliferation. One limitation highlighted by the authors in this study was that because the topographical features of the surface were dependent on both composition and temperature, universal structure-function correlations regarding roughness, surface chemistry, and cell responses could not be readily ascertained.

Recently, Treiser et al. published a technique whereby high-content imaging of cell morphology yielded a large number of quantifiable descriptors that can be used to potentially discern combinatorial variations in substrate composition (245). Using a similar high content imaging approach, this study

derives morphometric descriptors from cells cultured on discrete binary blends of pDTEc and pDToC that have been annealed on a gradient heat stage, which yields a temperature-induced roughness profile. Cell descriptors that are sensitive to roughness and/or surface chemistry are identified, and were utilized to decouple the effects of roughness and surface chemistry on cell attachment and adhesion strength. This study demonstrates a fast-screening, high-content imaging method to discern how surface topography and surface energy of structurally similar but compositionally varying, immiscible blends affect biological response on two dimensional gradient substrates.

3.2 Materials and Methods

3.2.1 Polymer synthesis and gradient fabrication

Tyrosine-derived polycarbonates were synthesized as described previously (215). Poly(desaminotyrosyl-tyrosine alkyl ester carbonate)s are referred to as poly(DTR carbonate)s, where R represents the alkyl ester pendent chain. In this study R is either ethyl (DTE) or octyl (DTO). The mass-average molecular mass and molecular mass distribution M_w/M_n (PDI) for each of the polymers are listed. Poly(DTE carbonate) (abbreviated pDTEc): $M_w = 131,000$, PDI = 3.0; poly(DTO carbonate) (abbreviated pDTOc): $M_w = 61,500$, PDI = 2.7.

3.2.2 Annealing Gradient Preparation

Discrete composition thin film strips of pDTEc and pDTOc tyrosine-derived polycarbonate homopolymers and blends (70/30,50/50,30/70 ratio pDTEc/pDTOc, by mass) were fabricated on a single 42 mm round glass coverslip (VWR, No 1½) by flow coating (**Fig. 3.1**) (246). Briefly, 3 % (mass fraction) solutions of each mixture were dissolved in methylene chloride and 25 mL drops were placed under the blade. The coating conditions were stage acceleration of 25 mm/s^2 , stage velocity of 15 mm/s and a spread distance of 40 mm resulting in films approximately 0.2 mm thick. The substrates were then subjected to a variable temperature heating stage exhibiting a well-defined linear temperature range to induce phase-separation (128). The range and slope of the temperature gradient are tailored through the respective block temperatures and their distance apart. All gradients and control films were annealed for 48 h in air.

The final substrates consisted of five discrete polymer strips (two homopolymer and three blends) on a single coverslip which were subjected to a linear annealing temperature profile orthogonal to the respective compositions. This format yielded "two-dimensional gradients substrates" ("two-dimensional gradients substrates will be used to refer to these substrates with a continuous temperature gradient in one dimension and a discrete compositional gradient in the other). The films were sterilized using ethylene oxide and degassed for 48 h prior to use.

3.2.3 Atomic Force Microscopy (AFM)

Tapping-mode atomic force microscopy measurements were conducted in air with a Nanoscope IV system (Digital Instruments) operated under ambient conditions with standard silicon tips (Nanodevices; L, 125 μm ; normal spring constant, 40 N/m; resonance frequency, (300 to 360) kHz). Images were collected using automated data acquisition every 2.5 μm . Root mean square (RMS) roughness measurements were determined using standard Digital Instruments software; averages and standard deviations were determined from two measurements at each distance from each of two different polymer thin film coated coverslips (n=4). Normalized mean gradients of steepness were calculated for 5 positions at 5 mm intervals for each of the compositional strips. Normalized gradient steepness was calculated with the following formula:

$$\text{Normalized gradient steepness} = \frac{\Delta \text{ RMS Roughness}}{(\text{Physical Distance})(\text{Mean RMS roughness})}$$

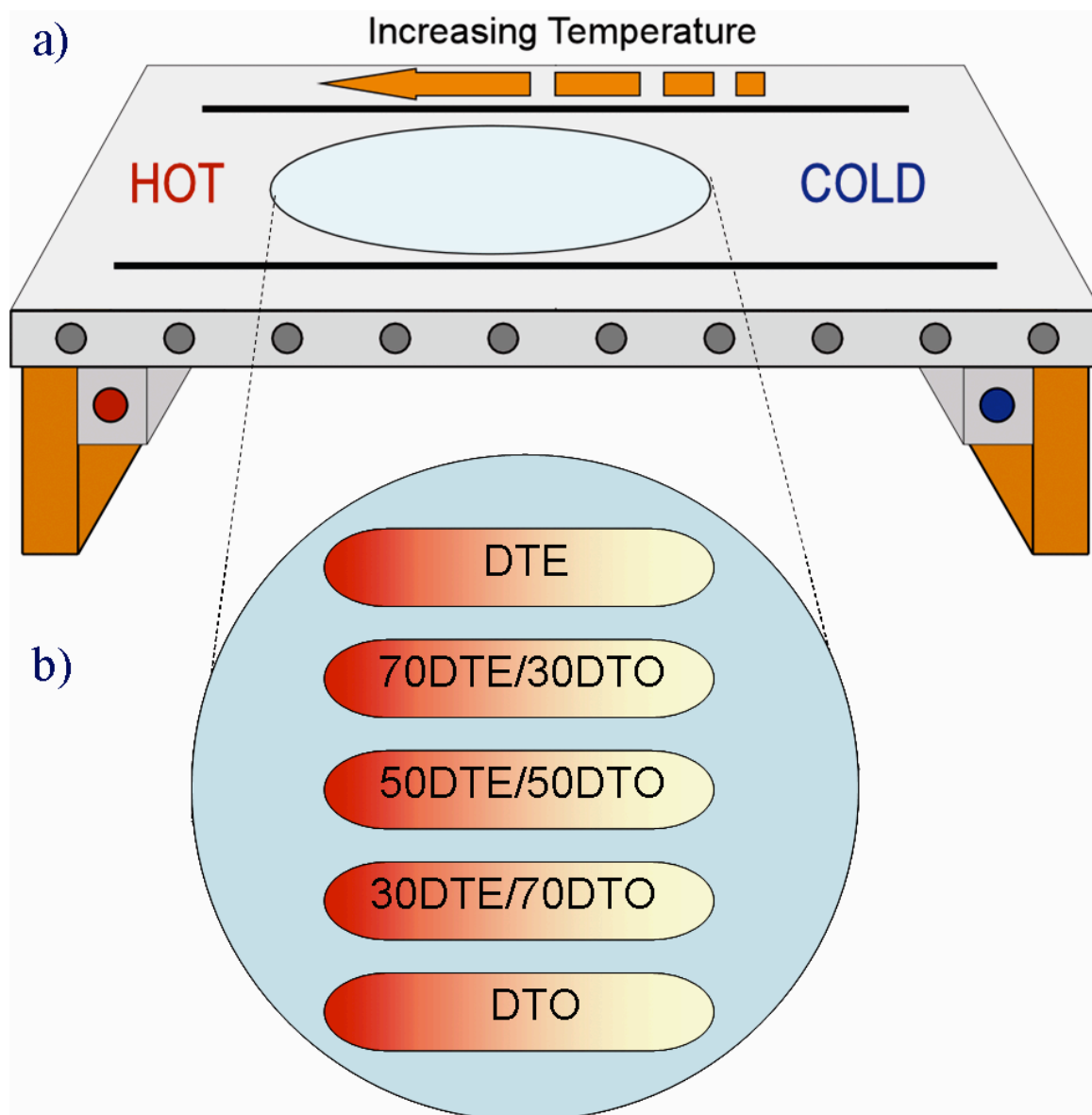


Figure 3.1: Fabrication of 2D orthogonal composition/roughness gradient platform.

a) Schematic of roughness gradient polymer substrate fabrication using the annealing temperature gradient platform. b) Overview of the design of the roughness gradient substrates based on polymer blends. Along the horizontal axis is a continuous temperature annealing gradient; along the vertical axis is the

compositional variation of pDTEc/pDTOc blends. (Figure Courtesy of Dr. Matthew Becker).

Cell culture and Transfection.

Human Saos-2 cells (a gift from Dr. David Denhardt; Rutgers University) transfected with a Green Fluorescent Protein (GFP)-tagged farnesylation (GFP-f) gene were used as a model cell line to probe the morphology and organization of cells cultured on topological gradients of poly(DTE carbonate) and poly(DTO carbonate) blends. The gene that encodes the farnesylation protein is fused with the EGFP gene in the vector (Clontech, Mountain View, CA). 3 SV40 viral promoter is used for the expression of GFP-farnesylation protein in mammalian cells. The farnesylation gene codes for a 20 amino acid sequence, which translates to the farnesylation protein that targets and binds to Ha-Ras, creating the farnesylated Ras protein complex. This binding process is mediated by a farnesyl transferase enzyme, which accompanies targeting of the protein complex to the inner face of the cellular plasma membrane. Because pEGFP is tagged to the farnesylation gene within the same vector, EGFP and farnesylation proteins are co-expressed, and EGFP can therefore be utilized as a visual indicator of activation of the Ras-farnesylation process, as well as an intracellular tracer to track the farnesylated Ras protein complex as it localizes to the plasma membrane. Therefore, using the pEGFP-farnesylation reporter gene provides two simultaneous advantages: 1) a membrane marker, which allows for fluorescent demarcation and resolution of the plasma membrane and is used for morphometric cellular analysis, and 2) an indicator of cell signaling activation related to oncogenic Ras-mediated cell proliferation, which is presented as GFP-f

intensity descriptors, such as standard deviation, mean, maximum, and minimum values of the density (GFP-f fluorescence intensity normalized to cell area). The transfection process was performed as previously described (245). Briefly, Saos-2 cells were propagated in HAM's F12 (F12H) culture medium (Invitrogen, Carlsbad, CA, USA) supplemented with L-glutamine, penicillin-streptomycin, and 10% fetal bovine serum (FBS; Sigma-Aldrich, St. Louis, MO, USA). Cells were transfected with Lipofectamine™ supplemented with PLUS™ reagent (Invitrogen), and stable lines were selected using 0.5 mg/mL G418 (Sigma-Aldrich). Saos-2 GFP-f cells were cultured in flasks (75 cm² surface area) at 37 °C in a fully humidified atmosphere with 5 % CO₂ in F12H (Invitrogen, Carlsbad, CA) supplemented with L-glutamine, penicillin-streptomycin, and 10 % fetal bovine serum (Sigma; St. Louis, MO). Medium was changed twice weekly and cultures were passaged with 0.25 % Trypsin EDTA (Lonza Inc., Walkersville).

3.2.4 Confocal Microscopy and Imaging

Saos-2 GFP-f cells were cultured on the roughness gradient substrates and incubated for 24 h at 37 °C. Live cell, real-time imaging was performed within a temperature controlled POC chamber retrofitted on the motorized stage of a Leica TCS SP2 confocal laser scanning microscope (CLSM) (Leica Microsystems Inc. Exton, PA). Green fluorescent images of cells were acquired using a 488 nm excitation with a 500 to 535 nm emission bandpass filter. All image frames underwent two line and frame averaging. For higher throughput cell attachment and adhesion imaging, tile-scanned CLSM images were obtained at low (10X objective, numerical aperture (NA) =0.7) magnification over a 2.5 mm

x 30 mm region (n = 6). For high-content imaging, single cells were viewed under high magnification (63x oil immersion objective NA=1.3) for the quantification of morphologically based cell descriptors (Image Pro Plus, Silver Spring, MD) and functional data (e.g. cell attachment and spreading). For the high-content imaging 15-30 cells per position (5 positions per composition) were examined for two independent substrates (n = 2).

3.2.5 Degree of Cell Attachment

Cells were seeded (6000 cells/ cm²) on polymer gradient substrates and incubated for 24 h (n = 2). The culture medium was removed and the disks were washed carefully with PBS to remove any unattached cells. The roughness gradients underwent tile scanning as described previously. The total number of cells within a region was determined.

3.2.6 Degree of Cell Adhesion Strength

The cell adhesion strength was quantified by determining the centrifugal force required to detach a critical fraction of adherent cells from the respective position on the gradient substrates. Cells were seeded (6000 cells/ cm²) on the gradient substrates and allowed to adhere for 1 h. Samples were then inverted and plates were filled with 1x DPBS solution (Lonza Inc.). The substrates were subjected to stepwise increases in centrifugal force ((200 to 800) rpm, corresponding to (9 to 146 x g) in a Beckman centrifuge for 5 min at room temperature. The number of adherent cells remaining on each surface was determined microscopically in six random positions on two independent samples (n = 2). The mean detachment

force required to remove a critical fraction of adherent cells was calculated from the following relationship: $f = RCF \times V_c(\rho_c - \rho_m)$, where RCF is the centrifugal force applied to the samples, V_c is the volume of a cell, and ρ_c and ρ_m are the densities of a cell and the medium respectively (247).

3.2.7 GFP-Farnesylation Based Morphometric Descriptors of Single Cells

Individual cell images of GFP-fusion protein expressing cells acquired through confocal microscopy were exported to Image Pro Plus (Version 5.1 for windows, Media Cybernetics, Inc., MD, USA) for morphometric descriptor generation. Image processing algorithms included contrast enhancement, low pass/sobel/flatten filtering, intensity-based thresholding, morphological operations, and parameter measurements. 15-30 cells examined from each position were used to calculate a population distribution for each descriptor.

The GFP-f descriptors were analyzed in two ways. The first utilized the ability of GFP-tagged farnesylation protein to fluorescently demarcate the plasma membrane. This analysis was not affected by variations in GFP-f fluorescence intensity, but was valid as long as the plasma membrane demarcation could be identified through image processing algorithms. It was possible to measure the cell boundary through membrane demarcation at even minimal fluorescence signaling around the plasma membrane. This analysis provided various cellular morphologic parameters: area; perimeter; lengths of major and minor axes of the ellipse circumscribing the same geometric area of the cell; mean radius; mean diameter; roundness; protrusions; protrusion length; mean feret length; maximum feret length; and minimum feret length. The second mode of analysis scrutinized

the variation in GFP-f fluorescence intensity within a single cell area. This analysis relates to the level of intracellular expression of the farnesylation protein and to Ras-mediated cell signaling activity, as described above. It provided us with another class of descriptor parameters: mean, sum, and standard deviation of density (GFP-f fluorescence intensity normalized to cell area); margination; heterogeneity; and clumpiness.

All descriptors listed were calculated utilizing standard object descriptors provided with Image Pro Plus software. SPSS statistical software (SPSS; Chicago, IL, USA) was then used to determine which high-content descriptors correlated best with surface roughness and cell attachment on the gradient surfaces. Bivariate correlation coefficients were computed relating each of the descriptors with surface roughness and cell attachment. Correlation coefficients that were found to be statistically significant ($p < 0.05$ unless otherwise noted) were extracted for further analysis.

3.2.8 Statistical Analysis

Statistical analysis was performed on morphometric parameters using SPSS software and included analysis of variance (ANOVA) with Tukey's HSD post hoc method and other multivariate statistical tools. The differences were considered significant for $p < 0.05$ unless otherwise noted. Error bars indicate the standard uncertainty around the mean.

3.3 Results and discussion

3.3.1 Two-dimensional gradient fabrication

Significant efforts have been expended to develop a versatile platform capable of varying one or more material properties with well-defined spatial constraints for biomaterials applications. However, unexpected physical and chemical variations which occur during the material processing remain a persistent challenge (128). These variations impede a correlation-based interpretation of biological events. The combinatorial platform presented in this study was designed to vary two material properties (i.e., surface topography and chemical composition) in a two-dimensional gradient platform (**Fig. 3.1b**). This platform affords the simultaneous evaluation of the topographical changes that present themselves during the phase separation process within a series of discrete blend compositions. Unlike current microarray-based methods (137) for the concurrent assessment of hundreds of potential biomaterials, the orthogonal gradient approach in this study focuses on the detailed examination of the effects of two material properties; surface topography associated with phase separation and composition, on cellular responses within a single substrate.

The phase-separation technique has been utilized to produce a variety of surface features in polymer blends (128, 129, 134, 241-243). Unlike other technologies, including laser ablation (248, 249), helium irradiation (250), and imprint lithography (238), which produce discrete topographical features on polymer surfaces, this temperature gradient method produces a wider variation in

surface properties. The demixing process was induced by annealing the blends of pDTEc/pDTOc on a hot stage possessing a linear temperature gradient. This resulted in a composition-dependent change in the surface roughness and surface-available phase fraction, which were determined by AFM measurements (**Fig. 3.2**). The slope of the roughness variation was determined mainly from the pDTEc content in the blend. Phase separation is a kinetically controlled process and as the temperature of the thermal stage approached the glass transition temperature (T_g) of the pDTEc (99.2 ± 0.7 and 52.6 ± 1.6 °C for pDTEc and pDTOc respectively) (242) the demixing process slows appreciably. The phase-separated surface of 50/50 pDTEc/pDTOc blends exhibited RMS roughness values ranging from 68 nm to 5 nm. Similar pseudo-linear curves with varying slopes in the surface roughness were observed on 70/30 and 30/70 pDTEc/pDTOc blends with RMS roughness values ranging from 35 nm-5 nm and 50 nm-5 nm, respectively (**Fig. 3.2**). The reproducibility and the pseudo-linear increase in the surface roughness that were demonstrated in this study indicate that the temperature gradient technologies can be utilized as a reliable property-controlled gradient platform. Complicating the trend elucidation is the fact that the respective components of the phase-separated surfaces exhibit markedly different behavior. The variable annealing temperature procedure yields a profile that possesses various amounts of each phase at the surface. As the individual components each have different protein adsorption behavior, the variable profile has rich physico-chemical phase space. Composition control in the form of discrete blends simplifies further the potential chemical variability.

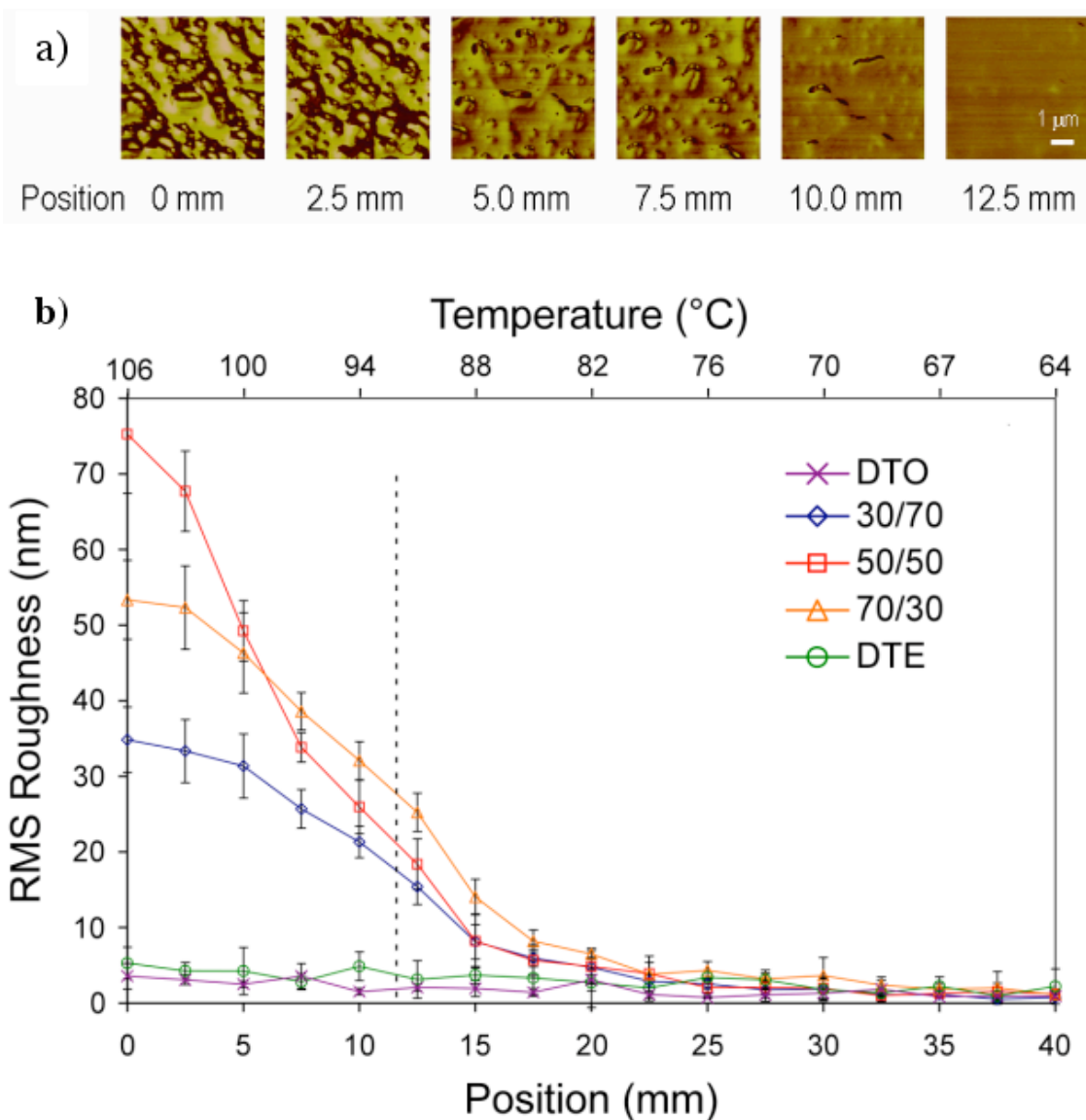


Figure 3.2: Surface roughness characterization of gradient substrate with AFM tapping mode

a) AFM phase images were taken along 30/70 pDTEc/pDTOc roughness gradients at an interval of 2.5 mm. The five positions selected are represented by p1 through p5. b) Comparison of different RMS roughness (computed from AFM height images; $n=4$) along annealing temperature gradients of the respective pDTEc/pDTOc blend compositions. The RMS roughness of the

respective polymer blends decreases monotonically with composition as the temperature approaches the glass transition temperature of p(DTE)c. The RMS roughness of homopolymers (pDTEc or pDTOc) stays constant at 1~5 nm along annealing temperature gradient. The dotted vertical line indicates the extremity of the range of roughness conditions shown in Panel (a). (Figure provided by Dr. Matthew Becker).

3.3.2 Cellular attachment and adhesion evaluation

Rapid screening of cell population-level adhesive responses was conducted through tile-scanning of images of Saos-2 GFP-f adherent cells to different regions of the polymer roughness gradients. Cells were found to attach in greater numbers to the pDTEc than to the pDTOc (**Fig. 3.3 and 3.4**). As both homopolymer surfaces were relatively smooth, these variations in cell attachment are likely due to differences in polymer hydrophobicity (242) and protein adsorption. The homopolymer pDTOc has a longer hydrocarbon pendant chain and is more hydrophobic than pDTEc. This result is consistent with previously reported *in vitro* and *in vivo* studies (215, 216, 242) demonstrating an inverse correlation between cell adhesion, spreading, and growth, and polymer hydrophobicity. With regards to surface features, Washburn *et al.* (133) reported that cells on the 12 nm rough surface exhibited increased spreading, more readily entered into the proliferative S-phase, and showed more profuse F-actin organization compared to those on the 1 nm rough surface. This study suggests that cell proliferation and cytoskeletal organization are controlled by the nanometer scale topography. The present study showed that for a given blend composition, the cell attachment increased monotonically with the degree of surface roughness until the RMS value reached 30 to 40 nm in the 50/50 pDTEc/pDTOc blends. However, cell attachment to the surfaces with RMS roughness values greater than 40 nm was diminished. While, a similar pattern

was observed for cell attachment on 70/30 and 30/70 pDTEc/pDTOc blends, the greatest overall cell attachment was observed on the 50/50 blends.

Further, we observed that the locations in the pDTEc/pDTOc blends with the most significant changes in topographical slope, about (5 to 10) mm along the roughness gradient, exhibited RMS roughness values of (30 to 40) nm and maximum cell attachment. Whether the roughness gradient steepness is a significant determinant of cell attachment and spreading remains to be confirmed. Our substrates presented both varying roughness and roughness gradient steepnesses on different blend compositions, so the roles of roughness and the gradients need to be decoupled. We examined whether cell adhesion profiles are governed by a specific gradient steepness of roughness, an index defined as steepness of roughness gradient divided by average degree of local roughness (**Fig. 3.4**). This index allows comparison of roughness gradients over regions of varying average roughness. Three trends appear to emerge. In general, regions with greater specific gradient steepness of roughness correlated with increased cell adhesion, suggesting that (apart from degree of roughness), the degree of gradient of roughness is a likely determinant of cell response. Second, the slope of the linear best fits to **Fig. 3.4** (see equations in caption for **Fig. 3.4**) was greatest for the 30/70 pDTEc/pDTOc blend composition, suggesting that the gradient steepness has the most pronounced effect on cell adhesion on the pDTO-rich blends, consistent with the notion that the homopolymer pDTOc elicits lower levels of cell adhesion. Finally, the 50/50 pDTEc/pDTOc blends showed variable cell adhesion for similar values of specific

gradient steepness, suggesting that the roughness gradient steepness is a weaker determinant than the average degree of roughness and blend chemistry for this blend composition. The 50/50 blends had the greatest overall cell adhesion (**Fig. 3.3 and 3.4**) at comparable roughness and lower roughness gradient steepness than the other blends and greater adhesion than either of the homopolymer substrates. This seems to support the dominance of blend chemistry in cell adhesion behavior in the 50/50 composition.

The degree of cell adhesion strength was measured indirectly by counting the number of cells that still remained on the substrate after differential centrifugal fields (**Fig. 3.5a-b**). The detachment curves demonstrated that the cells adhered more strongly to the rough surfaces than the smooth surfaces for a given composition; this was indicated by the decreased absolute value of the slope of the detachment curve, as compared to the slope of graphs obtained from the smoother surfaces in **Fig. 3.5**. Notably, cells adhered more strongly to the 50/50 pDTEc/pDTOc blends than to pDTEc, indicating that polymer composition and roughness can cooperatively sensitize cell adhesion and cytoskeletal organization. Our rapid screening studies also revealed that cell adhesion force increased monotonically with the surface roughness of the substrate on all the blends (**Fig. 3.3**). In contrast, we found biphasic patterns in both cell attachment and spreading, as evidenced by the fact that both cell attachment and spreading increased significantly at the position with intermediate roughness (RMS value: ~ 40 nm) as compared to other positions with higher or lower levels of roughness.

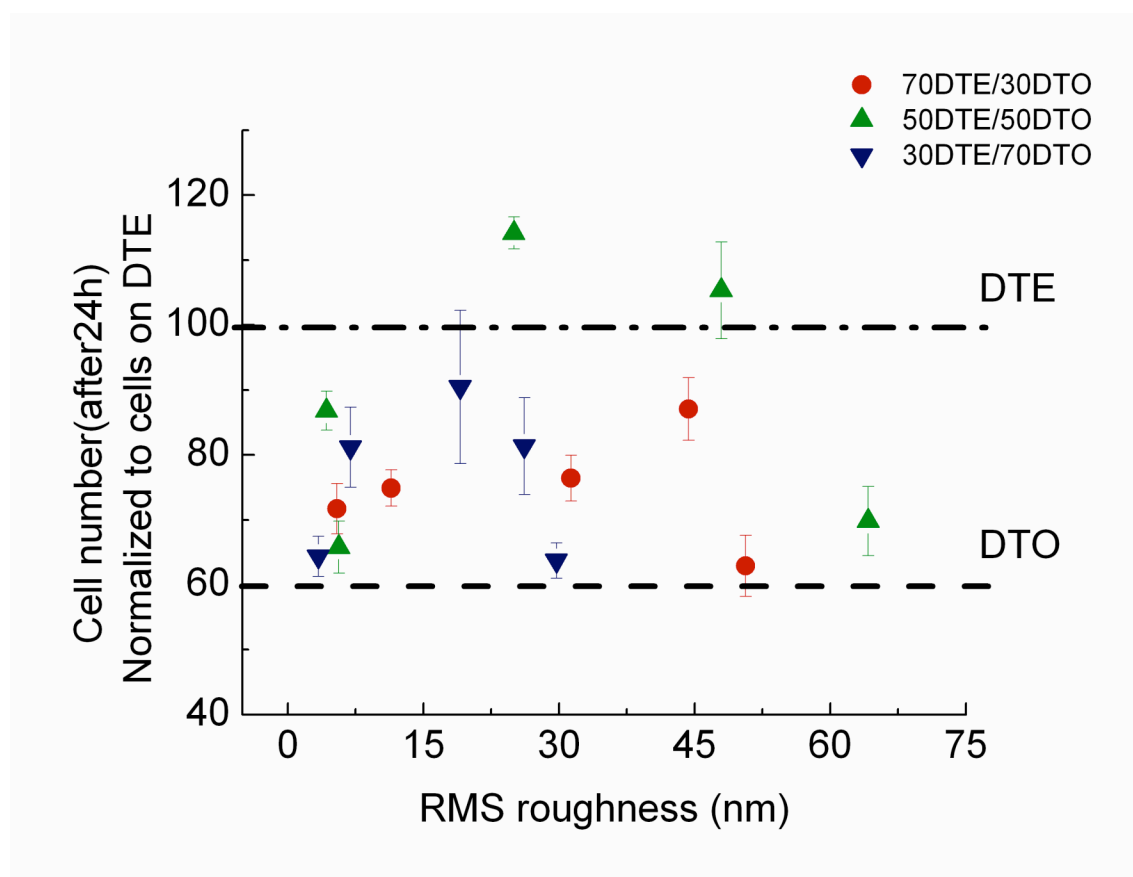


Figure 3.3: Degree of cell adhesion (24 h) was plotted versus RMS roughness on the substrates with roughness gradients.

Cell adhesion was analyzed at 5 different locations spaced 5 mm apart for each compositional strip. The number of cells attached along the roughness gradient displayed a biphasic correlation with the RMS roughness of the substrate surface.

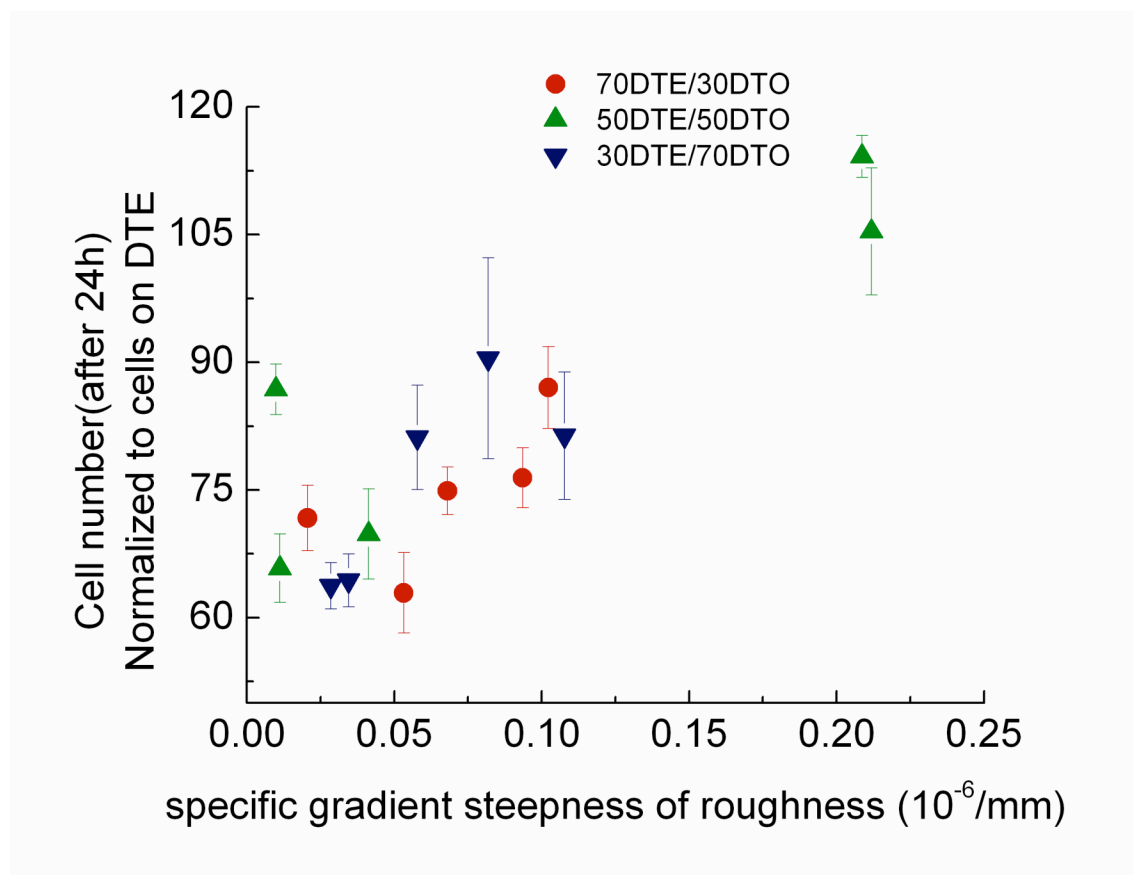


Figure 3.4: Cell adhesion (24 h) was plotted versus the specific gradient steepness of roughness, an index that corrects for varying degrees of roughness in different regions of the gradient steepness.

The number of cells attached to different positions on the substrates and different blend compositions are correlated with the “normalized” gradient steepness of the substrate surface. The best fit equations for the three compositions are:
 70DTE/30DTO: $y=62.3+182.45x$ $R^2=0.69$; 50DTE/50DTO: $y=70.87+181.54x$ $R^2=0.89$; 30DTE/70DTO: $y=58.65+283.25x$ $R^2=0.80$

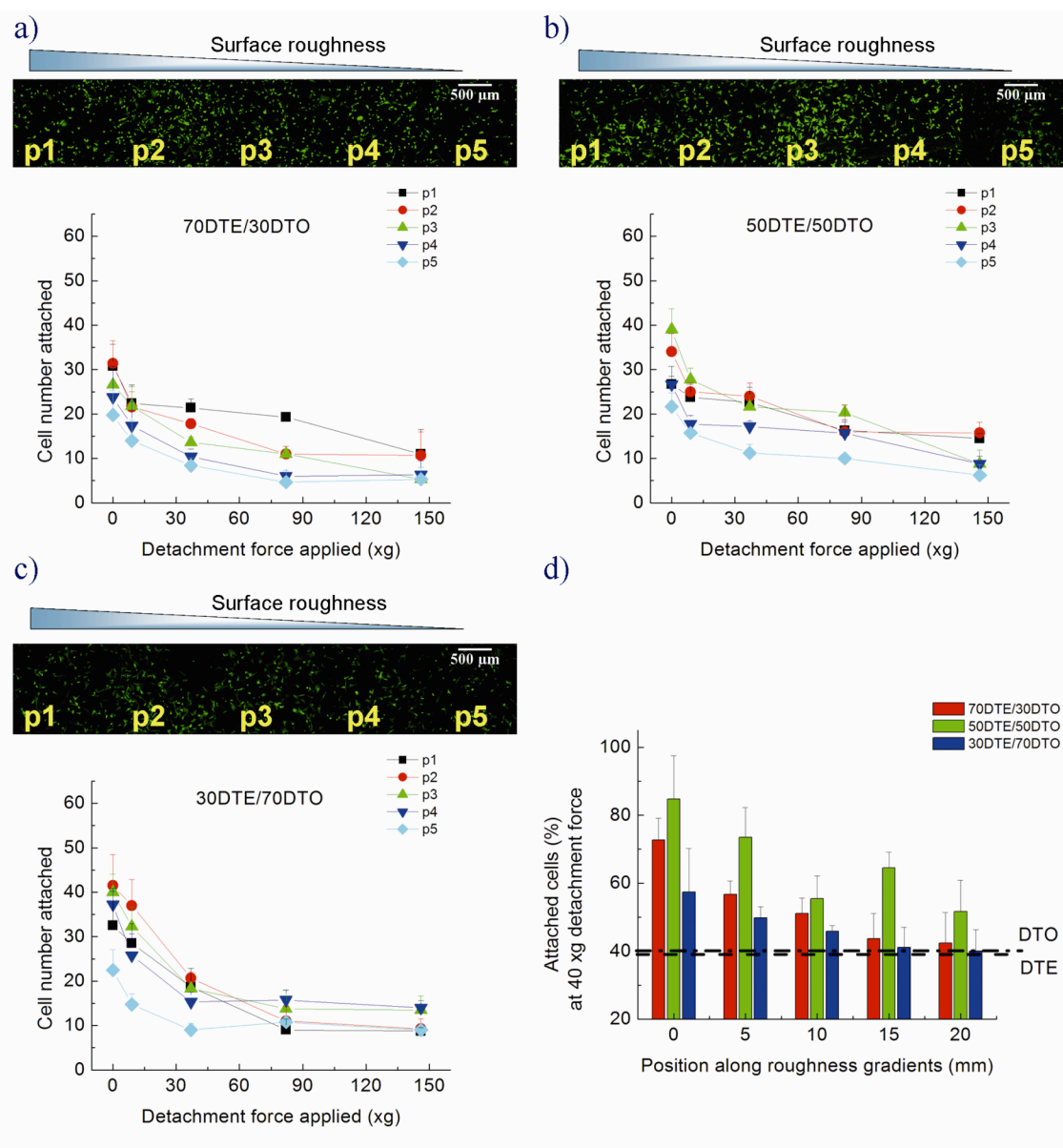


Figure 3.5: Saos-2 GFP-f cell adhesion force measurement using high throughput imaging.

(a-c) Saos-2 GFP-f cells were seeded on roughness gradients, incubated for 1h and centrifuged at 200~800rpm (9~137xg). Tile-scans were constructed for each of the substrate gradients with the 10x objective of a Leica TCS SP2 CLSM/MPM microscope. Cell number of GFP fluorescent cells was

determined by counting the number of fluorescent cells remaining. The 5 positions noted (p1-p5) refer to 5 positions (see **Fig. 3.2**) along each composition spaced 5 mm apart. Position 1 corresponds to the roughest portion of the gradient, while position 5 corresponds to the smoothest. A montage of the gradients of each pDTEc/pDTOc composition after centrifugation was reconstructed based on the tile-scanned images (1.5 x1.5 mm) in ImageJ. A single example of one of these montages before centrifugation is shown for the 70/30, 50/50 and 30/70 pDTEc/pDTOc blends (a-c respectively). The tile scan images were then used to determine the number of cells remaining after centrifugation under differential forces for the respective blends. The cell adhesion force monotonically increased with RMS roughness of the surface within individual compositions. (d) The number of cells remaining after application of 40 xg detachment force was compared across polymers. The 50/50 blend demonstrated the greatest adhesion force at 40 xg

The mechanistic factors underlying the role of roughness on cell adhesion and spreading are not entirely clear. However, one key link may be through the regulation of adsorbed extracellular matrix proteins from the culture environment, which in turn may be altered on microphase-separated substrates with varying chemistry and hydrophobicity. A number of published reports as reviewed by Wilson et al. indicate that the nano-scale surface roughness regulates the cell attachment and adhesion force through protein adsorption onto the substrate surface: the geometry and chemistry that are changed by the roughness formation can influence the concentration, conformation, and activity of the adsorbed proteins (251).

3.3.3 High-content Single Cell Imaging on Substrates with Roughness Gradients

Cell population level differences on substrates with incremental variations in surface physiochemical properties can be too subtle to be captured by high throughput or rapid screening. For such applications, information-rich high-content imaging is called for. Recently, Treiser et al. published a technique whereby quantitative descriptors of cell morphology are used to parse cell response to combinatorial polymer materials with differing chemistry (245). This study employed a similar technique to identify descriptors of cellular morphometry, which were responsive to changes in the substrate roughness.

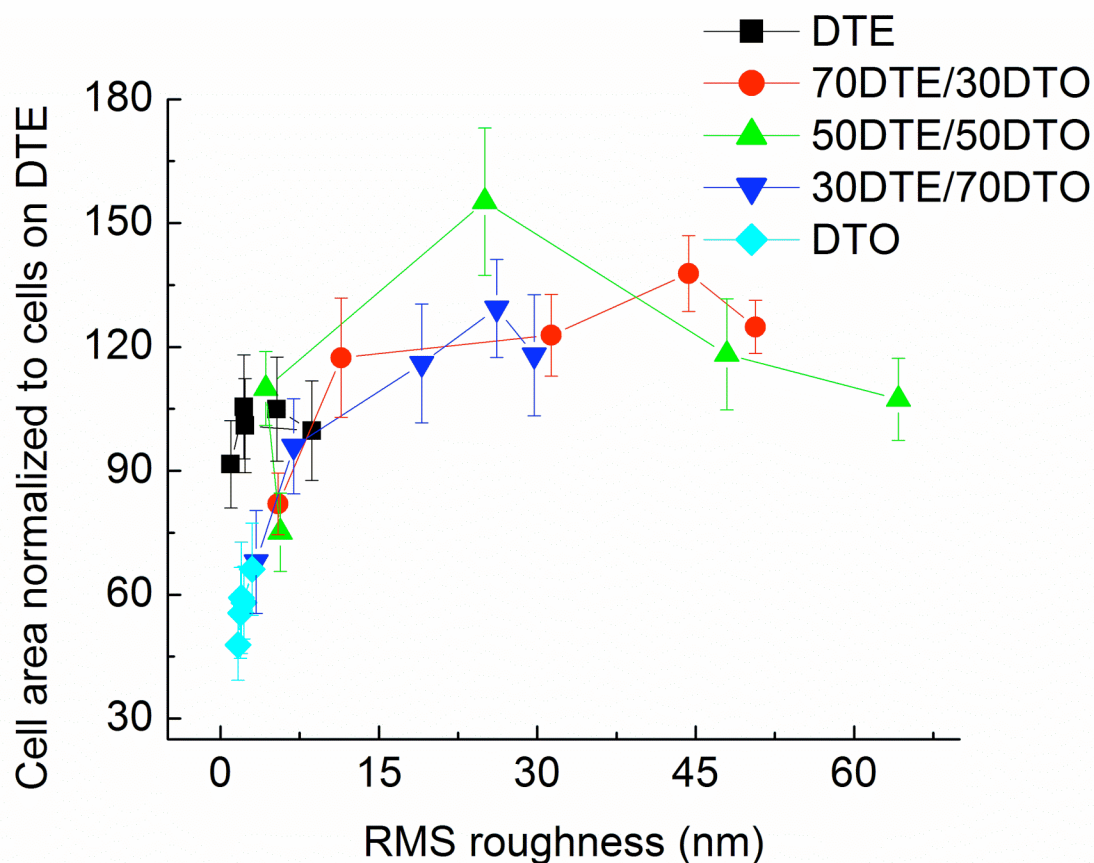


Figure 3.6: Normalized cell area versus roughness.

Cell area was utilized to characterize the spreading behavior of Saos-2 GFP-f cells cultured on the two dimensional gradients for 24 hours. Similar to 24 h cell attachment, Saos-2 GFP-f cell spreading displayed a biphasic correlation to surface roughness across compositions with intermediate roughness promoting the largest cell areas. (n =15 to 30 cells per condition).

The high-resolution imaging of the single cells and quantitative image analysis were used to screen the multiple cellular responses to the roughness gradient surfaces. The cell morphology and spreading changed continuously along both the roughness gradient axes (**Fig. 3.6**). At the smooth end of pDTEc-rich compositional regions, the cells spread more relative to the hydrophobic pDTOc-rich surfaces. This finding is consistent with reports from a previous study (215). The fact that pDTEc increases cell-substrate adhesion more than cell-cell cohesion as proposed by Ryan *et al.*(252) might account for the different cell behaviors elicited by the two polymers. The maximum cell spreading was observed at the intermediate position at RMS roughness of (30 to 40) nm in the 50/50 pDTEc/pDTOc blends.

The Saos-2 cells were cultured on pDTEc/pDTOc blends with roughness gradients, and the cell areas were computed (**Fig. 3.6**). The surface roughness behaved in a threshold-like manner; regions containing RMS roughness values greater than 5 nm resulted in larger cell areas for the textured pDTEc/pDTOc blends as compared to the non-textured homopolymers. The RMS roughness exceeding 5 nm led to no significant difference in cell area. In fact, while the surface features ranged from 4.3 nm to 64.2 nm in RMS height (positions located (0 to 15) mm), the cell area remained relatively constant except in a few positions on the 50/50 roughness gradient. One of the key findings of our high-content imaging is that, whereas the cell area is responsive to the "presence" of surface

topography (243), it lacks sensitivity to differences in nanometer scale surface features (134).

Because the cell area correlated poorly with changes in the surface roughness, high-content image processing and statistical analysis were particularly valuable to potentially identify other cell morphometric parameters that were sensitive to the changes in roughness within individual chemistries. We found two such parameters: "perimeter length" of GFP-f on the 70/30 and 30/70 pDTEc/pDTOc blends, and the "standard deviation of the intracellular intensity" of GFP-f on 50/50 pDTEc/pDTOc blends, which correlated well with the changes in the surface roughness (**Fig. 3.7**). While the perimeter is often used in combination with cell area to measure cell spreading, we report that only the cell perimeter length was responsive to the surface roughness. Since surface roughness can modulate cell response by affording increased anchor sites for cellular membrane processes, (253, 254) the changes in the membrane function of the Saos-2 cells might be guided by the roughness gradient and then coordinate changes in global cell shape. The protein farnesylation has been implicated in alteration of both the cytoskeleton organization and cell functions via the activity changes of the Rho and Ras protein family (255, 256). An activation of this protein family and their downstream effectors is an important event in the actin-myosin operation and focal adhesion assembly, both of which play a significant role in actin cytoskeleton organization and cell adhesion (191-194). The standard deviation of farnesylation intensity, the second high-content parameter that our analysis yielded, may reflect some aspect of cellular

farnesylation activity and thus implicate a direct or an indirect role for protein farnesylation in the signaling events downstream of cell adhesion to our gradient substrates. It should be noted that this parameter was correlated with the variations in the surface roughness of the 50/50 blends, but it was not as well correlated on the other compositional blends. Interestingly, the 50/50 blends were the substrates that elicited the greatest increase in cell response to the increase in surface roughness. Of note, while the statistically significant ($p < 0.05$) correlation coefficients for surface roughness were found for all of the blends, the value of the coefficients was low (< 0.90) for the 70/30 and 50/50 pDTEc/pDTOc blends (**Figure 3.7**). The pDTEc represents a polymer surface composition that promotes favorable spreading and attachment of cells in comparison to pDTOc (215). The low values of the correlation coefficients for the blends with ≥ 50 % pDTEc content may indicate that the increased presence of pDTEc lowers the ability to resolve cell morphologic changes that result from roughness alone. This would imply that the chemistry effect of the pDTEc dominates over the changes in the surface roughness. However, in polymer conditions composed largely of pDTOc (30/70 blends), the surface roughness effects on cell morphology may be resolved.

A major challenge in biomaterials characterization remains how to relate qualitative and quantitative changes in cell morphology to biological functions of interest. While the cell area provides a qualitative measure of cell behavior, quantitative correlations and the possibility that other cell morphometry-based descriptors will correlate with greater sensitivity and accuracy must be explored.

By utilizing high-content imaging, descriptors that correlated best with 1 h cellular attachment were identified (**Fig. 3.7**). Briefly, a bivariate correlation coefficient was calculated (Pearson correlation coefficient) utilizing SPSS software. Correlation coefficients that were found to be statistically significant ($p < 0.05$) were flagged and identified. The heat map compares the descriptors on all of the surfaces against those on single smooth control surfaces, but it does not make comparisons among the different degrees of roughness. Therefore, while the descriptor can be statistically different on all values of roughness versus the smooth surface, they could all have the same value on the different values of roughness and therefore have a poor correlation coefficient. Since the heatmap does not represent the value of the descriptor, it alone is not able to identify which descriptors best correlate linearly with roughness, hence necessitating the use of statistical analysis. Overall, the cell area was found to be a reliable predictor of cell attachment on the 50/50 blends but was not well correlated with attachment on the 70/30 and 30/70 pDTEc/pDTOc blends. However, the cell roundness and the length of the major axis of cells correlated with the 1 h cell attachment on the 70/30 and 30/70 pDTEc/pDTOc blends, respectively. The identification of descriptors that describe cell behavioral polarity as those that correlate best with early cell attachment implicates global cytoskeletal organization as a dominant mediator or effector of early cell attachment to textured substrates.

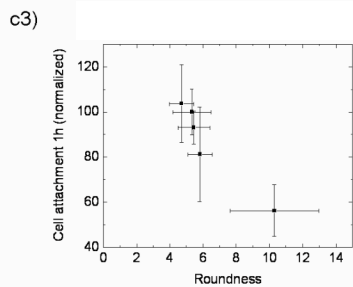
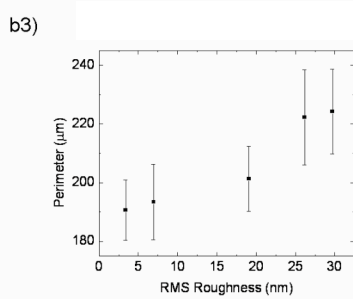
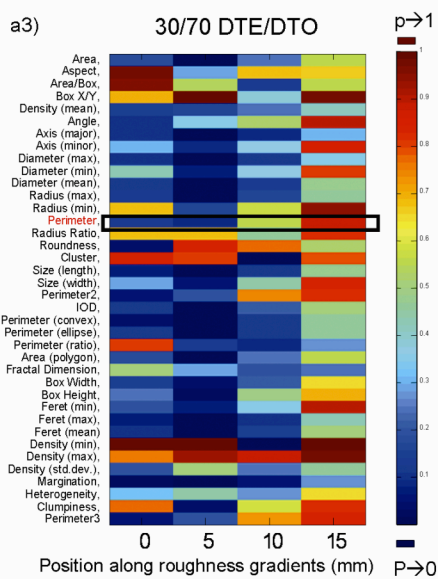
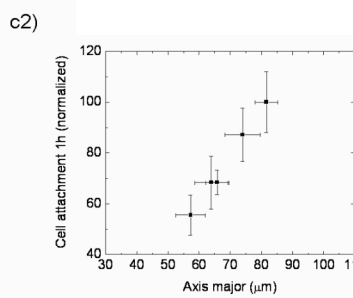
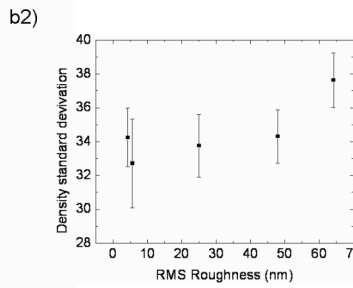
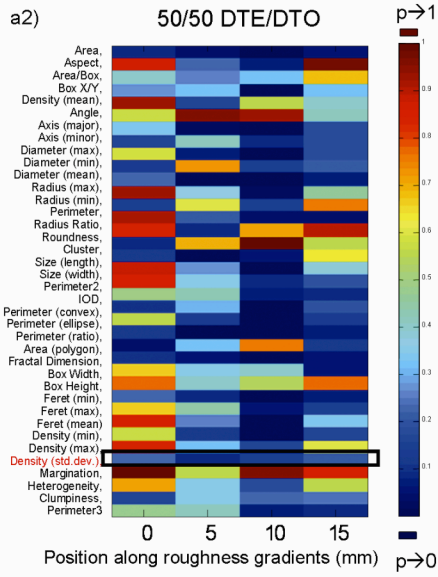
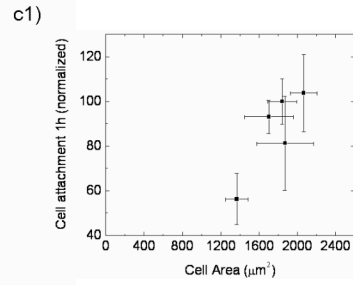
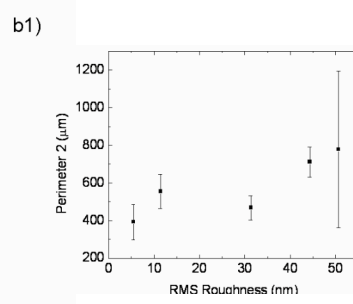
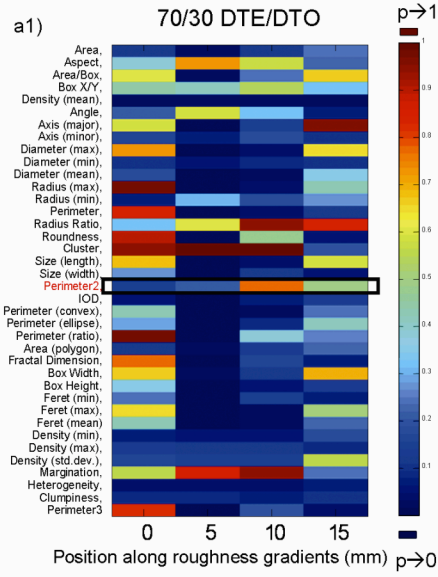


Figure 3.7: Quantitative characterization of cell shape descriptors and morphologic expression of GFP-farnesylation using cell morphometric descriptors.

a*) A 'heatmap' demonstrates the difference along roughness gradients of different pDTEc/pDTOc compositions. Cell population descriptors were determined for cells (15-30 cells per position) cultured at different locations along individual roughness gradient positions (0, 5, 10 and 15 mm) within compositional blends. An ANOVA with post-hoc Tukey's HSD was utilized to determine differences in mean values of cell population descriptors as compared to the mean values of population descriptors on smooth surfaces of the same composition. The "heat map" representation identifies the statistical differences (P-value) between descriptor values comparing positions of increasing roughness and smooth positions utilizing a color-based keying system. A strong statistical difference in descriptor value (ANOVA p value approaching 0) is represented by blue, while no statistical difference (p value approaching 1) by red, an intermediate color between dark blue and red indicates moderate statistical difference (p value between 0 and 1) The heat map does not compare the mean values of descriptors between different levels of roughness within the same compositions, nor do the color bars correlate to the direction of the difference.; b*) Identified descriptors that are sensitive to changes in surface roughness within polymer chemistries. Cell perimeter² (another method of calculating perimeter of a cell), density (GFP-F fluorescent intensity normalized to cell area) standard deviation and perimeter were identified as descriptors that

were sensitive to surface roughness of 70/30, 50/50 and 30/70 pDTEc/pDTOc respectively. c*) Identified descriptors that are well correlated to short term cell attachment. The 1h cell attachment was intercorrelated to cell area, axis major and roundness of 70/30, 50/50 and 30/70 pDTEc/pDTOc respectively. *1) represents polymer blends with 70/30 pDTEc/pDTOc; *2) represents polymer blends with 50/50 pDTEc/pDTOc; *3) represents polymer blends with 30/70 pDTEc/pDTOc.

Perhaps most striking about the presented findings is the identification of individual measures of cell shape that are sensitive to and correlate with surface topography and cellular behaviors. Typical qualitative analysis may identify elongation as a hallmark of surface roughness, but this relationship lacks reproducibility and is insensitive to small changes in material properties. The high-content imaging of cells cultured on the dual-gradient substrates permitted the identification of cell shape descriptors that are sensitive to either roughness or surface wettability (**Fig. 3.7**). The polygonal area of the cell was found to correlate with the surface energy of the material, while the perimeter length of the cell and the standard deviation of the intensity of GFP-f were all found to correlate statistically with the surface roughness. Current studies suggest that cell morphology and the generation of cytoskeletal tension are key regulators of cell function and signaling. Cell studies have highlighted the mechanisms by which the cell shape regulates cell cycle progression, apoptosis, and differentiation (87, 181-183). If cell shape is an essential regulator of cell response to materials, then detailed quantitative analysis of cell morphology, as presented in this study, may provide new insights to determine how material chemistry and roughness interact to produce observable differences in the cell behaviors.

3.4 Conclusion

In this study, we employed both rapid screening and high-content imaging, two complementary approaches, to examine cellular adhesion and morphogenesis on compositionally differing substrate blends of two members of tyrosine-derived polycarbonates that possess a gradient in phase-separation that induces several surface variations including hydrophobicity, individual polymer component and surface roughness. The adhesion of Saos-2 cells was rapidly screened via tile-scanning and was found to be maximized at intermediate regions, characterized by intermediate levels of roughness and the steepest roughness gradient. Through high-content imaging, we identified different morphometric parameters of the organization and intensity of GFP-f that correlate best with the most adhesive substrate compositions (chemistry) or with the degree of surface roughness. We examined the correlations between the defined parameters and the cell functions (e.g. early cell adhesion) obtained by rapid screening. Thus, by using a combination of high-throughput and high-content analysis, we demonstrated that quantitative descriptors of cell fluororeporters can be effectively identified to parse the biologically responsive properties of a library of polymer substrates.

4 High-Content Imaging of Saos-2 Response to Tyrosine-Derived Polycarbonates

4.1 Introduction

Substrates differing in chemical composition promote changes in cellular behavior. This substrate dependent behavior is a result of the outside-in cellular signaling that conveys the extracellular environment to the internal machinery of the cell. Of central interest to biomaterial design remains the elucidation of how the chemical, physical and biological properties of a material elicit cellular responses (257). Studies have demonstrated that the mechanical properties (89, 90), chemical properties (240, 258) and biological properties (219) of materials influence the cellular response. Currently, biomaterial performance is assessed in a laborious and time-consuming manner where each material is tested with a model cell line. In fact, it is the biological characterization that represents the rate-limiting step in the discovery of novel materials and even in the discovery of new uses for existing ones (123).

Traditionally, two separate methodologies have been proposed to increase the throughput of biological characterization. The first expands the number of materials sampled within a given assay, therefore increasing the total size of the material space explored. This has been completed a number of ways, but perhaps most popular is the synthesis of combinatorial libraries of materials that may then be resolved spatially on a single substrate (128, 134, 136, 241). Another approach rests on the ability to increase the quantity of information extracted per experiment. For example, instead of assaying a cell for a single

behavior (e.g., proliferation, differentiation, or migration), a single assay may be performed that provides information relating to many of these behaviors. Recently, “high content” cell morphological based screening approaches have been developed for the screening of potential pharmaceuticals and biologically active small molecules (160-164). Utilizing these approaches, scientists have been able to increase the information yield of a single assay to 10^8 individual cellular measurements (160). These assays focus on utilizing quantitative descriptors to screen biological compounds of potential interest in a high-throughput manner through multivariate statistical analyses.

High-content screening may also play a role in the study of cell-biomaterial interactions. Perhaps one of the clearest cellular processes influenced by the biomaterials is the spatial and morphological distribution of the cytoskeleton in contact with the substrate. Studies have highlighted the importance of the geometry and distribution of actin filament bundles that transmit the traction forces which cells express during spreading against their substrates (259). The actual spatial and morphological distribution of the cytoskeleton may hold important clues regarding the dynamics of cell spreading, cytoskeletal stiffening, and the nature and efficiency of outside-in signaling. This is because the cytoskeleton mediates contacts both on the outside, through the integrin complexes with extracellular substrates, as well as on the inside through cytosolic signaling cascades involved with second messengers and transcription factors. When cells contact the surface of biomaterials, the cell uses integrins to initiate binding to biomaterials-based matrix ligands, which mediate increases in

cytoskeletal tension, flattening, extension and spreading of the cells (260). The generation of force at integrin binding sites leads to local focal adhesion assembly and activation of signaling cascades and gene transcription events (176, 261-264), as well as to changes to the actin cytoskeleton (180, 221, 265). Therefore, the actin cytoskeleton may represent a “window” through which to characterize a number of biomaterial mediated cellular processes.

Currently, morphometric analysis of the cytoskeleton to culture on biomaterial substrates differing in chemistry has been a key aspect of the biological characterization of materials, but has lacked reproducible, quantifiable results and largely remains in the domain of qualitative observations (134, 154-159). However, recent advances in confocal laser scanning microscopy (CLSM), multi-photon microscopy (MPM) and image processing have provided the tools to adapt this “high content” imaging to cells cultured on biomaterials (165-169). In conjunction with genetic engineering, CLSM and MPM can be used to characterize the morphologic responses of living cells cultured on polymer substrates (159, 266, 267). Simply, genetically engineered cells are cultured on polymer substrates and imaged at high-magnification and -resolution. After imaging, quantitative metrics of the cytoskeletal organization are measured on a cell-by-cell basis. Once these descriptors are obtained, as in the small molecule high-content paradigm, computational methods are needed to extract the meaningful descriptors that best report on cellular behavior.

Utilizing a previously described high-content imaging platform (268), this study focuses on defining strictly quantitative metrics of the actin cytoskeletal

morphology to probe the cellular responses of a model cell line (Saos-2 cells) to a combinatorial library of polymers. Thus, to improve the understanding of substrate induced changes in actin morphology, an imaging based methodology was developed to quantify cytoskeletal changes resulting from culture on polymers of differing chemistry. Quantitative morphological descriptors based on the shape and distribution of cytoskeletal proteins were utilized to highlight how the addition of poly(ethylene glycol) (PEG), charge, and/or iodine alters cellular shape. Finally, computational modeling featuring decision tree (DTs) and artificial neural network (ANN) analyses were employed to determine if Saos-2 behavior might be captured within the actin cytoskeletal organization.

4.2 Materials and Methods

4.2.1 Polymer Nomenclature

Nomenclature for the polycarbonates follows previous published conventions (210-213). Polymers derived from Deaminotyrosyl-Tyrosine Ethyl ester monomers were entitled poly(DTE carbonate)s. Copolymers of x mole% Desaminotyrosyl-Tyrosine Ethyl ester with y mole% Desaminotyrosyl-Tyrosine (DT) and z% PEG₁₀₀₀ were simplified as poly(x%DTE-co-y%DT-co-z%-PEG₁₀₀₀ carbonate). Finally, iodinated copolymers of x mole% Iodinated Desaminotyrosyl-Tyrosine Ethyl ester with y mole% Iodinated Desaminotyrosyl-Tyrosine and z% PEG₁₀₀₀ were simplified as poly(x%I₂DTE-co-y%I₂DT-co-z%-PEG₁₀₀₀ carbonate).

4.2.2 Design of Combinatorial Polymer Library

Tyrosine-derived poly(DTE carbonate) and poly(I₂DTE carbonate) and copolymers with PEG and DT were synthesized according to published procedures (210, 213, 269, 270). The molar fraction of PEG₁₀₀₀ blocks in the copolymer was varied as 0, 4, 8 and 15 mole%. Acid containing monomers of Deaminotyrosyl-Tyrsoine (DT) were alternated between 0 and 10 mole%. Polymers containing DT, PEG and iodine were chosen because of the documented alteration of cellular responses elicited by these chemistries (211, 214, 235). Thus, it was hypothesized that large changes in cell morphology would be promoted by these chemistries therefore providing a suitable polymer test set for the development of the descriptor methodology. Poly(D,L-lactic-co-

glycolic acid) (Resomer 506) and poly(L-lactic acid) (Resomer L-206) were purchased from Boehringer Ingelheim (Ridgefield, CT, USA) (**Table 4.1**).

Table 4.1: List of Polymers For Saos-2 High Content Study

List of Polymers
<ol style="list-style-type: none"> 1. Poly(DTE carbonate) 2. Poly(92%DTE-co-8%PEG₁₀₀₀ carbonate) 3. Poly(85%DTE-co-15%PEG₁₀₀₀ carbonate) 4. Poly(96%DTE-co-4%PEG₁₀₀₀ carbonate) 5. Poly(I₂DTE carbonate) 6. Poly(96%I₂DTE-co-4%PEG₁₀₀₀ carbonate) 7. Poly(92%I₂DTE-co-8%PEG₁₀₀₀ carbonate) 8. Poly(85%I₂DTE-co-15%PEG₁₀₀₀ carbonate) 9. Poly(90%DTE-co-10%DT carbonate) 10. Poly(86%DTE-co-10%DT-co-4%PEG₁₀₀₀ carbonate) 11. Poly(82%DTE-co-10%DT-co-8%PEG₁₀₀₀ carbonate) 12. Poly(90%I₂DTE-co-10%I₂DT carbonate) 13. Poly(86%I₂DTE-co-10%I₂DT-co-4%PEG₁₀₀₀ carbonate) 14. Poly(82%I₂DTE-co-10%I₂DT-co-8%PEG₁₀₀₀ carbonate) 15. Poly(D,L-Lactic-co-Glycolic Acid) 16. Poly(L-Lactic Acid)

4.2.3 Preparation of Spin-coated Polymer Films

Polymers were dissolved into a 1.5% (v/v) methanol in methylene chloride solution yielding a 1% (wt/v) polymer solution. Solutions were filtered through 0.2 μm pore poly(tetrafluoroethylene) filter to remove particulates. Polymer solutions were then spin coated onto 35mm MatTek chambers (MatTek Corp.; Ashland, MA) with a central 15mm tissue culture treated coverslip bottom or onto 15mm glass coverslips (Fisher Scientific). Spin coating was conducted at 2000 RPM for 20 seconds.

4.2.4 Culture of Saos-2 cells on Polymer Coated Glass Substrates

7,400 GFP-actin engineered cells per cm^2 were seeded into sixteen individual polymer coated MatTek chambers in 190 μL of HAMS F12 (Gibco) supplemented with 1mM HEPES (Gibco), 10% FBS (Gibco), Penicillin (250 units)/Streptomycin (250 μg) (Gibco), and 2mM L-glutamine (Gibco) applied to the center cover glass. Cells were allowed to attach in a humidity-controlled incubator at 37°C and 5% CO_2 for approximately 6 hours. After the 6 hour attachment period, the individual MatTek chamber setups were supplemented with 3 mL of HAMS F12 supplemented with 1mM HEPES, 10% FBS, Penicillin (250 units)/Streptomycin (250 μg), and 2mM L-glutamine and cultured for an additional 18 hours in a humidity-controlled incubator at 37°C and 5% CO_2 .

4.2.5 Determination of Saos-2 Cell Proliferation

The percentage of cells proliferating at 24 hours after culture on different polymeric substrates was determined utilizing a commercially available BrdU kit (Catalog # 11299964001, Roche; Indianapolis, IN). Briefly, Saos-2 cells were cultured on polymer coated glass coverslips (described above) for 23 hours in a humidity-controlled incubator at 5% CO₂ and 37 °C. At the 23rd hour, BrdU reagent was added to the media for an additional hour of incubation. After a total of 24 hours of incubation (1 hour with BrdU), cells were fixed and labeled with mouse anti-BrdU antibody. A fluorescein conjugated goat anti-mouse secondary was then used to label the BrdU positive cells. The percentage of cells proliferating was determined via counting the number of BrdU positive cell nuclei versus the total number of nuclei as determined by DAPI counterstaining.

4.2.6 Determination of Saos-2 Cell Mineralization on the Polycarbonates.

Polymer mediated Saos-2 mineralization at 3 weeks was determined utilizing an alizarin red based assay. Saos-2 cells were cultured on polymer coated glass coverslips (described above) that were glued into the wells of a 24 well standard tissue culture polystyrene (TCPS) plate for 3 weeks in a humidity-controlled incubator at 5% CO₂ and 37 °C. To promote mineralization, cells were cultured in complete HAMS F12 media described above supplemented with 50 µg per mL ascorbate, 10 mM β-glycerophosphate, and 10 nM dexamethasone. Media was changed every 3-4 days. After a 3-week culture period, setups were removed and fixed with 4% paraformaldehyde. Mineral was then stained with a 1% Alizarin Red (catalog # A5533; Sigma) in water solution at pH = 4.14. Stained

mineral was solubilized utilizing 10% cetylpyridinium chloride in 10 mM sodium phosphate at pH = 7.0 in water. Solubilized mineral was transferred to a new 96-well TCPS plate and absorbance was read at 570 nm. Background values of polymer only conditions were subtracted for each polymer.

4.2.7 Engineering of Green Fluorescent Protein (GFP) Saos-2 Cell

eGFP-actin plasmids were obtained from commercial sources (Clontech, Mountain View, CA). Saos2 human osteosarcoma cells (a gift from David Denhardt; Rutgers University) were propagated in HAMS F12 (Invitrogen; Carlsbad, CA) supplemented with 2 mM glutamine, penicillin-streptomycin and 10% fetal bovine serum (Gibco; Carlsbad, CA). Cells were transfected with Lipofectamine supplemented with PLUS reagent (Invitrogen) and stable lines were selected using 0.5 mg/mL G-418 (Sigma; St. Louis, MO). Saos-2 cells were chosen for method development because they represented an osteoblastic-like cell type and were easily transfected with the eGFP-actin vector.

4.2.8 Imaging of Engineered Cells on Polymer Films

Confocal Laser Scanning Microscopy (CLSM) imaging was performed on a Leica TCS SP2 system (Leica Microsystems Inc.; Exton, PA). Cell seeded coverglass bottom MatTek chambers were excited at 488 nm and a 500-550 nm band-pass filter channel was used to detect GFP emission. A type HCX Plan APO CS 63x/1.3 glycerol immersion lens was used to obtain high-resolution images of individual cells and their associated cytoskeleton. All image frames

underwent two line and four frame averages. Approximately 20 cells per substrate were imaged.

4.2.9 Image Processing

Individual cell images were processed with commercially available software. Raw images were exported to Image Pro Plus Version 5.1 for windows (Media Cybernetics, Inc.; MD) Images first underwent image enhancement optimization (image contrast, brightness and gamma value adjusting) to equalize image intensity histograms. Contrast enhanced images were then filtered utilizing a ten pass Gaussian filter and then a series of Flatten filters. A pseudo-automated adaptive thresholding process was employed allowing the whole cell and individual actin filaments to be separately segmented based on the image intensity histogram (**Fig. 4.1**). Once either the whole cell or individual actin filaments was segmented, shape and higher order moment parameters were calculated utilizing the count object menu in Image Pro Plus on the segmented objects. In all 60 morphometric descriptors were calculated for each cell.

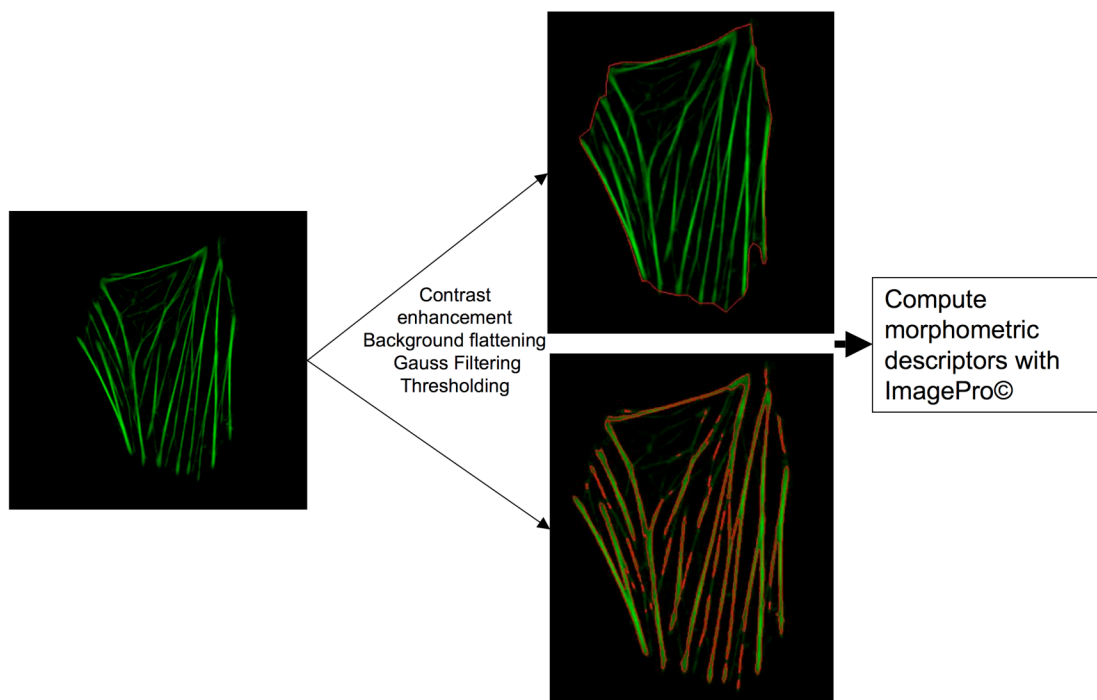


Figure 4.1: Segmentation procedure to compute morphometric descriptors of Saos-2 cells.

Cells first underwent a series of contrast enhancement and filtering protocols. Whole cell and individual actin filament areas of interest were selected utilizing an intensity-based thresholding procedure. Shape and higher order moment descriptors were calculated with ImagePro©.

4.2.10 Decision Tree for Identification of Material Responsive Descriptors.

Decision Trees (DTs) are commonly used computational modeling tools for the description, classification and generalization of data (271, 272). While the use of DTs to structure data occurs in a multidisciplinary domain, since the early 90's DTs have become a valuable tool to biologists and biomedical engineers (273, 274). Decision trees represent a powerful tool for biomaterial science because: (1) they are robust in that they can be applied to discrete, continuous or mixed data; (2) can provide accurate predictions to non-linear data (of which biological data often is); (3) the rules governing predictions are often straightforward; (4) decision trees can be used for description, a process by which the volume of data is transformed into a compacted form that preserves the data characteristics; (5) outliers do not confound the tree predictions (271-275).

Biomaterial scientists have recently utilized DTs to analyze the effects of polymer structure and calculated parameters on the biological response elicited by different substrates. These studies analyzed the description capability of decision trees to reduce large sets (>700) of descriptors to the most meaningful for future modeling approaches (144). The DTs that are involved in descriptor analysis classify data points by starting at the top of the tree (root node) and moving down the tree by creating a hierarchy of descriptor values on an "if-then-else" basis at each branch point until the terminal (leaf) node is reached. In these top-down or greedy constructions the data are recursively divided into subsets based upon the best classifying descriptors at each level. The decision tree algorithm that was utilized in this study was the classification and regression tree

(CART). CART is a DTs based methodology that recursively divides the data into subsets based on the best classifying descriptor at each level. CART utilizes the Ginni impurity as the optimization criteria (271). CART based DTs were utilized to identify those descriptors that are sensitive to distinct alterations of the polymer backbone chemistry. Polymer chemistries were assigned as the output factor with the average morphometric descriptors for each polymer chemistry as the functional input that the CART information gain algorithms utilized to predict descriptor values based on polymer chemistry. All chemistries underwent this type of analysis to identify those descriptors that are most sensitive to certain chemical backbone assemblies.

4.2.11 Artificial Neural Network (ANN) to Predict Polymer Influenced Saos-2 Cellular Behaviors from Early Morphology.

McCulloch and Pitts first proposed ANN's as a computational modeling approach in 1943 (276, 277). Briefly, an ANN utilizes its basic units, analogous to neurons, to associate a response with a specific input pattern (278). This association is developed by the basic units via parallel integration of the input information to determine the activity of each individual neuron (278). This parallel learning process allows non-linear statistical data modeling to correlate inputs with outputs (279). Computational modeling methods, and more recently ANN methods, have been utilized in the field of biomaterials to predict cellular and protein responses as functions of calculated and experimentally determined material properties (141-143, 280-282). This study employed ANN modeling methods to predict polymer influenced Saos-2 cellular behaviors based on early

cell and actin filament morphology. The DTs modeling methods described previously reduced the data set to the most relevant descriptors correlating with cellular behaviors of interest, and then the ANN determined a non-linear statistical relationship between these descriptors and the functional outputs (144) (**Fig. 4.2**). ANN modeling of cellular behaviors was performed utilizing the multilayer perceptron of the freeware WEKA software, developed at the University of Waikato, New Zealand (283).

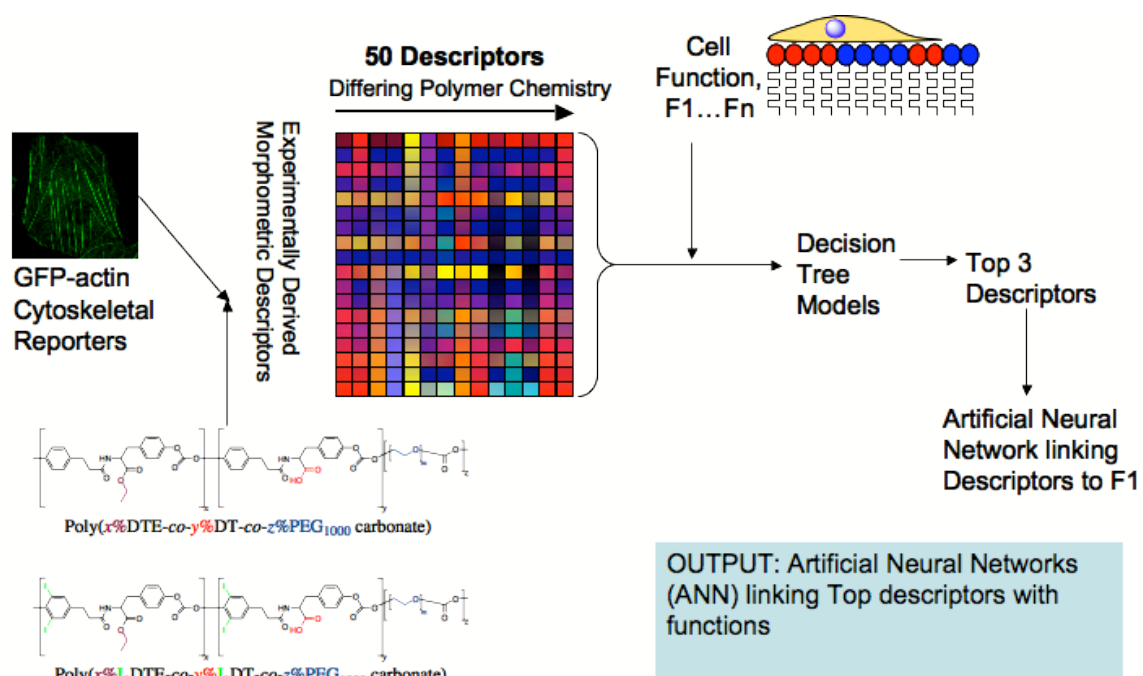


Figure 4.2: Computational approach to high-content morphometric descriptor prediction of Saos-2 cellular behaviors.

eGFP-actin engineered Saos-2 cells were cultured on polycarbonates with differing chemistries. Image based morphometric descriptors of cell and actin filament shape were computed to identify descriptors responsive to the chemical changes. Decision tree modeling is then used to determine the top morphological descriptors that correlate with cellular functions such as mineralization. The top three descriptors from the DTs were then used to train an ANN that could predict Saos-2 polymer-dependent mineralization based on early cytoskeletal morphology.

4.3 Results

4.3.1 Proliferative Response of Saos-2 Cells to Polymer Films

Saos-2 cells cultured on combinatorially derived polycarbonates and poly(α -hydroxy ester)s demonstrate material dependent entry into S-phase at 24 hours of culture (**Fig. 4.3**). If the combinatorial library is broken down by the main alterations of the polymer backbone some interesting correlations are observed. The addition of poly(ethylene glycol) (PEG) to the polymer backbone from 0% to 15% resulted in stepwise decreases in the percentage of cells proliferating at 24 hours. The addition of iodine to the polymer backbone appears to blunt this response. That is, iodination mitigates the resultant stepwise decreases in cell proliferation due to copolymerization with up to 15% by mole PEG₁₀₀₀ seen in their non-iodinated counterparts. Interestingly, while the addition of 10% DT, a charged species at physiologic pH, appears to decrease the percentage of cells proliferating, the combined effect of copolymers containing PEG and DT demonstrate an effect that increases cell proliferation. This seems to imply that while DT or PEG alone decrease Saos-2 cell entry into S-phase, the combination of the two results in an opposite and synergistic proliferative response. When iodine is included with PEG and charge, this opposite synergistic behavior is only seen for the intermediate (4%) PEG levels. Finally, the greatest level of cell proliferation was observed on polymers containing 4%-8% PEG in the presence of DT. This level of proliferation was higher than those recorded on poly(DTE carbonate), PLGA and PLLA.

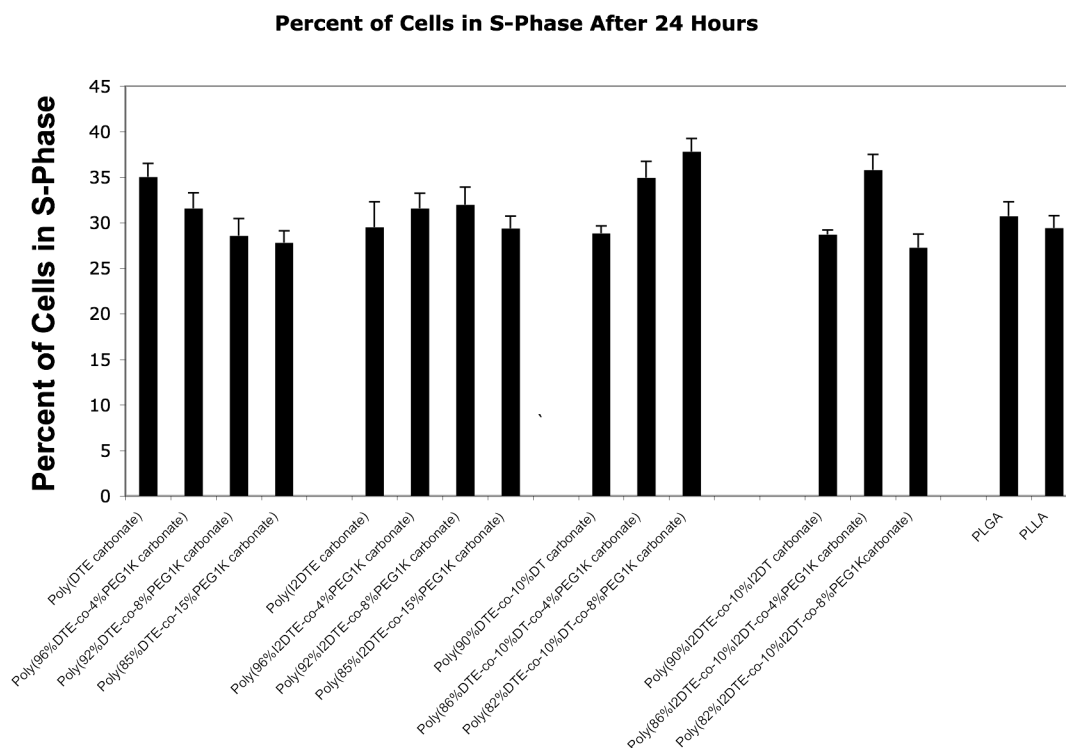


Figure 4.3: Saos-2 proliferative response to tyrosine-derived polycarbonates and poly(α -hydroxy ester)s.

Human Saos-2 cells were cultured for 24 hours on 16 different polymer substrates. The percentage of cells proliferating on each of the materials was assessed by BrdU staining. Error bars represent the standard error of the mean.

4.3.2 Material-Mediated Mineralization of Saos-2 Cells

Human Saos-2 cells are an osteosarcoma cell line that have gained interest in the cell culture community as a cell line that models osteoblastic behaviors. These cells have been shown to exhibit alkaline phosphatase activity, respond to osteogenic hormones, and to produce mineralized tissue (284). Therefore, of interest in the present study was to assess polymer dependent cellular responses in terms of mineralization of these osteoblast-like cells. After 3 weeks of culture on polymer substrates, diverse mineralization responses were observed as assessed by alizarin red S staining (**Fig. 4.4**). Poly(DTE carbonate) and PLLA demonstrated the greatest degrees of Saos-2 mineralization. The incorporation of PEG into the polymer backbone decreased the total amount of mineral when compared to their non-pegylated counterpart. The addition of iodine to the polymer backbone resulted in decreased total mineral production regardless of the PEG content. Similarly, addition of DT to the polymer backbone decreased total mineral production. However, like the proliferative response described above, the addition of PEG to the polymer backbone in conjunction with DT resulted in stepwise increases in total mineral production when compared to the non-pegylated DT containing polymer. Unlike the proliferative response, this synergistic effect does not result in total mineralization levels that are higher than the base polymer lacking charge and PEG.

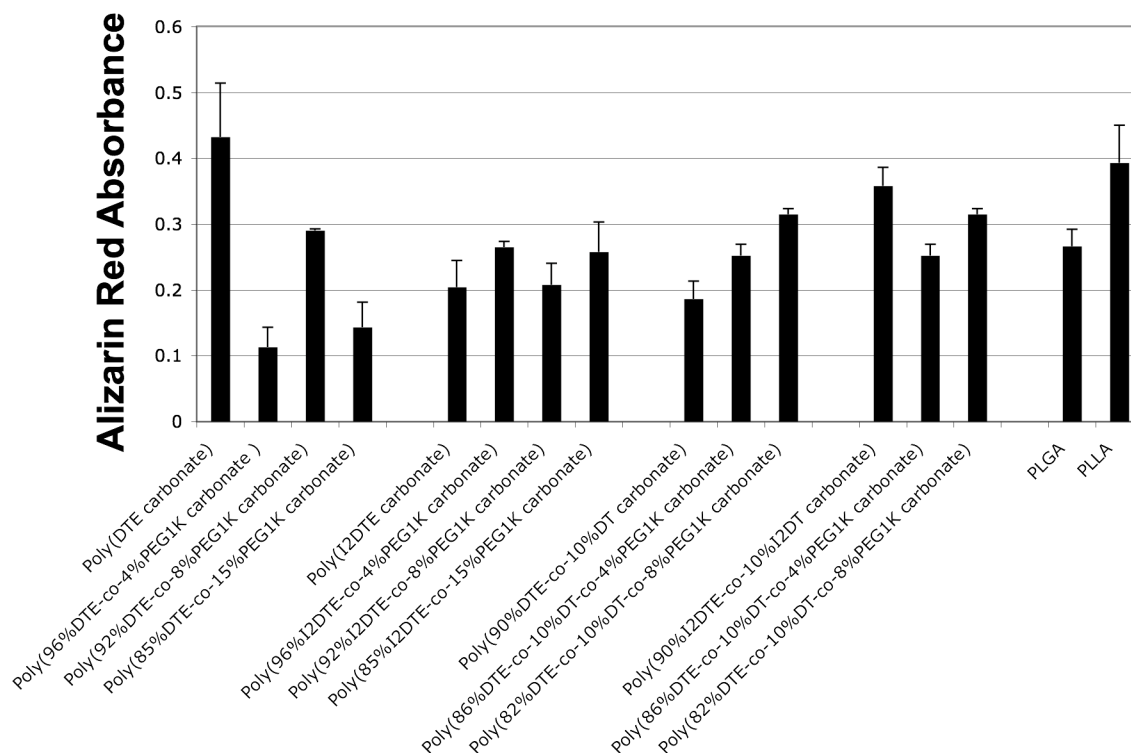


Figure 4.4: Saos-2 3 week mineralization response to tyrosine-derived polycarbonates and poly(α -hydroxy ester)s.

Human Saos-2 cells were cultured for 3 weeks on 16 different polymer substrates. The total amount of mineral present was assessed via Alizarin Red S staining. Absorbance values were background subtracted to account for polymer mineral deposit in the absence of cells. Error bars represent the standard error of the mean.

4.3.3 High-Content Imaging and “Heat Map” Representation of Saos-2 Cells Cultured on a Combinatorially-Derived Family of Polymers

When considering the proliferative and mineralization responses observed on the polycarbonates, it is clear that a complex interplay between backbone components occurs to steer Saos-2 behavior. Unfortunately, deriving correlations between individual monomers and the elicited responses remains difficult giving the high-levels of non-linear trends observed within the data. In an effort to extract more meaningful information regarding cell responses to biomaterials, a high-content morphometric approach was applied. High-content morphometric studies demonstrate that eGFP-actin engineered Saos-2 cells are viable when cultured on polymer coated MatTek chambers and coverslips for 24 hours. The cell seeding density of 7,400 cells per cm² provides adequate cells to attach to all 16 polymers while also maintaining a sparse deployment so as to allow single cell imaging by limiting intercellular contact (**Fig. 4.5**). It should be noted that for some samples the segmentation process requires the user to manually determine the segmentation intensity threshold so as to separate highly overlapping filaments or to segment actin structures that adopted amorphous shapes. Once segmented, morphology-based cell descriptors are calculated utilizing the automatic counting and sizing algorithms available within the Image-Pro software package. Morphologically based cell descriptors are shape parameters/calculations that utilize first and higher order moment intensity

calculations to quantitatively describe features of segmented objects. These descriptors can represent features of the segmented objects (i.e., whole cells and individual actin filaments) ranging from their shape to their spatial distributions throughout cells.

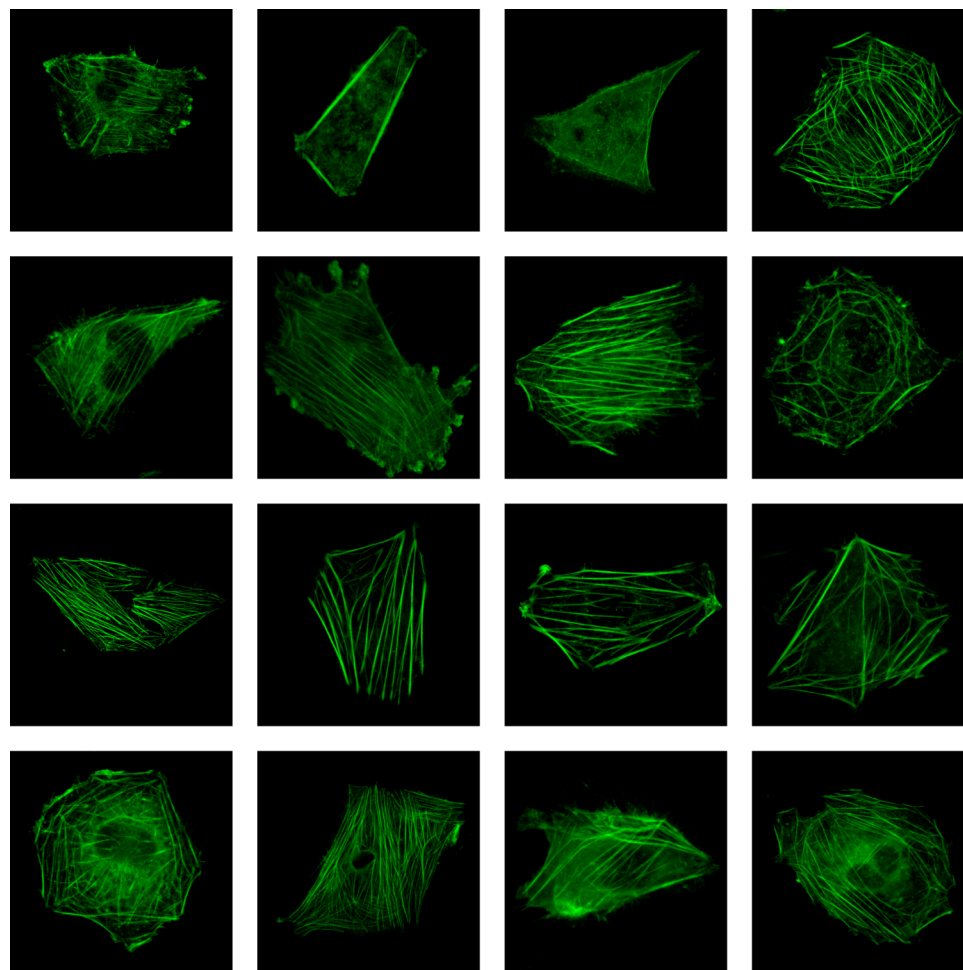


Figure 4.5: Representative confocal laser scanning microscope images of eGFP-actin engineered cells on tyrosine-derived polycarbonates and poly(α -hydroxy ester)s.

These images represent a random cell selected from a heterogeneous population of cells on a given substrate. **Top row (left to right):** Cells imaged on polymers 1-4. **Second row (left to right):** Cells imaged on polymers 5-8. **Third row (left to right):** Cells imaged on polymers 9-12. **Last row (left to right):** Cells imaged on polymer 13-16. Polymer numbers refer to aforementioned-keyed system in **Table 4.1**.

Initial mean descriptors values are computed for the 16 polymer substrates. Mean values of a population reflect the heterogeneous population of cell shapes observed on individual polymer films. For each polymer condition at least 20 cells are utilized as the sample population so as to effectively capture the shape-based population distribution of cells cultured on the different polymer films. Since 16 polymer conditions were considered with approximately 60 descriptors per polymer condition, a 60X16 data matrix is recovered where each data point represents the mean value for the cell descriptor of the population of cells cultured on a given polymeric substrate. The implementation of a “heat map” illustration allows the quick statistical comparison of individual descriptor means (**Fig. 4.6**). The “heat map” representation identifies the statistical differences (P-value of an ANOVA with post-hoc LSD comparison) between descriptor values among the differing polymer compositions utilizing a color-based keying system. In **Fig. 4.6**, all descriptor values for a given polymer composition are compared statistically to the same descriptor obtained for poly(DTE carbonate). Poly(DTE carbonate) was chosen as the comparison polymer because 14 of the 16 polymers within the test set represent perturbations of the polycarbonate via modification of the backbone by addition of increased percentages of PEG, charge and/or iodination. Therefore, the utilization of poly(DTE carbonate) as the comparison polymer allows for the identification of the effect that individual additions to the polymer backbone have on cell shape and actin cytoskeletal organization.

The “heat map” possesses the ability to both identify polymer chemistries that result in gross morphological changes as well as to identify descriptors that are sensitive to individual changes in polymer chemistries. For example, the columns shown in **Fig. 4.6** represent different polymer chemistries with each row within the column indicating the P-value of an ANOVA with post-hoc LSD between the descriptor values of a population of cells cultured on the indicated polymer and poly(DTE carbonate). A column represented with a majority of descriptors in blue identifies a polymer condition where the values of numerous descriptors for cells cultured on the indicated polymer differ from those cultured on poly(DTE carbonate). The observation that a majority of the descriptors appear statistically different likely highlights this polymer chemistry as one that promotes gross changes in cell shape and possibly strong differences in cell response.

Analysis of the heat-map representation allows for a number of interesting conclusions (**Fig. 4.6**). Like the proliferative and mineralization responses, the heat map demonstrates that the largest statistical differences in global cell shape and cytoskeletal organization occur with the addition of PEG. This is evident within the heat map as columns 1-3 and 7-8 demonstrate near step wise changes in cell shape comparable with some of the Saos-2 cell behaviors observed in response to culture on the same polymers. Interestingly, the addition of iodine to the polymer backbone reduced the effect that PEG had on cell shape, again reflecting the behavioral response of cells to these materials. Therefore, because the cell shape seems in some respects to mirror Saos-2

response, it follows that cell shape parameters may accurately capture or encode complex cell behaviors on biomaterials. One advantage of the high-content approach remains the fact that while global cell shape follows many of the physiologic cellular behavior trends, individual descriptors may be identified that are responsive to individual chemical components of the materials. Through examination of the rows throughout the “heat map” it is possible to identify descriptors that respond to individual alterations of the polymer chemistry or changes that result from multiple alterations to the polymer backbone. The morphometric descriptors may therefore function as sensitive indicators of polymer chemistry. However, to parse this data requires computational methods that have the ability to dissect the heat-map data into the most influential reporters of Saos-2 response.

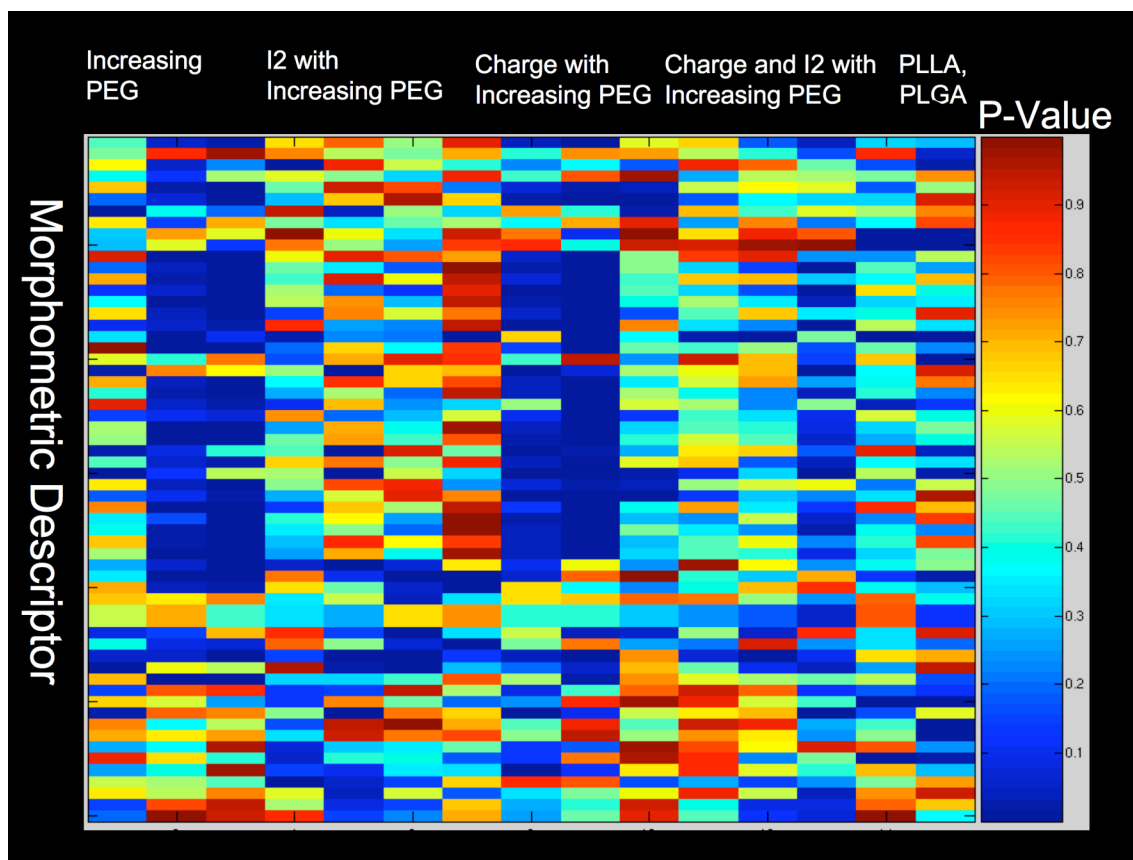


Figure 4.6: “Heat-map” representation of the statistical difference of in morphological descriptor value as a result of culture on polymers of different chemistry.

The heat-map displays the P-value of an analysis of variance (ANOVA) with post-hoc LSD test when comparing the individual morphometric descriptors (rows) on poly(DTE carbonate) to the polymers indicated in the columns.

4.3.4 Decision Tree Modeling to Parse Chemistry Responsive Morphometric Descriptors

CART based DTs allowed more accurate determination of descriptors that are sensitive to distinct changes of polymer chemistry. The chemical alterations considered in this study included the additions of iodine, PEG and charge. DTs analysis determines the morphometric descriptors that are most responsive to the aforementioned chemistry alterations. The DTs results can be seen in **Fig. 4.7**. In **Fig. 4.7** three separate trees were derived for the presence of charge, iodine and PEG in the polymer substrate. The descriptors that best correlate with changes in polymer chemistry are present in the higher nodes within the trees. Thus, eGFP-actin defined clumpiness is most responsive to pegylation. Hole area and the standard deviation of actin filament staining intensity are most responsive to charge. Curl (convex) is the most responsive to the presence of iodine, followed by the ratio of the length to the width of the box bounding the cell (Box X/Y) and then cell roundness.

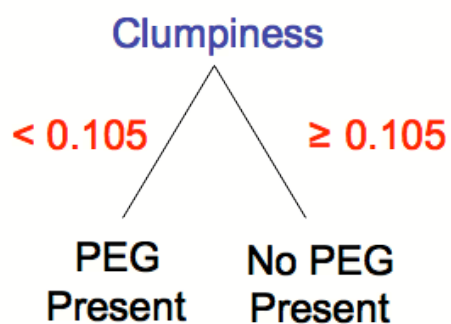
4.3.5 Computational Modeling Efforts to Predict 3 Week Polymer-Mediated Mineralization Based on 24 hour High Content Morphometrics

Computational modeling efforts are employed to determine if the high-content imaging approach may provide new insights into the complex behavioral responses exhibited by Saos-2 cells on the polycarbonates. To test the validity of the premise, mineralization was chosen as a target behavior for high content screening. Mineralization was chosen over proliferation because mineralization

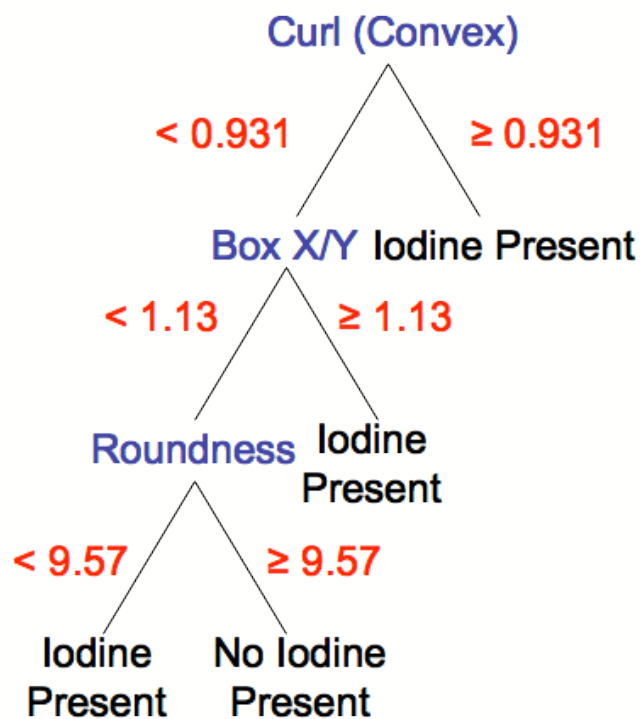
is a process that takes weeks of assay time in order to assess. Therefore, a high-content approach that can quickly predict mineralization response weeks ahead of time would represent a significant advancement to the characterization of biomaterials for possible orthopedic applications.

Following the approach outlined by Smith et al. (144), a DTs model allows for feature selection. To take into account the uncertainty of cellular response measurements, the conventional CART routine is augmented by a Monte Carlo (MC) procedure. A series of computer-based pseudo-experiments are generated where the measured values of mineralization and the mean descriptor values on the different polymer films are randomly perturbed within a normal distribution defined by the experimental mean and standard deviation. A single most relevant descriptor (i.e., the descriptor with the highest information gain) is obtained from each pseudo-experiment, representing the first node of the decision tree for that pseudo-experiment. Descriptor results from all MC iterations are summarized into a histogram and the top descriptors with the highest counts in this histogram undergo further analysis. To determine the relevance of the descriptors to cellular functions, a descriptor based on a randomly generated series of numbers is added to the data set (a 61st descriptor). The relative relevance (RR) (**Table 4.2**) of each descriptor was calculated as the ratio between the count of the descriptor of interest and the count of the randomly generated descriptor entitled “Random”. The three descriptors that were found to have the highest RR in 100,000 MC iterations were: “Aspect ratio” (RR = 463), “heterogeneity” (RR = 174), and “margination” (RR = 135) (**Table 4.2**). These three descriptors are

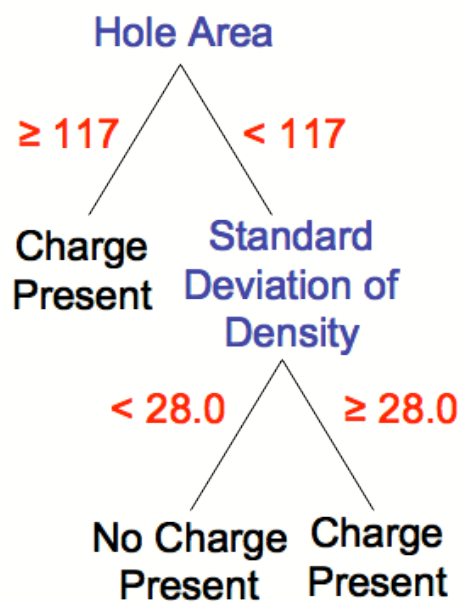
then used to generate and test an ANN model to predict Saos-2 mineralization studies. Utilizing a 10-fold cross validation analysis, a model was built using just Saos-2 heterogeneity, aspect ratio and margination to predict 3 week mineralization responses on the 16 polymer set. The ANN results can be seen in **Table 4.3**. Unfortunately, the ANN performs moderately at predicting 3 week mineralization on biomaterial substrates based solely on early actin-based cell morphology. The ten-fold cross validation yielded a correlation coefficient of 0.5713 for the 16 instances.



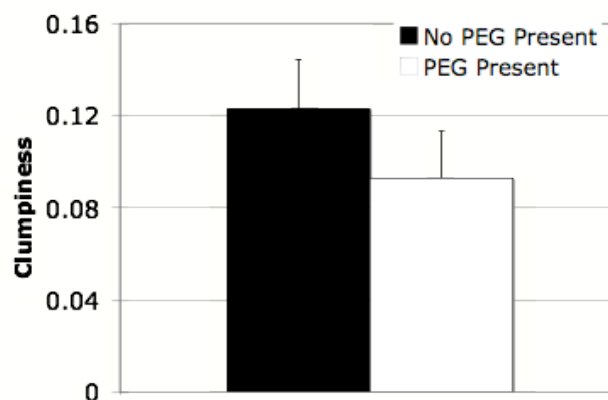
(a)



(b)



(c)



(d)

Figure 4.7: Polymer chemistry responsive descriptors determined by decision tree analysis.

The decision trees here identify descriptors most responsive to individual alterations of substrate chemistry. The tree decision process is read as follows: the decision nodes (in blue) represent descriptors with a decision rule (in red) based on the descriptor value. The tree identifies the presence or lack of a certain polymer chemistry based on a sequential binary process of path selection following the decision rules. Tree (a), (b), and (c) represent trees for PEG, iodine, and charge respectively. (d) represents the average value of clumpiness for polymer with and without PEG (difference significant at $p < 0.05$ by Student's T-Test).

Table 4.2: Decision tree results of top 3 Saos-2 24 hour morphometric descriptors relating to 3 week mineralization.

Descriptor	Relative Relevance
Aspect Ratio	463
Heterogeneity	174
Margination	135

Table 4.3: Summary of 10-fold cross validation artificial neural network used to predict Saos-2 3 week mineralization on polymers based on solely 24-hour actin morphometrics.

Summary Statistic	Value
Correlation Coefficient	0.5713
Mean Absolute Error	0.0908
Root Mean Squared Error	0.1143
Total Number of Instances	16

4.4 Discussion

Saos-2 cells represent an osteosarcoma cell line that demonstrate utility as a model for human osteoblasts (284). Current research has utilized these cells to model osteoblastic response to a number of biomaterials including: titanium (285), biomimetic substrates such as hydroxyapatite (285-287), and synthetic biomaterials (288-290). Within the current study, they are used as a model to determine if complex cell-material interactions may be encoded within the early actin-based cytoskeletal organization.

Saos-2 cells were engineered with an eGFP-actin vector to allow the identification of the cytoskeleton within living cells cultured on synthetic, degradable, combinatorially synthesized tyrosine-derived polycarbonates. This library was selected because it possesses enormous tunability of the material's physical and biological properties. With regards to human osteoblast-like cells, Webb et al. demonstrated that osteoblasts respond to changes in surface chemistry, with changes in chemical functional groups having larger consequences on cell behavior than substrate wettability (291). Thus, copolymerization with other monomers represents another method to access novel polymers that may have significant effects on cellular phenotypes.

Saos-2 proliferative and mineralization responses are often utilized as an initial assessment of cell-biomaterial response (292, 293). When cultured on the library of 14 polycarbonates and 2 poly(α -hydroxy ester)s, diverse and complex proliferative and mineralization behaviors are observed. Perhaps the most

consistent response is the decrease in both mineralization and proliferation with the inclusion of PEG. Copolymerization with PEG provides a method to tune both physical and biological properties of the polymers (213). PEG copolymerization allows for the creation of degradable, biocompatible polycarbonates with increased hydrophilicity, decreased glass transition temperatures, decreased tensile moduli, decreased cell attachment and increased water uptake (213, 270). The observed decrease in both the proliferation and mineralization of Saos-2 cells on the pegylated polymers may result from the anti-adhesive attributes of the PEG. Previous studies by Okumura et al. demonstrate that the ability of Saos-2 cells to proliferate and produce mineral depends highly on the rate and degree of surface attachment (285). Therefore, the observed decrease in proliferation and mineralization may simply have resulted from the “cell repellent” nature imparted via addition of PEG to the polymer backbone. Additionally, PEG inclusion may affect cellular response via differential ligand conditioning. PEG-variant biomaterials systematically regulate cell behaviors such as cell motility, cell adhesion, cell attachment strength, and thrombogenic activity via alterations in the conformation and total amounts of adhered proteins such as fibronectin (219, 220). Previous reports indicate that small changes in polymer chemistry that alter fibronectin and type I collagen conformation and spatial distribution result in altered osteoblast-specific gene expression in Saos-2 cells (294, 295). Thus, the effect of PEG may result from anti-cell adhesive nature or due to induced conformational changes in adsorbed proteins.

The copolymerization with iodinated monomers imparts radiopacity enabling the polymeric device to be visualized on X-ray fluoroscopy (269, 296). While X-ray visibility is the primary impetus for the addition of halogenated monomers to the tyrosine-derived polycarbonate backbone, the chemical change results in alterations to the physical and biological properties of the materials. Polymers containing iodine have differential effects on protein absorption profiles and cellular behaviors based on both individual polymer chemistry and cell type (211, 214, 235). In this study, iodine mitigates the effect of PEG on Saos-2 proliferation. Recent studies indicate that iodine can rescue the effects of pegylation on human smooth muscle and endothelial cell adhesion, growth and migration via counteraction of the non-fouling properties imparted by PEG (211, 297). Therefore, the rescue of Saos-2 cell proliferation likely stems from similar reversal of the protein repellence (235). The decreased mineralization detected simply in the presence of the iodinated polymer represents an interesting new finding. Previous reports indicate that osteoblastic like cells preferentially pattern on material chemistries that presumably promote greater proteoglycan adsorption (298). Therefore, the decreased mineralization may result from extreme fouling of the surface allowing for serum proteins to displace proteoglycans from the surface. However, this hypothesis should be assessed in future studies.

DT generally exerts its change on polycarbonate behavior via increases in the rates of polymer degradation (210). Interestingly, studies also demonstrate that the presence of the acid pendent group results in enhanced hydrophilicity

and adsorption of calcium ions suggesting usefulness of the material in mineral forming cells (217, 218). This study reports that incorporation of DT monomers results in suppression of both Saos-2 proliferation and mineralization. Interestingly, previous work using gels indicated that anionic charge actually increased Saos-2 attachment and proliferation (299). While thin films and gels are not directly comparable, the effect of imparting charge on polymer surfaces remains a phenomena requiring greater investigation. Perhaps the most interesting observation of this study is the opposite and synergistic behavior displayed when DT is combined with PEG. This effect was captured in both the proliferation and mineralization responses of Saos-2 cells. This effect may be due to some balance in pro-oxidant and anti-oxidant produced by the PEG and DT segments respectively that promotes optimal growth conditions for Saos-2 cells (300).

The presented studies demonstrate that via the use of combinations of iodinated monomers, charged monomers, and PEG it is feasible to elicit ranges of cellular behaviors in osteoblast-like cells. The combinatorial nature of the library adds an additional layer of complexity that may confound effects seen within single chemical alterations. Therefore, in an effort to capture the intricacies of these biomaterial-dependent behaviors, a high content profiling approach is employed. High-content imaging of eGFP-engineered Saos-2 cells has been reported for limited members of the polycarbonate library (268). However, this study aimed to drastically increase the number and combinatorial nature of the assayed materials. The heat map representation provides a global

view of which chemistries most affect actin organization. Interestingly, when analyzing the heat-map it is evident that the conditions that promote the greatest changes in cell shape are the PEG containing conditions. This corresponds well with the proliferation and mineralization studies that highlighted the PEG containing polymers as those that most alter Saos-2 response.

DTs modeling provides greater insights into the cell shape and cytoskeletal organizational changes elicited by different polymer chemistries (**Fig. 4.7**). Interestingly, all three of the trees highlight different groupings of descriptors that respond to different changes in the backbone chemistry. Whereas the DTs for iodine contains descriptors that are largely representative of changes in whole cell shape, the DTs for PEG and charge are representative of changes in actin filament distribution. This would seem to indicate whereas iodine affects cellular behavior by influences largely related to whole cell shape, PEG and charge act via differences in actin filament spatial configurations and distributions. With regards to the presence of PEG containing polymers, it can be seen in **Fig. 4.7** that the average clumpiness for cells cultured on polymers containing PEG is lower than the value for those cultured on polymers without PEG. Clumpiness is defined as the fraction of pixels deviating more than 10% from the average intensity of the object remaining after an erosion process. It reflects the object's texture. With regards to the eGFP-actin engineered Saos-2 cells employed in this study, clumpiness most likely correlates with the degree to which actin monomers within the cells have been organized into filamentous structures. This is because monomeric actin, which is represented as small area

pixels, would not remain after an erosion procedure. Therefore, the greater the percentage of pixels remaining after erosion the more likely the actin monomer is arranged in a spatially localized structure. The presence of PEG most likely results in less organization of actin into grouped structures such as filaments. Utilizing high-content based morphological screening it is possible to identify cell populations cultured on substrates of different chemistries, and with DTs modeling the descriptors that best respond to these perturbations are highlighted.

While the ability to parse out cytoskeletal changes that evolve from culture on differing substrates, ultimately the usefulness of the high content imaging approach rests in its ability to predict cell behavioral responses. In this study, high-content imaging was utilized in an attempt to predict Saos-2 substrate-mediated mineralization. As discussed previously, Saos-2 cells are generally utilized as a model cell line for osteoblastic cells. The main function of the osteoblast is the production of mineralized bone (301). Osteoblasts and Saos-2 osteoblastic cells have been shown to have material-dependent mineralization responses (302-305). However, traditional screening has relied on material synthesis, a 2-4 week cell culture period, and then mineralization assays to elucidate these responses. In this study, live high-content images of eGFP-actin engineered individual cells is attempted as a novel methodology to predict or capture mineralization responses weeks before then can be experimentally recorded. Utilizing a feature selection and modeling paradigm previously published by Smith et al. (144), three descriptors out of 60 were selected for a Monte Carlo series of pseudo-experiments via DTs modeling. The selected

descriptors represented the top descriptor of the DTs of 100,000 pseudo-experiments with high RR (**Table 4.2**). The high RR of these descriptors indicates that when accounting for the experimental variability in both the functional mineralization assays and the high-content descriptor evaluation these descriptors are 463 to 174 times more important than a randomly generated series of numbers within a normal distribution. Interestingly, the selected descriptors represent a combination of both general shape behaviors (aspect ratio), and cytoskeletal organizational descriptors. Studies by Anselme et al. identify that human osteoblast adhesion, mineralization and cytoskeletal assembly are correlated with elongated osteoblasts (154). Therefore, that aspect ratio was the most relevant descriptor in our DTs analyses is not surprising. Margination and heterogeneity both represent descriptors that pertain to the actin cytoskeletal organization throughout the cells. Cells with higher levels of both margination and heterogeneity would represent cells with high degrees of monomeric actin organized into filamentous structures located toward the periphery of the cell. The importance of the actin cytoskeleton and its arrangement into filamentous structures has been documented thoroughly within the literature. Disruption of the actin cytoskeleton in human mesenchymal stem cells treated with osteogenic induction factors is sufficient to reduce or even completely inhibit osteoblastogenesis (87, 306). Conversely, with regards to Saos-2 cells, Okumura et al. found that materials that promoted earlier osteogenesis were those that demonstrate poorly formed stress fibers and weak cell polarity (285). Therefore, although the direct relationship regarding actin

filament organization and mineralization is poorly understood, it is clear that the orientation and filamentous structure of actin plays a role therefore justifying the DTs selected descriptors.

ANN modeling of 3 week Saos-2 mineralization in response to substrates for 16 polymers was performed utilizing average high-content descriptor values obtained at 24 hours on the same polymers. A 10-fold cross validation experiment utilized 90% of the data to train and 10% of the data to test 10 separate times. Building the ANN model and validating in this manner produced a correlation coefficient of 0.5713. While this does not represent an extremely high correlation, it does indicate a medium level positive correlation of our descriptors taken at 24 hours with the long-term mineralization behaviors. The correlation may be less than optimal for a number of factors. First and perhaps most importantly, the selection of the Saos-2 as the model cell line is less than ideal. Reports indicate that care must be undertaken when utilizing Saos-2 cells as model cell lines as their proliferation rates, mineralization responses and gene expression profiles undergo phenotypic instability with increasing passage number (307). Therefore, although surface chemistry may regulate osteoblast behavior via cytoskeletal-mediated signal transduction pathways (308), Saos-2 cell mutation may unravel the intricate network linking these behaviors (309). Additionally, mineralization may represent a less than optimal choice for the cellular behavior of interest. While the extreme length of time required for mineralization assays make them a prime candidate for 24-hour morphometric screening, mineralization as a process is not 100% dependent on cells. Certain

biomaterials, particularly poly(DTE carbonate) in this study, have been shown to bind calcium phosphate crystals on the surface in the absence of cells (310). Therefore, the role of the physical material in the process of mineralization represents a likely confounder in the high-content morphometric-based predictions by the ANN.

4.5 Conclusion

This study examined how Saos-2 cells interact with combinatorially derived polymer libraries. Proliferation and mineralization data indicated that the cellular response elicited by these materials represented a complex interplay of the individual components of the polymer backbone. This interplay promoted cellular behaviors that cannot be characterized by simple compositional correlates. In an effort to parse these intricate phenotypic responses, a high-content morphometric approach that utilized eGFP engineered Saos-2 cells to obtain quantitative descriptors of actin cytoskeletal morphology was employed. Utilizing this platform, subtle variations in cellular response to the underlying substrate were highlighted using a “heat-map” visualization approach. Decision tree modeling allowed for the identification of individual morphometric descriptors that were sensitive to the addition of PEG, charge and iodine to the polymer backbone. Finally, utilizing the 24 hour morphometrics, a computational model was built to predict 3 week mineralization response at 24 hours. The model demonstrated a medium strength positive correlation. Given the general variability of biological data, the high-content morphometrics combined with aforementioned computational modeling approach possibly represents a powerful tool to parse cellular responses at early time intervals. Future studies should focus on expanding this approach to model cell lines that have less passage variability and better-defined phenotypic outputs. Additionally, an interesting pursuit remains a biochemical understanding of how these quantitative descriptors encode long-term behaviors at early time points.

5 Cytoskeleton-based Forecasting of Stem Cell Lineage Fates

5.1 Introduction:

Stem cells are pluripotent cells that display self-renewal in their stem-like states. These stem cell may be extracted from human embryonic tissues (54) , obtained from reprogrammed somatic cells (311-313) or isolated from niches within adult tissues such as but not limited to the bone marrow (55-57), liver (58, 59), skin (60, 61), adipose tissue (62, 63) and brain (64-66). Human mesenchymal stem cells (hMSCs) isolated from adult bone marrow have gained interest in the tissue engineering community because of their capability to differentiate into a multitude of terminal cell types (68). Currently, strategies in tissue engineering focus on the application of soluble cues and material substrata to direct the differentiation of stem cells toward desired cell fates (314). It has been shown that material chemistry (315), material mechanics (89), and/or applied growth factor mixtures (68, 316, 317) differentially promote MSC differentiation toward lineages such as: adipocytes, neurons, chondrocytes, myocytes and osteoblasts. Ultimately, the success of engineered constructs depends on the ability to isolate these stem cells and subsequently utilize the aforementioned tools to steer differentiation toward cell types of interest.

At present, the guided differentiation of stem cells remains difficult because the mechanisms that govern the passage from uncommitted stem cells toward differentiated cells have yet to be completely identified (318). Hindering this identification further is the reliance on traditional endpoint assays to assess lineage, which often require weeks to months of culture and provide limited early

assessment of cell behavior. Methods such as gene microarrays allow for the classification of stem cell maturation into distinct stages (319), however such methods treat heterogeneous groupings as single populations and are unable to follow the kinetics of the mechanisms underlying lineage commitment. These issues slow the pace of screening and discovery of promising new material and soluble factor treatments for stem cell tissue regeneration.

One proposed approach has centered on the analysis of whole cell morphology and cytoskeletal organization for characterizing cell responses in tissue engineering constructs. As early as 1980, Olson et al. demonstrated that mammalian cells may be classified solely based on quantitative shape characteristics and pattern recognition analyses (320). However, while cell shape and cytoskeletal organization remain traditional aspects of cell characterization in the tissue engineering and stem cell fields, the generally employed methods lack reproducible, quantifiable results and have steered from a quantitative approach to the domain of qualitative or semi-quantitative observations (134, 154-159). Recent work by Mangoubi and coworkers demonstrated that utilizing a quantitative, high-content textural analysis approach allows the identification and subsequent classification of undifferentiated and differentiated colonies of human embryonic stem cells (321). Additionally, a strictly quantitative morphometry-based approach was shown to provide “cellular fingerprints” of cell responses to substrata and soluble cues (268). Therefore, quantitative morphometry may represent a viable avenue to characterize hMSC response to soluble and material cues.

During the process of lineage commitment, cells undergo a number of morphological changes relating to differences in the spatial distribution and expression of key cytoskeletal proteins (322, 323). While differentiation is often accompanied by changes in cell shape, studies have demonstrated that cell shape in turn regulates cellular differentiation (115, 186, 188, 324). Cytoskeletal components, particularly actin and its downstream effectors, are strong mediators of hMSC differentiation toward the osteoblastic lineage, with early cytoskeletal organization having a large effect on longer-term functions (87, 306). This study presents a “high-content” imaging-based methodology where quantitative features of actin fluororeporter shapes, intensities, textures and spatial distributions (morphometric descriptors) are defined and utilized to assess cell behavior. Of central interest to the present study was the question whether the spatial and structural organization of the cytoskeleton in general, and actin in particular, encodes the predilection of cultured stem cells to differentiate toward particular cell fates. If so, “high content” morphology-based analyses of stem cell lineage commitment could provide: predictive measures of long-term cell behaviors at early time points for the effective screening of biomaterials; real time measures of stem cell fates and identification of when lineage commitment is determined; cell-by-cell based analysis that is able to capture the heterogeneity of sample populations; and the ability to parse out lineage commitment in stem cells influenced by multiple stimuli.

5.2 Materials and Methods:

5.2.1 Human Mesenchymal Stem Cell Culture

Human mesenchymal stem cells (hMSCs) were obtained from commercial sources (Lonza; Walkersville, MD). Cells were cultured in a humidity-controlled environment under 5% CO₂ and 37°C and fed every 3-4 days with growth media (basal media) supplemented with commercial SingleQuot's® (Catalog # PT-3001, Lonza). Cells were received at passage 1 and used for up to 4 passages. Cells were subcultured upon reaching 90% confluence. Osteogenic induction (OS), adipogenic induction/maintenance (AD) media were reconstituted as per manufacturer (Catalog #'s PT-3002 and PT-3004 respectively, Lonza). Adipogenic media were cycled with 3 days induction followed by 1 day maintenance. Mixed media (MX) conditions consisted of 50:50 osteogenic:adipogenic induction/maintenance media.

5.2.2 hMSC Differentiation on Fibronectin-Coated Glass Substrates

Fibronectin- (BD Biosciences; Franklin Lakes, NJ) coated glass substrates were created via the application of 400 µL of 25 µg/mL phosphate buffered saline (PBS) solution to each well of a glass bottom 24-well plate for 1 hour at room temperature. hMSCs (Lot# 7F3458 (36 year old male) and Lot# 7F3675 (22 year old female) were applied at 3,000 cells per cm² and allowed to attach in basal medium for 6 hours. After the 6-hour attachment period, the basal medium was replaced with appropriate induction media. For differentiation assays, cells were cultured for 2 weeks and then stained for alkaline phosphatase activity and lipid

production as described previously (71, 87). To stain alkaline phosphatase, cells were fixed with 4% paraformaldehyde in PBS, permeabilized with 0.1% Triton-X 100 in PBS, rinsed with PBS and stained with Fast Blue RR/napthol (Kit # 85, Sigma-Aldrich; St. Louis, MO). To stain lipids, cells were washed with 60% isopropanol and then stained with 30 mg/mL Oil Red O (Sigma). For total cell counts, cell nuclei were stained with 1 μ g/mL DAPI (Sigma).

5.2.3 Polymerase Chain Reaction (PCR) of hMSCs Under Induction Media

For 6, and 24 hour time points, hMSCs (Lot#'s 7F3458 and 7F3675) were cultured on fibronectin-coated glass and treated with induction media as described previously. For 3 week differentiation at optimal seeding densities, cells were seeded at 3,000 or 25,000 cells per cm^2 and treated with the appropriate induction media for osteogenic and adipogenic differentiation respectively. At appropriate time points, total mRNA was extracted (Catalog # 74106, Qiagen; Valenica CA) and reverse transcribed to produce a cDNA library (Catalog # 4374966, Applied Biosystems; Foster City, CA). Human primers for RUNX2 (PPH01897B), osterix (OSX) (PPH00705A), and PPAR γ (PPH02291F) were purchased from SABiosciences (Frederick, MD). All genes were compared to expression of ribosomal protein 18S (PPH05666E). Any samples that failed to show crossing points below 45 cycles were assumed to have a crossing point of 46 cycles.

5.2.4 High-Content Imaging of hMSC on Glass and Fibronectin-Coated Glass

hMSCs (Lot#: 7F3458 (Donor 1) and 7F3675 (Donor 2), Lonza, Inc., MD) were applied at 3,000 cells per cm² for 24 hour morphology and 1,000 cells per cm² for time course studies and allowed to adhere to treated and untreated glass surfaces for 6 hours in basal medium. After a 6-h attachment period, basal medium was replaced with appropriate induction media. After 18-90 (as indicated) additional hours cultured in differentiating media, cells were fixed and stained with AlexFluor 488 Phalloidin (Invitrogen). Cells were imaged under 63X objective (NA = 1.3) with a Leica TCS SP2 system (Leica Microsystems Inc.; Exton, PA) and excited at 488 nm with a 500-700 nm detection band-pass filter. All images represent a mosaic of 60 individual images (10X6 grid). Raw images of subconfluent cells were exported to Image Pro Plus Version 5.1 (Media Cybernetics; MD) and equalized for image intensity histograms, segmented to ensure that contiguous whole single cell regions of interest (ROI's) were selected, and processed to yield shape, intensity and higher order moment parameters as output to a text file.

5.2.5 Computational Methods to Parse Cytoskeleton-Encoded Stem Cell Fates

Forty-three associated morphometric features were archived for each cell. These features represent quantifiable measures of the whole cell and actin filament morphology/organization for a single cell. Features that were defined

include: shape features, intensity-based features that relate to the degree of actin filament formation, and textural and cytoskeletal organizational features that describe the spatial distribution of actin filaments and their location within a given cell. A complete list of the 43 calculated features and their relevance to the actin cytoskeleton is shown in **Table 5.1**. Due to the large (43) numbers of descriptors for each cell, dimensionality reductions such as Multi-Dimensional Scaling (MDS) or Principal Components Analysis (PCA) are necessary to reduce the number of dimensions within the data. This study chose MDS for dimensionality reduction over PCA because it does not make the assumption that each data point is a linear combination of the basis set. Instead, MDS seeks to preserve the distance between the data points in an attempt to find a non-linear mapping for the data. Nonlinear scaling methods yield better mapping in lower dimensions than standard linear transformations such as PCA (325). MDS is normally formulated as an optimization problem such that the stress is minimized. The stress function, S is defined as the disagreement in the distances calculated from the original data and the distance calculated from the lower dimensional embedding. In **Eqn. (1)**, S represents the stress, n is the number of samples within the data, δ represents the original distance, and d represents the calculated distance via multi-dimensional scaling.

$$S = \left[\frac{\sum_{i=1}^n \sum_{j>i}^n (\delta_{ij} - d_{ij})^2}{\sum_{i=1}^n \sum_{j>i}^n d_{ij}^2} \right]^{1/2} \quad (1)$$

$$d_{ij} = \left[\sum_{a=1}^m (x_{ia} - x_{ja})^2 \right]^{1/2} \quad (2)$$

d is calculated via **Eqn. (2)**, where x is the coordinate of the point within the new embedding and a is the number of dimensions desired, which in this study is 3. These two equations are coupled in an optimization framework and solved via techniques such as steepest descent or other nonlinear optimization methods (326). Ultimately, the MDS algorithm reduces the dimensionality of the data set by the discovery of similar and dissimilar groupings of the 43 actin-defined features of each cell. These groupings are defined via a non-linear combination of the descriptors that maximizes the observed similarities and dissimilarities between cells. The individual cells are then plot in 3D with the inter-point distance representative of their descriptor-combination similarities; points nearer to each other in the 3D remapping are more similar that points further from each other (**Fig. 5.1**). Multi-Dimensional Scaling (MDS) was implemented via Matlab's (Mathworks; Natick, MA) statistical toolbox to re-graph cellular descriptor coordinates based on a reduced 3D representation where each point represents an individual cell. To ensure that reduced data sets were valid, a synthetic data set was generated based on the variance of each of the individual classifiers (**Fig. 5.2**) and compared to MDS results for sample conditions. Classification of MDS-based cell coordinates was performed utilizing a support vector machine (327). Classification accuracy, sensitivity and specificity were performed with a randomized two-fold cross validation run 50 times on individual data sets utilizing a radial distribution function.

5.2.6 Preparation of Spin-coated Polymeric Substrates

Tyrosine-derived polycarbonates (270), polymethacrylates (146, 328), poly(D,L-lactide-co-glycolide) (Resomer 506) and poly(L-lactic acid) (Resomer L-206) (Boehringer Ingelheim; Ridgefield, CT) were dissolved in a 1.5% (v/v) methanol in methylene chloride solution yielding a 1% (w/v) polymer solution. Polymer solutions were then spin-coated onto a 15 mm glass coverslip. Spin-coating was conducted at 4,000 RPM for 30 seconds. Collagen coated coverslips were made by incubating a glass coverslip in a 7 $\mu\text{g/mL}$ collagen solution at 37°C overnight.

5.2.7 hMSC Morphometrics and Differentiation on Polymeric Substrates

Polymer-coated glass coverslips were placed in the bottom of a 24 well glass bottom tissue culture plate and secured with a silicon O-ring (Catalog # -111, Molding Solution; Lexington, KY). The setup was sterilized with a UV light applied at 5,500 to 6,500 μW per cm^2 for 900 seconds. hMSCs (Lot#'s 6F4392 (18 year old male) and 7F3458) were applied at 21,000 cells per cm^2 and allowed to attach in basal medium for 6 hours. After the 6-hour attachment period, the basal medium was replaced with appropriate induction media. After 24 h, cells were fixed, stained with phalloidin and imaged as described above. For differentiation assays, cells were stained for alkaline phosphatase activity and lipid production as described previously. Only substrates that elicited greater than 50% of the cells with alkaline phosphatase activity at 2 weeks were examined within this study.

Table 5.1: Table of 43 actin fluororeporter-defined morphometric features for individual hMSCs.

This table lists the 43 actin-based features quantified for each cell. The definition of the feature and its probable significance to actin filament organization are listed. Shape features are highlighted in blue, intensity features are highlighted in green, and textural/organizational features are highlighted in red.

<i>Feature</i>	<i>Definition</i>
Angle	Reports the angle between the vertical axis and the major axis of the equivalent ellipse. Within the context of this study it would capture randomly oriented versus aligned cell populations,
Area	Reports the total actin area of each cell.
Polygonal Area	Reports the area of the polygon that defines the object's outline.
Area/Box	Reports the ratio between the area of each object and the area of the imaginary bounding box.
Aspect	Reports the ratio between the major and minor axes of the ellipse with the same area, first and second order moments of the cell.
Axis (major)	Reports the length of the major axis of the ellipse with the same area, first and second order moments of the cell.
Axis (minor)	Reports the length of the minor axis of the ellipse with the same area, first and second order moments of the cell.
Box Height	Reports the height of the smallest bounding box that completely encompasses the whole cell.
Box Width	Reports the width of the smallest bounding box that completely encompasses the whole cell.
Box Ratio	Reports the ratio between the Box Width and Box Height
Dendrites	Reports the number of 1-pixel thick open branches. Within the context of the actin cytoskeleton it represents the number of processes stemming from the cell.
Dendritic Length	Reports the total length of all dendrites.
Maximum Diameter	Reports the length of the longest line joining two outline points and passing through the centroid of the cell.
Mean Diameter	Reports the average length of the diameters.
Minimum Diameter	Reports the length of the shortest line joining two outline points and passing through the centroid of the cell.
End Points	Reports the number of 1-pixel thick processes stemming from the cell.
Maximum Feret Length	Reports the longest caliper length.
Mean Feret Length	Reports the average caliper length.
Minimum Feret Length	Reports the shortest caliper length.
Fractal Dimension	Reports the fractal dimension of the cell's outline.

Cell Area/Total Area	Reports the ratio between the area of the cell to that of the entire field of view (10x6 tile scan image).
Perimeter	Reports the length of the outline of each cell using a polygonal outline.
Perimeter2	Faster but less accurate measure of the perimeter.
Perimeter3	Reports a corrected chain code length of the cell perimeter.
Convex Perimeter	Reports the perimeter of the convex outline of each cell.
Elliptical Perimeter	Reports the perimeter of the ellipse surrounding the outline of each cell.
Perimeter Ratio	Reports the ratio of the convex perimeter to the perimeter outline of each cell
Maximum Radius	Reports the maximum distance between each cell's centroid pixel position and its perimeter.
Minimum Radius	Reports the minimum distance between each cell's centroid pixel position and its perimeter.
Radius Ratio	Reports the ratio between Max Radius and Min Radius for each object, as determined by Max Radius / Min Radius.
Roundness	Reports the roundness of each object, as determined by the following formula: $(\text{perimeter}^2) / (4 * \pi * \text{area})$. Circular cells will have a roundness = 1; other shapes will have a roundness > 1.
Size (Length)	Reports the feret diameter (caliper length) along the major axis of the cell.
Size (Width)	Reports the feret diameter (caliper length) along the minor axis of the cell.
Mean Density	Reports the mean intensity of all pixels within a cell. Correlates to the average amount of fluorescently tagged phalloidin present within a given cell.
Standard Deviation of Density	Reports the standard deviation of the intensity of pixels within a cell. This represents the degree to which the phalloidin stained cytoskeleton is localized into distinct filaments of equal staining intensity.
Sum of the Density	Reports the sum of the total intensity values of all pixels within a cell. Corresponds to the total amount of positive phalloidin-staining within the cell.
Integrated Optical Density	Reports the average intensity of each object normalized by the area of the cell.
Holes	Reports the number of independent contiguous areas with no staining within a cell.
Hole Area	Reports the area of holes within an object.
Hole Ratio	Reports the ratio of the object area excluding holes, to the total area of the object, as determined by $\text{Area} / (\text{Area} + \text{Hole Area})$.
Margination	Reports the distribution of intensity between the center of the cell and the edge of the cell. Describes the relative spatial distribution of actin filaments within the cell.
Heterogeneity	Reports the fraction of pixels that vary more than 10% from the average intensity of the cell. Is a textural parameter that describes the degree to which the actin filaments are organized into homogeneously stained structures.
Clumpiness	The fraction of heterogeneous pixels remaining in a cell after an erosion process. It reflects the object texture and the degree to which actin filaments are organized into filamentous structures.

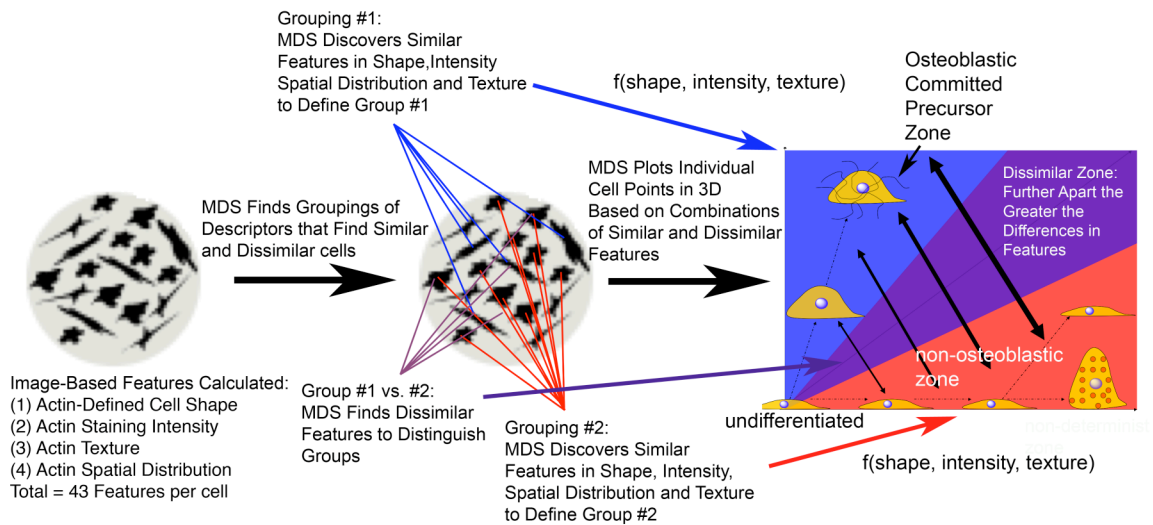


Figure 5.1: Schematic of Multi-Dimensional Scaling (MDS) approach to segment cells based on actin cytoskeletal organization.

A heterogeneous population of cells is cultured on a substrate, stained with fluorescently labeled phalloidin, which binds filamentous actin, and imaged at high-resolution. 43 morphometric features are calculated for each cell based on actin shape, intensity of staining, texture and spatial distribution. MDS allows the 43 features of individual cells to be grouped and remapped in 3D with their proximity to each other indicative of the similarities in their features. More similar cells are graphed closer together than less similar cells. The MDS algorithm discovers similar and dissimilar groupings of cells via a non-linear combination of the 43 descriptors that maximizes the spatial representation of the similarities and dissimilarities between individual cells.

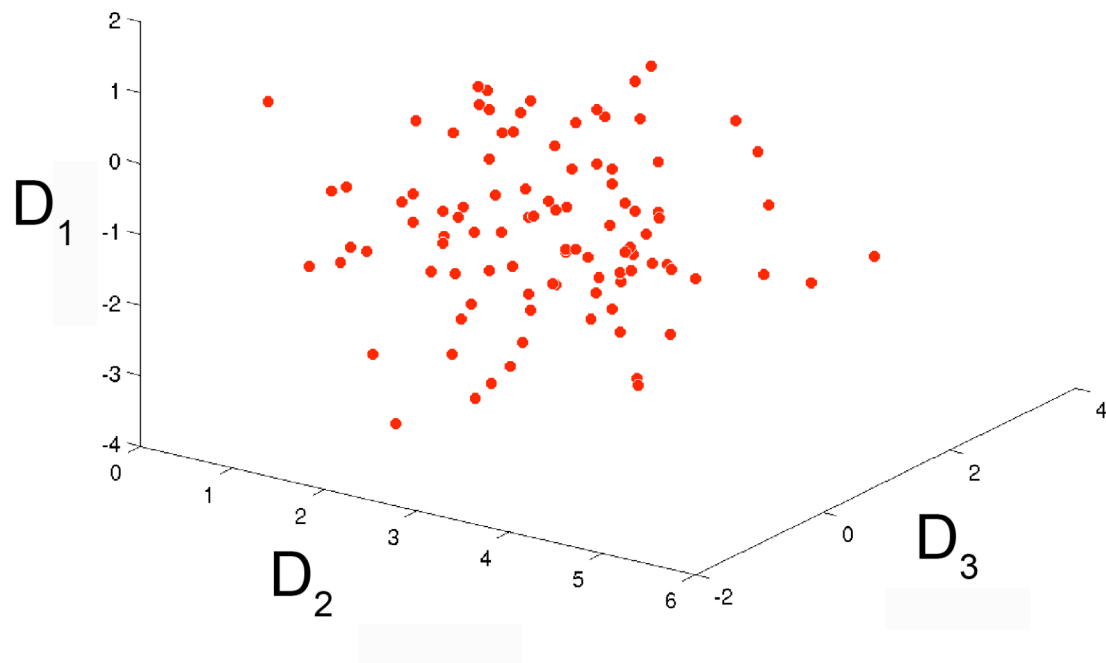


Figure 5.2: Performing MDS upon a random negative control yields no clear identifiable structure.

A negative control was run to confirm that the vertex based MDS structure seen in **Fig. 5.3-5** are not an artifact of the multidimensional scaling process itself. The synthetic negative control consisted of randomly generated values with the same mean and standard deviation as the raw data. Performing the MDS on this synthetic data set results in a graphical representation of the data lacking defined structure while maintaining its Gaussian character. There is no clear reference point or vertex from which the rest of the data deviates. Therefore the MDS clustering seen in the experimental conditions clearly results from inherent attributes of the data and is not a random effect.

5.3 Results:

5.3.1 hMSC adopt distinct differentiation outcomes that are not apparent from early cell shape/morphology

Human bone-marrow derived MSCs demonstrate differentiation behaviors that are dependent upon both cell seeding density and growth factors. Traditionally, adipogenic differentiation of hMSCs is observed when seeding cells at high density (25,000 cells per cm^2) in media supplemented with dexamethasone, indomethacin, insulin and isobutylmethylxanthine; while osteogenic differentiation of hMSC is induced by seeding cells at low density (1,000-3,000 cells per cm^2) with supplementation of dexamethasone, ascorbate and β -glycerophosphate (68). By culturing cells at 3,000 cells per cm^2 on fibronectin-treated glass, we observed distinct differentiation fates after two weeks in AD (**Fig. 5.3A**), basal (**Fig. 5.3B**), and OS induction media (**Fig. 5.3C**). At 3,000 cells per cm^2 on fibronectin-coated glass in AD media (**Fig. 5.3A**), which is well below the optimal seeding density for adipogenic differentiation, hMSCs displayed evidence of both adipocytic and osteoblastic differentiation at 2 weeks as assessed by Oil Red O and Fast Blue Staining respectively (**Fig. 5.3D**). Under the same seeding density with OS media (**Fig. 5.3D**), hMSCs exhibited osteoblastic differentiation with greater than 75% of the cells displaying alkaline phosphatase activity and no detectable evidence of lipid accumulation. Finally, under basal control media (**Fig. 5.3B**), the vast majority of cells were identifiable

neither as osteoblastic nor adipocytic cells. Thus, under these conditions, hMSCs demonstrate robust differentiation behaviors in response to altered soluble cues. Screening for early changes in the “overall” cell morphology (24 h) fails to capture these differences between conditions (**Fig. 5.3E-H**). The identification of which cells are committed toward the osteoblastic versus adipocytic lineages is impossible between conditions. In fact, comparison of traditional shape parameters such as total cell area and cell aspect ratio (**Fig. 5.3H**) reveals no apparent difference between AD- and OS-treated samples.

5.3.2 Early PCR of characteristic genes of differentiation fail to show differences in AD versus OS treated cell cultures.

While stark differences in differentiation behavior are observed in hMSCs at 2 weeks, an interesting question remains when is the earliest moment that lineage commitment may be defined for these cells. Traditionally, the earliest indicators of commitment to the osteoblastic and adipocytic lineages are shown to be changes in gene expression profiles (319, 329). Of particular importance in osteoblastic differentiation are RUNX2 (Cbfa1) (72), a transcription factor and major regulator of osteoblastogenesis, and its downstream effector OSX (81), a transcription factor necessary for progression to the osteoblastic phenotype. The expression of the transcription factor PPAR γ , being both necessary (101, 102) and sufficient (103) for adipocytic differentiation, represents an identifiable gene that is up-regulated in adipogenesis (110). To identify the relative changes in gene expression that are characteristic of terminal cell phenotypes, hMSCs were cultured for 3 weeks under seeding densities and media conditions optimized for

adipogenesis and osteoblastogenesis as described previously. PCR was performed on these samples (**Fig. 5.4**) with the gene expression for RUNX2, OSX and PPAR γ relative to 18S normalized to the expression of the same genes of undifferentiated hMSC in basal media after a 6-hour attachment period. Adipocytic differentiated hMSCs up-regulate the mRNA expression of PPAR γ over 10,000 fold compared to their osteoblastic counterparts, where expression increases only 3 fold when normalized to the undifferentiated hMSC condition. hMSCs of the osteoblastic phenotype demonstrate increases in RUNX2 and OSX transcription of 25 fold and 3.5 fold respectively. Gene expression for adipocytic cells showed only an 18 fold increase for RUNX2 and actually showed a increase in OSX expression of 6 fold over basal cells. These experiments confirm that for hMSCs differentiated to adipocytes we expect a large increase in PPAR γ as a hallmark gene expression feature of the phenotype (114). Likewise, for the osteoblastic fate, hMSCs should exhibit increased levels of mRNA expression for RUNX2 (72). To determine whether these characteristic changes in gene expression could be used to identify early populations of cells as either osteoblastic or adipocytic, PCR for RUNX2, OSX and PPAR γ was performed at 6, and 24 hour (**Fig. 5.4**). Interestingly, at 24 hours no features of the gene expression changes characteristic of the terminal phenotypes were observed. All genes of interest remained either unchanged or were slightly down regulated compared to their undifferentiated predecessors (6 hour conditions under basal media). Thus, gene expression analyses by PCR of key genes indicative of osteoblastogenesis and adipogenesis fail to identify lineage commitment events

occurring after culture under osteogenic and adipogenic induction media at seeding densities of 3,000 cells per cm² on fibronectin-coated glass.

5.3.3 High Content Cytoskeletal Imaging and Computational Modeling Yield Morphologically Distinguishable Stem Cells

Our premise is that early cytoskeletal morphology of single cells (**Fig. 5.5A**) enabled through high-content imaging may hold clues to longer-term hMSC behavior. Tile scan images of phalloidin-stained hMSCs cultured under adipogenic, osteogenic, and basal media conditions demonstrate that cells rapidly organize their actin cytoskeleton within 24 hours (**Fig. 5.3E-G**). Individual cell cytoskeletal shape, texture, and spatial distribution descriptors were obtained via a series of image processing techniques (**Fig. 5.5B**) that capture quantitative differences in cell organization that are not apparent to the eye. High-content morphometric analysis provides 43 cytoskeletal shape-, intensity-, and texture-based descriptors of whole cell and individual filament morphology for each cell (**Fig. 5.5C**). Using MDS key combinations of these 43 descriptors were reduced into 3 dimensions (**Fig. 5.5D**).

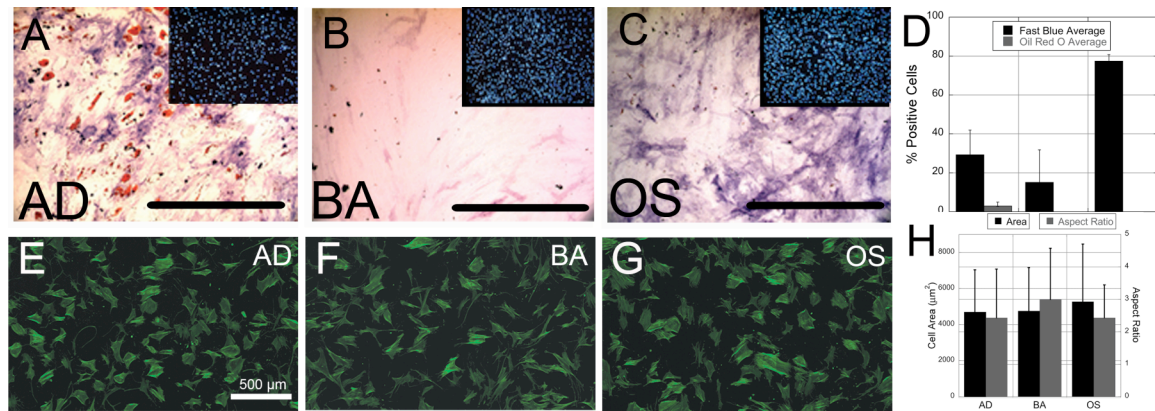


Figure 5.3: hMSCs display growth factor-dependent differentiation behaviors at 2 weeks that are not apparent at 24 hours.

hMSCs were cultured on fibronectin-coated glass substrates at 3,000 cells per cm^2 for 2 weeks in either **(A)** AD media, **(B)** BA or **(C)** OS induction media. Differentiation behaviors for osteoblastic and adipogenic phenotype were assessed by Fast Blue Staining (blue stain) for positive alkaline phosphatase activity or Oil Red O (red stain) staining for intracellular lipid accumulation respectively (collectively “FBOR”). Inlays represent corresponding images of fluorescently labeled nuclei. **(D)** Quantitative analysis of FBOR staining demonstrates 75% fast blue positive cells in OS media and significantly ($p < 0.05$) less fast blue positive cells and almost no oil red O positive cells in AD and BA media. Error bars represent the standard deviation of $N=2$ independent experiments. hMSCs were cultured for 18 hours in **(E)** AD media **(F)** BA media, and **(G)** OS media. Cells were fixed and then stained for actin at 24 hours of total culture time. **(H)** Quantitative assessment of cell shape parameters traditionally associated with cell fate (cell area and aspect ratio) demonstrated no significant differences between AD, BA and OS treated hMSCs at 24 hours. Error bars

represent the standard deviation for N=350-437 cells. Scale bar for A-C = 100 μm .

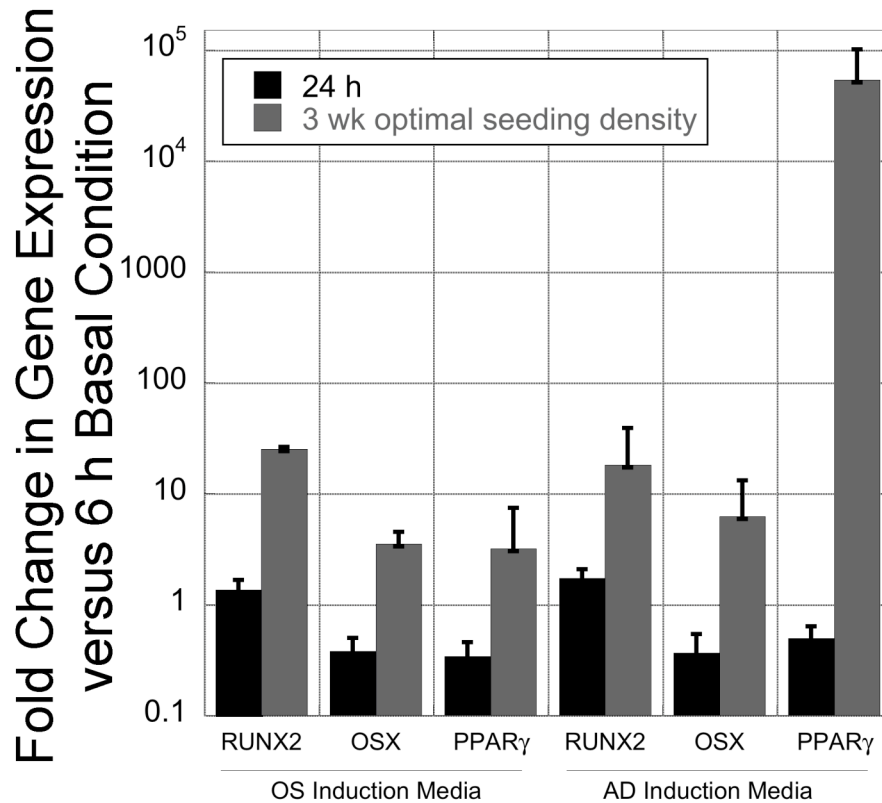


Figure 5.4: hMSCs display growth factor dependent differentiation behaviors that are not detectable by gene transcription analyses within the first 24 hours of culture.

Polymerase chain reaction (PCR) results of mRNA transcripts of RUNX2, OSX and PPAR γ for cell cultures at 24 hours, and 3 weeks in either AD or OS induction media. For the 6 and 24 h samples cell seeding densities were 3,000 cells per cm². The 3 week samples were seeded at 1,000 cells per cm² for OS conditions and 25,000 cells per cm² for AD conditions to promote optimal osteoblastogenesis and adipogenesis for comparisons. PCR data shown resulted from N = 2 independent experiments with cells from 2 different donors. Error bars represent the standard deviation.

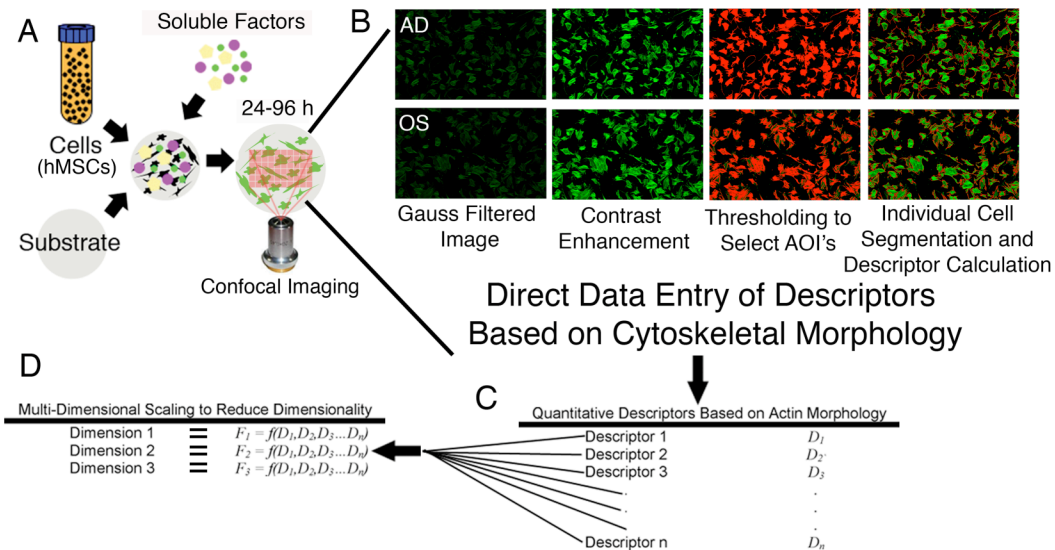


Figure 5.5: The development of descriptor-based computational modeling approaches to parse hMSCs at 24 hours in culture.

(A) A quantitative approach was undertaken to parse cell fates. Tile scan images for single experiments were obtained and underwent image processing **(B)** to yield a list of 43 morphometric descriptors that described whole cell shape and cytoskeletal distribution **(C)**. **(D)** Utilizing multi-dimensional scaling (MDS), the 43 dimensional descriptor space was combined in a non-linear fashion to create a new 3 dimensional space to visualize the data. In the MDS, each point represents a single cell cultured under the defined media condition.

5.3.4 MDS Analysis of cytoskeletal descriptors discerns bone precursors within the first 24 hours

The high content imaging followed by MDS allows clear visualization of cell subpopulations grown in adipogenic versus osteogenic conditions (**Fig. 5.6A-C**). Cells grown in OS media locate primarily within a single cluster (OS blue cluster) (**Fig. 5.6A-C**). Cells cultured under AD and basal media (BA) segmented almost entirely into overlapping clusters (red AD/black BA cluster) (**Fig. 5.6D-F**), with limited overlapping with the OS cluster. To determine whether these clusters are reasonably indicative of commitment to their respective lineages, these results were compared with the fast blue/Oil Red O (FBOR) studies of cells under the same conditions (**Fig. 5.3A-D**). FBOR staining correlates highly with 24 MDS predictions supporting that the identified clusters, and therefore cytoskeletal morphologies, are encoding commitment to specific cell phenotypes. Cells cultured at 3,000 cells per cm² in OS media demonstrated a majority of cells with significant alkaline phosphatase activity indicating their commitment toward the osteoblastic phenotype. In contrast, cells cultured in AD or basal media displayed fewer cells with significant alkaline phosphatase activity, as well as sporadic oil red O positive cells in the adipogenic condition.

Predicting stem cell lineage outcomes is challenged by inherent variability in the stem cell populations. For hMSCs, this variability may result from biological differences in the donor source of cells (330), age of the donor (95), and passage number within a given donor source (331). To examine whether the high-content

descriptor-based segmentation of cell populations visualized were donor or passage dependent, experiments were performed with 2 different donors (age 22 and 36) and with 2 different passage numbers (**Fig. 5.6**). When comparing across different cell sources (compare **Fig. 5.6A-C**), clear segmentation of adipogenic and osteogenic treated cell populations is observed in all cases. Additionally, in all instances, the OS treated cells segmented from the AD/BA treated cells (**Fig. 5.6E-F**). Validation of the OS versus AD segmentation produced by the MDS for the different conditions was performed utilizing a support vector machine (SVM) to classify the different grouping (**Fig 5.6A-C**). Statistics from the SVM indicate that the MDS identifies and distinguishes OS treated cells with high accuracy, specificity, and sensitivity from AD treated cells.

5.3.5 Cytoskeletal descriptors capture the substrate-governed time evolution of lineage commitment

Unlike their fibronectin-coated counterparts, hMSCs cultured on glass substrates without fibronectin pre-treatment showed no definable clusters for either the OS or AD treated cells at 24 hours (**Fig. 5.7A-B**). Time sequence analysis (**Fig. 5.7C-F**) of the MDS for cells cultured in OS or AD conditions indicate that on untreated glass, these characteristic morphometric features developed between 48 and 72 hours. With increasing time (96 hours; **Fig. 5.7F**), the segmentation was more pronounced, indicating that within the time frame examined, the cytoskeletal based morphometrics of these two cell populations become progressively divergent.

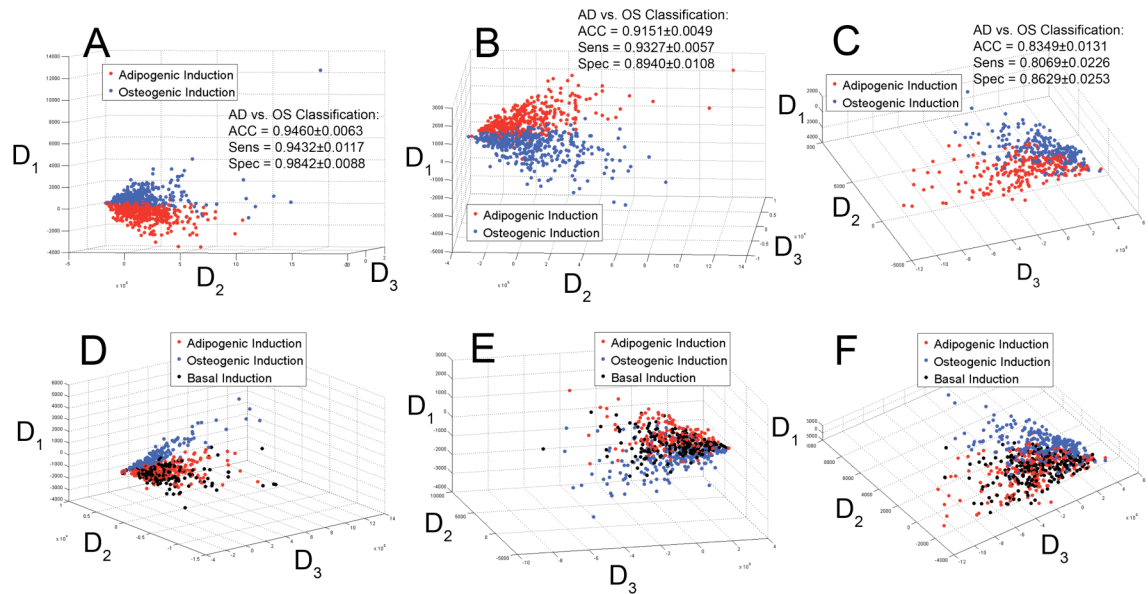


Figure 5.6: Cytoskeleton-based descriptors segment and identify individual osteoblastic cells within hMSC cultures exposed to soluble factors.

MDS results demonstrate that individual cells exposed to OS media (blue) cluster separately from cells in either AD (red) (**A-C**) or BA (black) (**D-F**) media. All cells were cultured on fibronectin pre-conditioned glass at 3,000 cells per cm². This segmentation was observed in at least three different cultures consisting of two donors (Donor 1 = 36 year old male (**A, D, B, E**); Donor 2 = 22 year old female (**C, F**)) and two passages (2 (**A, C, D, F**) and 4 (**B, E**)). No segmentation was observed between the AD and BA media conditions (**D-F**). For (**A-C**) data are pooled from 4 different wells for each condition, in (**D-F**) data is pooled from 2 wells for each condition. (**A-C**) Support vector machine (SVM) classification of clustering evident in the MDS graphs supports that when comparing OS versus AD treated cells classification can be achieved with high accuracy (ACC), sensitivity (Sens), and specificity (Spec). Error reported on SVM classification

represents the standard deviation for ACC, Sens, and Spec for N=50 two-fold cross validation pseudo-experiments of MDS data plotted in **(A-C)**.

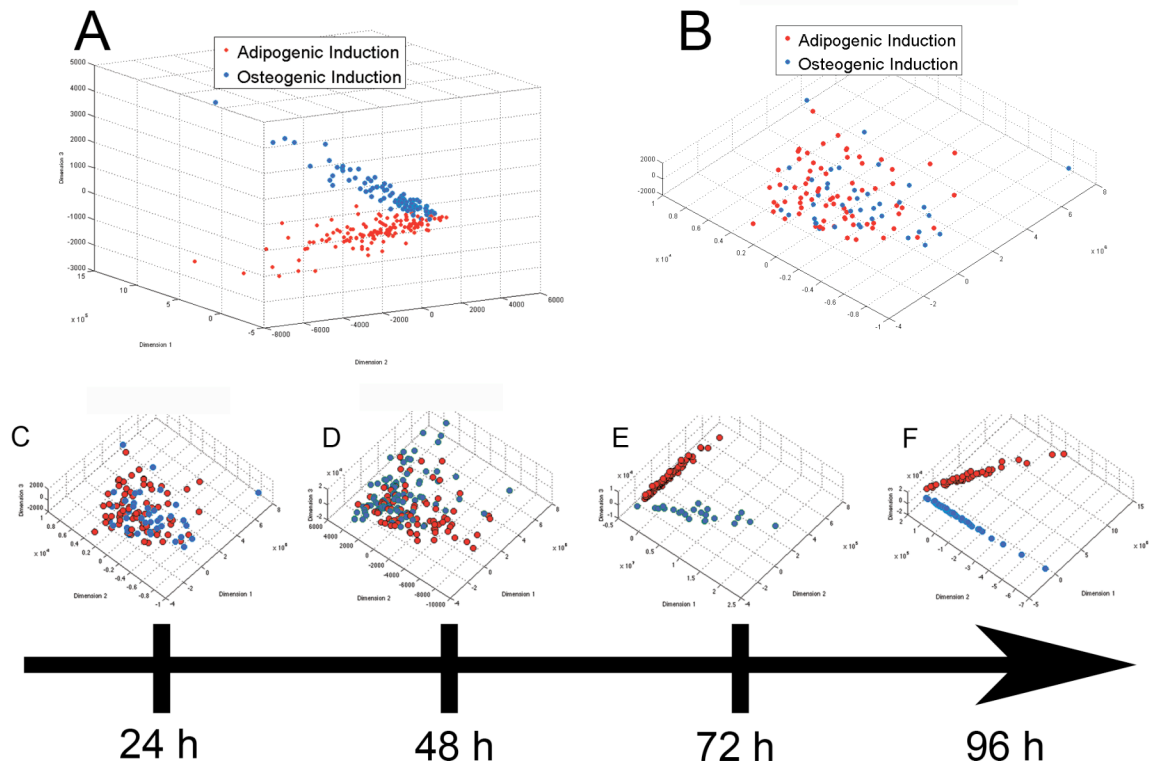


Figure 5.7: Cytoskeletal based morphometric segmentation kinetics occur in a ligand-dependent manner.

hMSCs were cultured in either AD or OS media on glass substrates with **(A)** and without **(B)** fibronectin pre-treatment for 24 hours. At 24 hours the fibronectin-pretreated substrates demonstrate a clear segmentation of the hMSCs treated with AD or OS induction whereas glass alone conditions do not. Over time with the non-conditioned glass, the cytoskeletal based segmentation process becomes progressively more pronounced with culture time **(C-F)**. The MDS of cells taken at 24 hours **(C)**, 48 hours **(D)**, 72 hours **(E)**, and 96 hours **(F)** are shown. No clear segmentation was seen on the glass substrate until 72 hours of culture. Data is shown from one representative time course experiment.

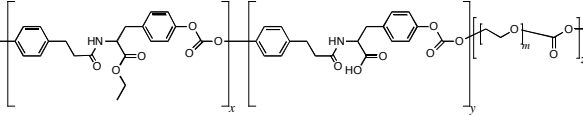
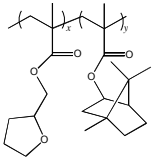
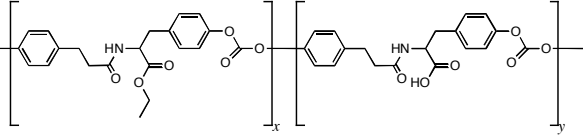
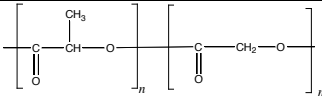
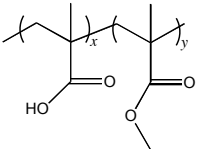
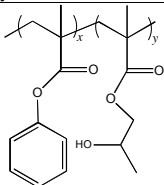
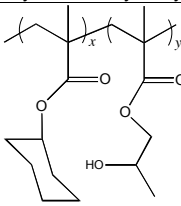
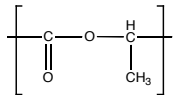
5.3.6 24 h Forecasting of hMSC osteoblastic lineage outcomes at two weeks via high content morphometric descriptors

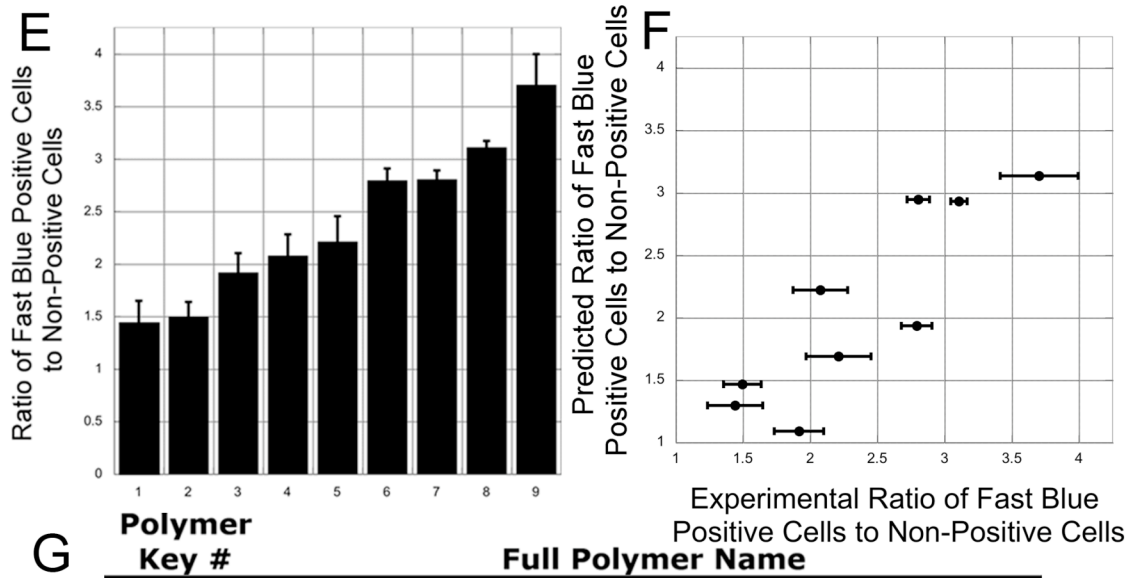
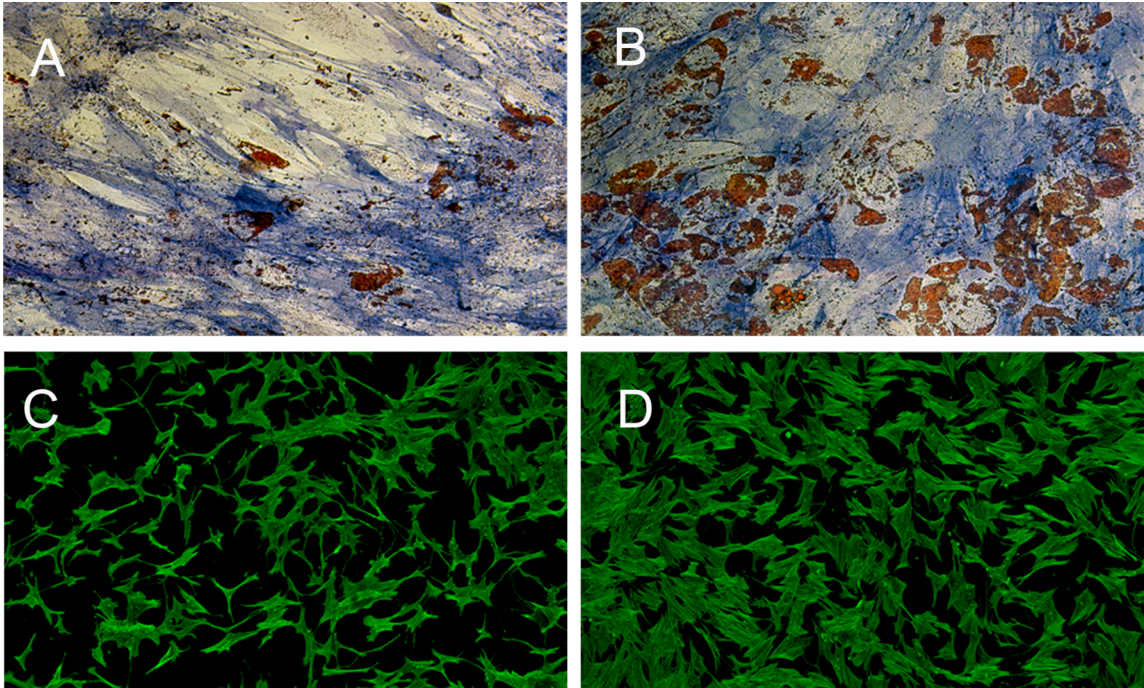
We next examined whether the morphometric approach could be applied to predict osteoblastic differentiation of hMSCs on complex engineered synthetic substrates that promote variable degrees of osteoblastic differentiation behaviors. Nine polymers with diverse physicochemical properties (**Table 5.2**) are used in the test case based on their ability to support in excess of 50% of the cells toward the osteoblastic lineage at 2 weeks. High seeding density (21,000 cells/cm²) and mixed induction media were employed to rank-order and parse out materials that potentiate osteogenic differentiation (**Fig. 5.8**). Examination of the 24-hour high-content images of hMSCs demonstrated no apparent differences in cell morphology elicited by the materials (**Fig. 5.8C-D**). However, FBOR analysis of hMSCs cultured on these materials demonstrated substrate-dependent staining in terms of the ratio of osteoblastic committed cells versus non-osteoblastic committed cells (**Fig. 5.8E**). Utilizing the previous outlined approach (**Fig. 5.5**) the MDS results for individual polymer samples showed two distinct cell fates within a given sample (**Fig. 5.9**). This divergent cell segmentation is attributed to the same divergence seen in the OS versus AD control conditions seen in **Fig. 5.5**. Calculating the ratio of cells that cluster in the osteoblastic regime (identified by the larger of the two clusters) allowed for the prediction of the ratio of cells that will become osteoblasts versus those that will not (**Fig. 5.8F**). This prediction was compared with the experimentally observed FBOR results obtained at 2 weeks for the same polymers (**Fig. 5.8E**). Polymer

chemistry appeared to have a large effect on hMSC differentiation with the ratio of cells that are fast blue positive to those that are not ranging from approximately 1.50 to almost 3.75 for the tested materials (**Fig. 5.8E**). The 24 hour morphometric-based prediction was compared with the experimentally captured FBOR staining. A high correlation (Pearson correlation coefficient = 0.87) results between the MDS based 24 h predictions and the 2 week experimental values (**Fig. 5.8F**).

Table 5.2: The single cell morphometric methodology can be used to assess hMSC differentiation on a wide array of biomaterials.

The 8 synthetic materials utilized to promote altered bone versus non-bone differentiation ratios are shown. Chemical formula, chemical composition, molecular weight (M_n , M_w), polydispersity (PDI), glass transition temperatures (T_g) and air-water contact angle is reported for all the materials. All values were measured except for the T_g for PLLA and PLGA, which were obtained from the literature. As can be seen, the morphometric approach can be applied on materials representing a varied material space. Three separate classes of synthetic materials were chosen including polycarbonates, polymethacrylates, and poly(α -hydroxy ester)s. All values are \pm the standard deviation. Note: for poly(70%methacrylic acid-co-30%methyl methacrylate) no T_g was found (NF) before the polymer's decomposition temperature.

Polymer	Molecular Weight	PDI	T _g (°C)	Air Water Contact Angle
 <p>poly(82%DTE-co-10%DT-co-8%PEG_{1K} carbonate)</p>	M _n = 120K M _w = 171K	1.4	46 20	72.5°±2.6
 <p>poly(71%tetrahydrofurfuryl-co-29%-isobornyl methacrylate)</p>	M _n = 249K M _w = 514K	2.1	56	68.2°±1.0
 <p>poly(90%DTE-co-10%DT carbonate)</p>	M _n = 241K M _w = 316K	1.3	101	72.7°±1.4
 <p>poly(50%D,L-lactic-co-50%glycolic acid)</p>	M _n = 50K M _w = 88K	1.8	42	70.8°±0.9
 <p>poly(70%methacrylic acid-co-30%methyl methacrylate)</p>	M _n = 87K M _w = 107K	1.2	NF	80.1°±1.0
 <p>poly(78%benzyl-co-22%hydroxypropyl methacrylate)</p>	M _n = 121K M _w = 308K	2.5	72	63.5°±4.4
 <p>poly(30%cyclohexyl-co-70%hydroxypropyl methacrylate)</p>	M _n = 331K M _w = 742K	2.2	92	89.9°±2.3
 <p>poly(L-lactic acid)</p>	M _n = 109K M _w = 182K	1.7	66	73.7°±0.8



Polymer Key #	Full Polymer Name
1	poly(82%DTE-co-10%DT-co-8%PEG1K carbonate)
2	poly(71%tetrahydrofurfuryl-co-29%-isobornyl methacrylate)
3	poly(90%DTE-co-10%DT carbonate)
4	poly(lactic-co-glycolic acid)
5	poly(70%methacrylic acid-co-30%methyl methacrylate)
6	poly(78%benzyl-co-22%hydroxypropyl methacrylate)
7	Collagen
8	poly(30%cyclohexyl-co-70%hydroxypropyl methacrylate)
9	poly(L-lactic acid)

Figure 5.8: Altered hMSC osteoblastic commitment resulting from substrate may be predicted based on MDS at 24 hours.

(A-B) At constant seeding density (21,000 cells per cm²) and applied soluble cues (MX media) synthetic substrates alter the percentage of cells that differentiate toward the osteoblastic lineage at 2 weeks as assessed by FBOR staining. FBOR images are shown for polymer 8 **(A)** and 1 **(B)**. **(C-D)** While the FBOR staining in **(A-B)** shows differences in the ratio of osteoblastic versus non-osteoblastic cells on different substrates, no obvious morphologic differences in cytoskeletal morphology are seen in the 24 h tile scan actin-stained images shown for the same polymers (8 **(C)** and 1 **(D)**). **(E)** Quantification of the ratio of fast blue positive cells to non-fast blue positive cells for each substrate shows ratios ranging from approximately 1.5 to 3.75. Error bars represent the standard deviation of N=2-4 experiments per substrate. **(F)** Scatter plot with the X-axis representing the ratio of 2-week cells experimentally observed becoming osteoblasts to those not committed to becoming osteoblasts, versus the 24 hour morphometric/MDS prediction for the same ratio (Y-axis). A high degree of correlation between the prediction and observed percent of osteoblasts was seen (Pearson correlation coefficient = 0.87). The X error bars represent the standard deviation for N=2-4 independent experiments. **(G)** Table listing full polymer names with corresponding keyed system shown in **(F)**.

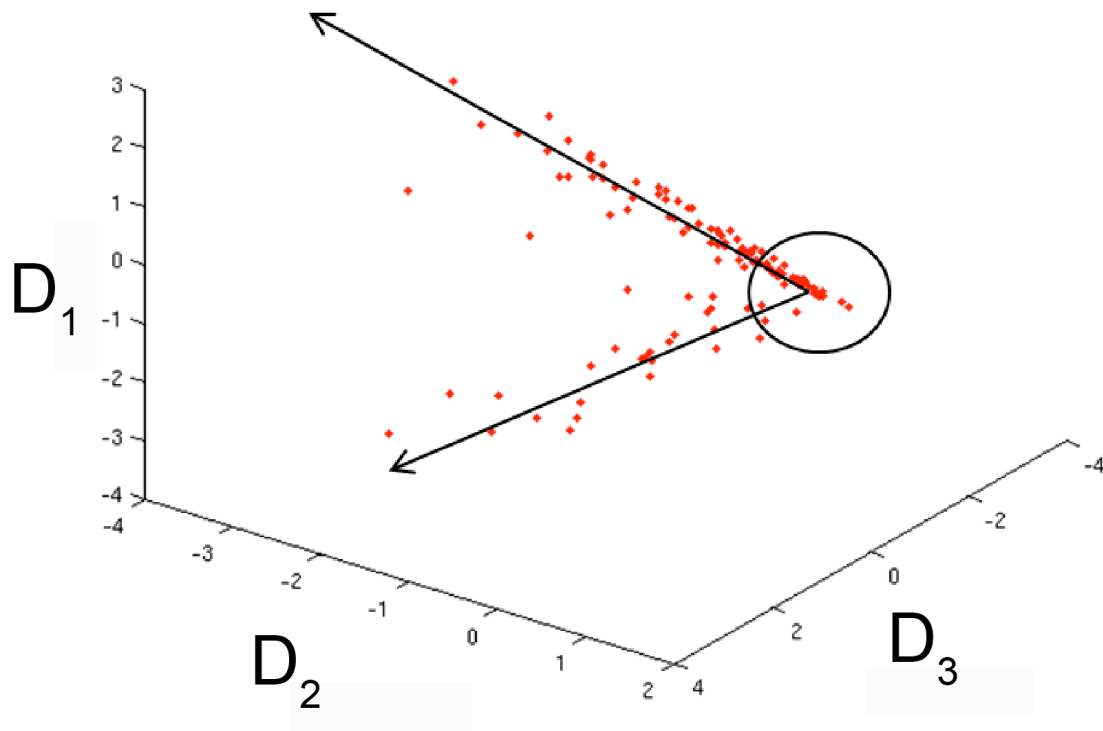


Figure 5.9: hMSCs cultured on synthetic/ECM substrates demonstrate two separate definable clusters within a single image.

Running of the MDS upon the individual cell morphometrics for a single sample of cells cultured upon poly(30% cyclohexyl-co-70% hydroxypropyl methacrylate) demonstrates that the MDS-processed cells are scattered via 2 different trajectories. It is hypothesized that these trajectories correspond to osteoblastic-committed cells and non-osteoblastic-committed cells respectively. Each point in the graph represents a single cell. All cells were taken from a single tile scan image and were cultured within the same well under a similar milieu. Cells were cultured at 21,000 cells per cm² in 50:50 mixed AD:OS media. These conditions were chosen to maximize the bi-potential nature of the culture.

5.4 Discussion:

“High content” cell morphology-based screening approaches have been developed for the screening of potential pharmaceuticals and biologically active small molecules, but these strategies have yet to become widespread for stem cell and tissue engineering applications. We demonstrate here that classifications of individual cell fates accurately predict long-term cellular behaviors days to weeks before they are experimentally detected. We also suggest that these classifications can be modulated by variations in the stem cell environments (biomaterial substrates and soluble cues). Previous work on hMSC differentiation reports links between global cell shape parameters and MSC differentiation behavior (87). However, this study finds that first moment shape descriptors alone fail to capture the heterogeneity and segregation of hMSCs at early time points (**Fig. 5.3H**). To capture these hallmark cytoskeletal “fingerprints” of osteoblastic committed precursors, we suggest that the high content methodology proposed in this study is valuable (**Fig. 5.5**).

The proposed methodology captures and quantifies the degree of heterogeneity within a given cell culture. **Fig. 5.3A-C** clearly demonstrate that hMSCs rarely behave as single cell phenotype in culture. Rather, heterogeneous pockets of cells that adopt similar fates appear. Unlike pooled analysis methods such as gene microarrays, PCR and well plate-based colorimetric end point analyses (e.g., fluorescent alkaline phosphatase and lipid accumulation kits), the high content morphometric approach is able to capture the unique cytoskeletal

characteristics of each cell and correlate them with its own cellular behavior. The ability to parse cells on a cell-by-cell basis represents a fundamental shift in the approach to stem cell characterization. By treating each cell as its own experimental data point, it is possible to increase both the informational yield and statistics of a given assay without increasing the number of samples or conditions analyzed (332).

The differentiation of hMSCs toward terminal phenotypes represents a biological process occurring over days to weeks. Gene expression analyses have demonstrated that transcription of genes traditionally indicative of commitment toward the osteoblastic (319) and adipocytic (114, 329) lineages (RUNX2 and PPAR γ respectively) are largely observed after 3 or more days in differentiation cultures. While expression of these genes are traditionally considered the first definitive markers of hMSC lineage commitment, studies have demonstrated that events occurring much earlier are linked to end-stage phenotypic expression. Changes in initial cell seeding density, cell shape and early cytoskeletal mechanics display the ability to influence MSC terminal behavior (71, 87).

The cytoskeletal morphometrics, which underlie the classification proposed in our study, reinforce the notion that the actin cytoskeleton plays a dominant role in regulating hMSC differentiation. This likely occurs via cell shape, Rho, ROCK, and cytoskeletal tension mechanisms, which promote osteoblastic induction (66, 87, 306). More specifically, the actin cytoskeleton plays a dominant role in regulating the differentiated phenotype. Cytochalasin D treatment to disrupt actin organization is sufficient to prevent expression of

markers of differentiation in hMSCs under osteoblastic induction (306). Furthermore, studies have proposed a detailed mechanism in which actin-based cell shape, Rho, ROCK and cytoskeletal tension influence hMSC differentiation. These studies demonstrated that the actin cytoskeleton induced up-regulation of RhoA (205), and subsequently ROCK, in spread cells results in preferential commitment of hMSCs to osteoblastic rather than adipocytic lineages (87). The total activity of ROCK, and therefore tendency to commit to one lineage versus another, may be captured in the morphology of individual actin fibers as different activities of ROCK result in altered actin fiber thickness and density (202). Additionally, transient expression of a glycerophosphodiester phosphodiesterase localized to the actin cytoskeleton results in both morphologic changes of the cytoskeleton and increases in alkaline phosphatase activity (333). Thus, within the context of the previously established framework linking the actin cytoskeleton to the osteoblastic phenotype in hMSCs, it follows that the cell decision-making process may be encoded within the cytoskeleton itself.

Actin filament organization throughout a cell has been associated with a number of intracellular signaling pathways and events including activation of the mitogen-activated protein kinases (MAPKs) (334), NF- κ B signaling (335), phosphoinositol kinase signaling (336), calcium signaling (337) and regulation of transcriptional events (338). Quantitative morphologic changes captured by the cytoskeletal descriptors may provide a metric of the signaling state of cells, an area that warrants further investigation. Therefore, the morphometrics presented

within this study may be useful not only in predicting stem cell fate, but in more generalized cell behavioral and signaling analyses.

The methodology of morphometric profiling of cell behaviors could be refined in the future to address discrimination of different lineage types (beyond osteogenic versus adipogenic, for example), and also temporal changes in differentiation within dynamic conditions. Currently, our predictions appear valid when the induction stimuli (i.e., substrata or soluble factors) remain unchanged for the entire period of culture, but could be examined when hMSCs transdifferentiate into other lineages (318). The questions to address in the future are which cytoskeletal descriptors if any are unique to specific lineages, and whether such descriptors can help parse multiple lineages. Our MDS-based segmentation correctly parses cells cultured under osteogenic conditions, but given its current one-reporter (actin)-based parsing process, it is unable to parse adipogenic cells from those under basal conditions (**Fig. 5.6D-F**). This is possibly due to lack of true adipogenic differentiation under the sparse seeding conditions we employed or because our imaging did not extend to the formative time course of cytoskeletal rearrangement indicative of adipocytic lineage commitment. Further, in the current form, the actin-based profiling could not be extended to parse cells near confluence in adipogenic versus basal media, but newer methods could be developed based on nuclear morphology (339) where cell-cell segmentation is not necessary.

In this study, fibronectin pre-conditioning had a marked effect on accelerating the kinetics of hMSC lineage commitment. Additionally, as small

changes in substrate chemistry can significantly affect matrix ligand conditioning (219, 258), we examined whether our high content stem cell profiling approach could help discriminate hMSC commitment to distinct lineages on nine different substrates. The physicochemical properties of such substrates themselves play a critical role in steering the percentage of cells that commit to specific fates (**Fig. 5.8E**). It is hypothesized that when a stem cell is given all of the necessary soluble factors to differentiate into multiple terminal cell types, the conformation of the cell, as influenced by the substrate, specifies the probability of differentiating into certain fates. The differences in hMSC commitment between polymer samples likely results from the chemical modifications in the polymer backbones. Previous work with hMSCs on self-assembled monolayers (315) and poly(ethylene glycol)-variant materials (328) confirms that material chemistry can affect osteoblastic lineage commitment and differentiation. For the nine polymers assessed in this study, a high degree of correlation between the 24-hour predictions and the experimentally observed 2-week FBOR was observed (0.87). Despite the seeming complexity of the large number of varied polymer surface properties that could influence stem cell differentiation, we believe cells integrate such signals into early intracellular morphological cues within 24 hours that predict the behavior out at two weeks. Thus lineage fates may be driven by rapid deterministic differentiation events early on and not necessarily by different growth kinetic behaviors (87).

One of the implications of using this image-based approach is that it is not necessary to hypothesize the existence of significantly different fates of the cell

before identifying the fact that multiple cell fates may exist. Since the individual cells compared in this study segregate so readily into the different clusters, there may exist a method to first image a cell and associate it with a currently unknown fate. After a cell has been associated with an unknown fate, these cells can then be separated and cultured independently. This may allow researchers to obtain homogenous populations of cells even when the induction of cell formation is not perfect. The ability to do so allows one to explore the pathways that lead to differentiation in greater detail because it becomes possible to isolate the main decision points (i.e., the small perturbations within the system that force the cell down one specific fate). Secondly, it may increase the fidelity of results from experiments such as microarrays, in which it is necessary to obtain mRNA expression levels from a population of cells. Populations of different cells, each, would normally adversely affect such results exhibiting their own lineage-specific gene expressions, therefore making it difficult to identify the role of specific genes in different cell lines.

5.5 Conclusion:

We have shown that through “high-content” morphometric analyses it is possible to identify the differentiation behavior of stem cells early within culture periods. This methodology applies to the differential behavior of these cells resulting from altered soluble factors, ligand conditioning or synthetic/biomimetic substrates. These findings are significant because they first show that surface chemistry plays a critical role in the kinetics of cellular differentiation. Additionally, the ability to identify cellular fates early on may allow us to establish a time line for cellular differentiation and identify critical points in cellular evolution for further assaying. The ability to obtain reasonably accurate predictions of cellular functions early opens up new approaches for the: screening of different polymers for directed stem cell differentiation, separating heterogeneous populations of cells, and increasing the fidelity of cellular differentiation assays. Finally, the MDS based stem cell identification could be utilized as an approach to rapidly screen and identify lead biomaterials for use in regenerative medicine.

6 Research Summary and Future Directions

6.1 Research Summary

This dissertation focused on addressing the needs of the tissue engineering community through the development of a novel “high-content” morphology-based imaging platform. This methodology was developed to address the critical needs and priorities of the field as highlighted in the MATES report (47): “(1) understanding the cellular machinery; (2) identifying and validating biomarkers and assays; (3) advancing imaging technologies; (4) defining cell/environment interactions; and (5) establishing computational modeling systems”. The hypothesis was posed that high-content morphometric-based imaging in combination with computational modeling methods will provide early predictive measures of cell fate and function as well as capture cytoskeletal involvement in complex material-mediated cell behaviors. To test the validity of the hypothesis four separate aims were undertaken. First, we developed a methodology for obtaining high-content feature-based descriptors of cytoskeletal and cytoplasmic markers. This methodology demonstrated that high-content imaging could characterize cell attachment, apoptotic behavior and cytoskeletal organization in response to culture on a limited sample of tyrosine-derived polycarbonates. Second, the high-content methodology was combined with a gradient-based polymer coated substrate approach to simultaneously elucidate the response of cells to continuous changes in surface roughness and discrete changes in surface chemistry. The high-throughput nature of the gradient setup

allowed for the rapid screening of global cell functions such as cell attachment. By coupling this analysis with the high-content approach, it was possible to propose unique aspects of global cell shape and signaling pathways that were altered/activated in response to surface roughness and specific chemistries. Therefore, the gradient and high-content approaches synergized to provide rapid assessment of cell response to material composition and topography while providing in depth single cell features that responded to these material factors. Third, the high-content approach was expanded to study cell response to a compositionally similar and systematically varied library of 14 tyrosine-derived polycarbonates. In this study it was demonstrated that the actin-based cytoskeleton of human Saos-2 cells responded in material-dependent manners. This cytoskeletal organizational response was shown to occur in parallel with complex material-mediated changes in Saos-2 cell proliferation and mineralization. In an attempt to link the early (24 hour) changes in material influenced cytoskeletal changes to the 3 week mineralization response on the same materials computational modeling methods were employed. Utilizing the 24 hour morphology, the computational model was able to predict the 3 week mineralization response with limited success. The limitation of the prediction was attributed to the complexity of the functional assay chosen (i.e., mineralization) and to the cancer-like nature of the Saos-2 cells. Therefore, in the fourth aim, human mesenchymal stem cells (hMSCs) were grown on synthetic and biomimetic surfaces. Material and soluble cues were used to promote divergences in lineage commitment of the hMSCs. High-content morphometrics

based on actin cytoskeletal organization taken at 24 hours demonstrated segregation of cell populations based on certain unique feature combinations. The feature-based methodology not only correlated well with 2 week differentiation behaviors, but demonstrated that the time scale of the image feature-based cell population segregation may be hastened or slowed by the ligand conditioning status of the materials. Finally, utilizing the 24 hour morphometric cell population segregation on synthetic materials, it was possible to forecast 2 week differentiation behaviors with a high degree of correlation.

Based on the findings discussed within the individual chapters of this dissertation, it was concluded that the hypothesis was valid. High-content morphometric imaging of early cell response captures long-term, material and soluble factor dependent behaviors. This work built on previous studies by Olson et al., which indicated that cell populations could be classified based solely on textural analyses used in conjunction with computational classification techniques (320). Confocal and/or epifluorescent imaging remain mainstays of cell characterization. However, traditional analysis of cell morphology has been limited to simple first order metrics of global cell shape including but not limited to: cell area, aspect ratio, and cell shape factor. When the cytoskeletal organization is analyzed, it is generally done so in a qualitative manner. At best, some studies have attempted semi-quantitative approaches to characterize the total amount of cytoskeletal proteins present. However these findings generally fail to mirror the associated qualitative assessments (154). A major finding of this work is that when analyzed in a strictly quantitative manner, the cytoskeleton,

particularly actin, acts as a sensitive probe of cell response. Utilizing the morphometric-based analysis presented within this dissertation, it is possible to capture subtle changes in material influenced cytoskeletal organization and forecast drastic divergences in cell behaviors weeks before they occur.

In fact, this study found that changes in cytoskeletal shape may be the one of the earliest markers/indicators of cellular outcomes. Therefore, while this study chose to focus on hMSC lineage commitment to either the adipocytic or osteoblastic lineages, this methodology may be applicable to other cell phenotypes or even other cell lines. hMSCs maintain the ability to differentiate into a number of cell phenotypes. Studies have investigated other lineages such as: chondrocytes (68), myofibroblasts (340), neurons (341), myoblasts (342, 343) and other cell types of all three germ layers (55). The high-content platform highlighted within this dissertation may be used to probe the role of the cytoskeleton and possibly predict hMSC differentiation to any of these aforementioned cell lineages. Additionally the applicability could be expanded to other stem cells. Recently, Mangoubi and coworkers utilized an image-based approach to classify colonies of human embryonic stem cells (hESCs) as either undifferentiated or differentiated (321). High-content cytoskeletal-based imaging may provide new methods to study hESC differentiation as well as examine the role that the cytoskeleton plays in early differentiation events. In conclusion, this dissertation has presented a cell characterization approach that provides: predictive measures of long-term cell behaviors at early time points, the effective forecasting of stem cell lineage commitment on complex biomaterials; real time

measures of stem cell fates and identification of when lineage commitment is identifiable; cell-by-cell based analysis that is able to capture the heterogeneity of sample populations; and the ability to parse out cell response influenced by multiple stimuli (e.g., soluble and material cues).

6.2 Future Directions

6.2.1 Cytoskeletal Descriptor Pathway Elucidation

The high-content morphometric analysis discussed within this dissertation represents a novel method to characterize and forecast cell response to material and soluble cues. However, the exact manner by which these descriptors capture key mechanistic events in cell behavior remains unclear. Previously, it has been shown that subsets of the molecules believed to be responsible for hMSC lineage commitment are those that also determine actin stress fiber shape and distribution (87, 202, 306, 344, 345). Therefore, it is possible that the captured characteristic cytoskeletal feature combinations represent cytoskeletal changes that are upstream or downstream of these signaling cascades. Alternatively, as actin organization is involved in RNA transcription (338, 346), it is possible that the descriptors themselves represent changes at the transcriptome level. Therefore, to probe the role of the descriptors within the context of the intracellular machinery and signal transduction pathways that lead to ultimate cell fate, two strategies may be employed. Utilizing systems biology approaches, the effect of Rho GTPases and their downstream effectors on actin

morphogenesis may be ascertained through the selective inhibition of each of these molecules. This will allow the determination of the resultant actin shape as a function of the activity of these molecules therefore directly linking intracellular signaling activities with their associated descriptor combinations. Second, gene microarray analyses may be used to discern changes in the transcriptional activity of hMSCs (110, 319, 329). By utilizing microarray assays at time points proximal to those of descriptor evolution it may be possible to highlight characteristic genes that are up regulated and therefore contributory and/or resultant of the cytoskeleton-based descriptors. Ultimately, when combined, the two methods may provide a detailed mechanism by which the high-content actin-based morphometric descriptors encode or dictate cell responses.

6.2.2 Three Dimensional High-Content Descriptor Calculation

The ultimate success of tissue engineering depends on the ability to fabricate constructs that mimic the function and morphology of endogenous tissues. While 2D systems provide convenient models of hMSC behavior, ultimately, implantable devices must be 3D in nature. The culture, expansion and differentiation of hMSCs in 3D scaffolds has been applied to create tissue-engineered products including skin substitutes (16, 340), bone (347-350), cartilage (350, 351) and fat (349). Currently, the high-content morphometric approach has been demonstrated in strictly two-dimensional cultures. However, the method may demonstrate utility in characterizing hMSC behavior in 3D environments. While the organization of the cytoskeleton of hMSCs has been largely characterized on 2D matrices, studies have shown that cells do form

matrix adhesions in 3D, but the organization and type of focal adhesions formed in 3D environments are distinct from those formed in their 2D counterparts (as reviewed in (352, 353)). Additionally, studies have demonstrated that when cultured in 3D versus 2D, fibroblasts adopt differences in cell morphology that occur in parallel with increases in cell behaviors such as proliferation, migration, and adhesion (354). Similar perturbations have been reported when comparing 2D and 3D cultures of hMSCs. Hishikawa and coworkers reported changes in gene expression profiles of osteoblastic genes with up-regulation of key osteogenic genes in 3D versus 2D cultures (355). Given the changes in both cell morphology and cellular behaviors seen when transitioning from a 2D to 3D system, the high-content morphometric approach presented within this dissertation may represent an ideal tactic to characterize hMSCs seeded within 3D scaffolds. Adaptation of the morphometric approach will require significant method development. First, the descriptor calculation approach highlighted within this dissertation works for two-dimensional projections of cellular ultrastructure. While the current ImagePro© software package defines 2D cell area, aspect ratio, and actin filament spatial distribution, new three-dimensional descriptors defining the 3D cytoskeletal organization must be developed. Secondly, material platforms for the scaffolds must be tested to ensure that they maintain the pluripotency of the stem cells while allowing directed differentiation to certain phenotypes. Studies have demonstrated that hMSCs remain pluripotent in 3D scaffolds while maintaining the ability to differentiate along multiple lineages (350, 356) utilizing similar soluble cocktails as those employed

in the 2D cultures within this dissertation. Finally, computational modeling systems will need to be developed to classify and/or predict hMSC differentiation behaviors as compared to their early 3D morphology. One interesting aspect to explore is whether the cytoskeletal features that are indicative of osteoblastic differentiation in 2D are similar or correlated to those in 3D. If so, this may present a new approach to predict hMSC differentiation behaviors in 3D scaffolds based solely on their more easily obtained 2D descriptor values.

6.2.3 Analysis of Other Intracellular Molecules for Descriptor Generation

The current study focused on high-content imaging of the actin cellular spatial arrangement and filament-defined cell shape. Actin was chosen because of its well-documented involvement in cell-material interactions as well as its intimate association with signaling cascades that affect cell differentiation, attachment and proliferation. While high-content descriptors of actin appear to provide useful metrics of cell responses, it remains possible that other intracellular elements may benefit from the presented morphometric approach. One such cytoskeletal element is the integrin. When cells contact surfaces, they use adhesion receptor molecules called integrins to initiate binding to matrix ligands adhering to the material surface. Integrins represent the mechanosensory machinery of the cell. The generation of force at integrin binding site leads to local focal adhesion assembly and activation of signaling cascades and gene transcription (176, 261-264). For example, integrins directly activate intracellular signaling processes with their adhesion and clustering resulting in activation of focal adhesion kinase (FAK), a non-receptor tyrosine

kinase recruited to focal adhesion areas of cells (357, 358). FAK activates a number of intracellular proteins and signaling molecules including Src, phosphatidylinositol 3-kinase, Grb2, p130^{Cas} and paxillin, which regulate cellular functions ranging from proliferation and apoptosis to migration (359-363). While the FAK mediated cascade was one of the first identified integrin mediated signals, independent activation of mitogen activated protein (MAP) kinase and the Ras GTPase superfamily by integrins has been shown (as reviewed in (364)). Activation of MAP kinase triggers the extracellular signal-regulated cascade (Erk) that regulates cell proliferation and differentiation; while the Ras GTPase superfamily including Rho, Rac, and CDC42 have been implicated in the cell cycle, cell morphogenesis and cell migration (94, 320, 365-367). Finally, integrin binding to substrates leads to changes in mRNA expression, translation and targeting (368-370). Overall, integrins maintain a crucial role in the mediation of the cellular response. Therefore detailed analysis of the cytoskeletal distribution and morphometrics of these adhesion complexes may provide insight into the signaling state of a cell and possibly act as accurate early predictive measures of long-term cell behaviors.

Cells have been described as structures supported by cytoskeletal elements in tension rather than supported by hydrostatic compressional continuity (170-173). In these models, the cytoskeleton of the cell couples the nucleus to integrins, therefore providing a path for the propagation of mechanical cues from the extracellular matrix to the control center of the cell, the nucleus (174). Therefore, the nucleus represents another intracellular element that may

benefit from the approach presented within this dissertation. Previous work on nuclear shape morphometrics has focused on the pathologic assessment of cancerous cells (371). However, nuclear shape may be indicative of more than carcinogenic progression, but also may be indicative of complex cell behaviors. For example, nuclear shape has been shown to strongly influence the expression of osteogenic genes in osteoblastic cells (324). Furthermore, studies by McBride et al. demonstrated that the nuclear shape of hMSCs was correlated with proliferation and expression of genes associated with differentiation (339). Therefore, a detailed morphometric analysis of nuclear shape or the distribution of key nuclear proteins may represent a viable method to define early metrics of cell behaviors. Transitioning from cytoskeletal to nuclear morphometrics has the added benefit of expanding the sample population to confluent cell cultures. Currently, the greatest limitation of the cytoskeletal-defined high-content imaging platform is that single cells must be resolved. Therefore, the analysis is not amenable to cell cultures where cells have become confluent. This represents a major limitation particularly with regards to adipocytic differentiation of hMSCs, which occurs primarily within confluent cultures. As cell nuclei may be resolved in confluent cultures, the adaptation of the high-content morphometric approach to cell nuclei may allow predictive measures of a wider and more robust range of cell fates and behaviors.

7 References

1. Langer R & Vacanti JP (1993) Tissue engineering. *Science* 260(5110):920-926.
2. Niklason LE & Langer R (2001) Prospects for organ and tissue replacement. *JAMA* 285(5):573-576.
3. U. S. Renal Data System (2008) *USRDS 2008 Annual Data Report: Atlas of Chronic Kidney Disease and End-Stage Renal Disease in the United States* (National Institutes of Health, Bethesda, MD), (National Institute of Diabetes and Digestive and Kidney Diseases).
4. OPTN (2009) Transplant : Organ by Diagnosis. 2009(February 24).
5. Beaty JH, Canale ST, & Campbell WC (2007) *Campbell's Operative Orthopaedics* (Elsevier Science); Campbell's Operative Orthopaedics 11th Ed.
6. Skalak R & Fox CF (1988) Tissue Engineering: Proceedings of a workshop held at Granlibakken. (Alan Liss, New York, NY).
7. Caplan AI (2007) Adult mesenchymal stem cells for tissue engineering versus regenerative medicine. *J Cell Physiol* 213(2):341-347.
8. Riazi AM, Kwon SY, & Stanford WL (2009) Stem cell sources for regenerative medicine. *Methods Mol Biol* 482:55-90.
9. Langer RS & Vacanti JP (1999) Tissue engineering: the challenges ahead. *Sci Am* 280(4):86-89.
10. Singh G & Kelly M (2005) Origins of the "Indian method" of nasal reconstruction. *Plast Reconstr Surg* 116(4):1177-1179.
11. Griffith LG & Naughton G (2002) Tissue engineering--current challenges and expanding opportunities. *Science* 295(5557):1009-1014.
12. Reffelmann T, Konemann S, & Kloner RA (2009) Promise of blood- and bone marrow-derived stem cell transplantation for functional cardiac repair: putting it in perspective with existing therapy. *J Am Coll Cardiol* 53(4):305-308.
13. Janssens S, Dubois C, Bogaert J, Theunissen K, Deroose C, Desmet W, Kalantzi M, Herbots L, Sinnaeve P, Dens J, Maertens J, Rademakers F, Dymarkowski S, Gheysens O, Van Cleemput J, Bormans G, Nuyts J, Belmans A, Mortelmans L, Boogaerts M, & Van de Werf F (2006) Autologous bone marrow-derived stem-cell transfer in patients with ST-segment elevation myocardial infarction: double-blind, randomised controlled trial. *Lancet* 367(9505):113-121.
14. Collins JM & Russell B (2009) Stem cell therapy for cardiac repair. *J Cardiovasc Nurs* 24(2):93-97.
15. Yang S, Leong KF, Du Z, & Chua CK (2001) The design of scaffolds for use in tissue engineering. Part I. Traditional factors. *Tissue Eng* 7(6):679-689.

16. Ma PX (2008) Biomimetic materials for tissue engineering. *Adv Drug Deliv Rev* 60(2):184-198.
17. Hubbell J (1995) Biomaterials in tissue engineering. *Nature Biotechnology* 13(6):565.
18. Shin H, Jo S, & Mikos AG (2003) Biomimetic materials for tissue engineering. *Biomaterials* 24(24):4353-4364.
19. Zhao J, Zhang N, Prestwich GD, & Wen X (2008) Recruitment of endogenous stem cells for tissue repair. *Macromol Biosci* 8(9):836-842.
20. Bezwada RS, Jamiolkowski DD, Lee IY, Agarwal V, Persivale J, Trenka-Benthin S, Ernetta M, Suryadevara J, Yang A, & Liu S (1995) Monocryl suture, a new ultra-pliable absorbable monofilament suture. *Biomaterials* 16(15):1141-1148.
21. Frazza EJ & Schmitt EE (1971) A new absorbable suture. *J Biomed Mater Res* 5(2):43-58.
22. Herrmann JB, Kelly RJ, & Higgins GA (1970) Polyglycolic acid sutures. Laboratory and clinical evaluation of a new absorbable suture material. *Arch Surg* 100(4):486-490.
23. Ray JA, Doddi N, Regula D, Williams JA, & Melveger A (1981) Polydioxanone (PDS), a novel monofilament synthetic absorbable suture. *Surg Gynecol Obstet* 153(4):497-507.
24. Athanasiou KA, Agrawal CM, Barber FA, & Burkhart SS (1998) Orthopaedic applications for PLA-PGA biodegradable polymers. *Arthroscopy* 14(7):726-737.
25. Attawia MA, Uhrich KE, Botchwey E, Fan M, Langer R, & Laurencin CT (1995) Cytotoxicity testing of poly(anhydride-co-imides) for orthopedic applications. *J Biomed Mater Res* 29(10):1233-1240.
26. Knowles JC (1993) Development of a natural degradable polymer for orthopaedic use. *J Med Eng Technol* 17(4):129-137.
27. Nair LS, Lee DA, Bender JD, Barrett EW, Greish YE, Brown PW, Allcock HR, & Laurencin CT (2006) Synthesis, characterization, and osteocompatibility evaluation of novel alanine-based polyphosphazenes. *J Biomed Mater Res A* 76(1):206-213.
28. Yaszemski MJ, Payne RG, Hayes WC, Langer R, & Mikos AG (1995) The in vitro mechanical strength and in vivo bone ingrowth of a degrading polymeric composite biomaterial. *Mater. Res. Soc. Symp. Proc.* 394(Polymers in Medicine and Pharmacy):21-24.
29. Liu HW, Chen CH, Tsai CL, Lin IH, & Hsiue GH (2007) Heterobifunctional poly(ethylene glycol)-tethered bone morphogenetic protein-2-stimulated bone marrow mesenchymal stromal cell differentiation and osteogenesis. *Tissue Eng* 13(5):1113-1124.
30. Ranger WR, Halpin D, Sawhney AS, Lyman M, & Locicero J (1997) Pneumostasis of experimental air leaks with a new photopolymerized synthetic tissue sealant. *Am Surg* 63(9):788-795.
31. Bennett SL, Melanson DA, Torchiana DF, Wiseman DM, & Sawhney AS (2003) Next-generation hydrogel films as tissue sealants and adhesion barriers. *J Card Surg* 18(6):494-499.

32. Gill IS, Ramani AP, Spaliviero M, Xu M, Finelli A, Kaouk JH, & Desai MM (2005) Improved hemostasis during laparoscopic partial nephrectomy using gelatin matrix thrombin sealant. *Urology* 65(3):463-466.
33. Buevich F, Do F, McJames J, Pulapura S, Edelman W, Moses A, Diamond M, & Timothy S (2007) Patent assigned to: TyRx Pharma Inc. US 2007/0198040 A1.
34. Morrison WA (2009) Progress in tissue engineering of soft tissue and organs. *Surgery* 145(2):127-130.
35. Nose Y & Okubo H (2003) Artificial organs versus regenerative medicine: is it true? *Artif Organs* 27(9):765-771.
36. Kohn J, Welsh WJ, & Knight D (2007) A new approach to the rationale discovery of polymeric biomaterials. *Biomaterials* 28(29):4171-4177.
37. Kaihara S, Borenstein J, Koka R, Lalan S, Ochoa ER, Ravens M, Pien H, Cunningham B, & Vacanti JP (2000) Silicon micromachining to tissue engineer branched vascular channels for liver fabrication. *Tissue Eng* 6(2):105-117.
38. Fidkowski C, Kaazempur-Mofrad MR, Borenstein J, Vacanti JP, Langer R, & Wang Y (2005) Endothelialized microvasculature based on a biodegradable elastomer. *Tissue Eng* 11(1-2):302-309.
39. Bhatia SN, Yarmush ML, & Toner M (1997) Controlling cell interactions by micropatterning in co-cultures: hepatocytes and 3T3 fibroblasts. *J Biomed Mater Res* 34(2):189-199.
40. Wendt D, Stroebel S, Jakob M, John GT, & Martin I (2006) Uniform tissues engineered by seeding and culturing cells in 3D scaffolds under perfusion at defined oxygen tensions. *Biorheology* 43(3-4):481-488.
41. Burg KJ, Holder WD, Jr., Culberson CR, Beiler RJ, Greene KG, Loeb sack AB, Roland WD, Eiselt P, Mooney DJ, & Halberstadt CR (2000) Comparative study of seeding methods for three-dimensional polymeric scaffolds. *J Biomed Mater Res* 51(4):642-649.
42. Lysaght MJ & Hazlehurst AL (2004) Tissue engineering: the end of the beginning. *Tissue Eng* 10(1-2):309-320.
43. Lysaght MJ, Nguy NA, & Sullivan K (1998) An economic survey of the emerging tissue engineering industry. *Tissue Eng* 4(3):231-238.
44. Lysaght MJ & Reyes J (2001) The growth of tissue engineering. *Tissue Eng* 7(5):485-493.
45. Lysaght MJ, Jaklenec A, & Deweerd E (2008) Great expectations: private sector activity in tissue engineering, regenerative medicine, and stem cell therapeutics. *Tissue Eng Part A* 14(2):305-315.
46. Johnson PC, Mikos AG, Fisher JP, & Jansen JA (2007) Strategic directions in tissue engineering. *Tissue Eng* 13(12):2827-2837.
47. U.S. Government Multi-Agency Tissue Engineering Science (MATES) Integracy Working Group (2007) Advancing tissue science and engineering: a foundation for the future. A multi-agency strategic plan. *Tissue Eng* 13(12):2825-2826.

48. Iwasa J, Engebretsen L, Shima Y, & Ochi M (2008) Clinical application of scaffolds for cartilage tissue engineering. *Knee Surg Sports Traumatol Arthrosc.*
49. Ohgawara H, Edamura K, Kawakami M, & Umezawa K (2004) Diabetes mellitus: rational basis, clinical approach and future therapy. *Biomed Pharmacother* 58(10):605-609.
50. Hutmacher DW (2000) Scaffolds in tissue engineering bone and cartilage. *Biomaterials* 21(24):2529-2543.
51. Priya SG, Jungvid H, & Kumar A (2008) Skin tissue engineering for tissue repair and regeneration. *Tissue Eng Part B Rev* 14(1):105-118.
52. Ohashi K (2008) Liver tissue engineering: The future of liver therapeutics. *Hepatol Res* 38(The 6th Japan Society of Hepatology Single Topic Conference: Liver Failure: Recent Progress and Pathogenesis to Management. 28–29 September 2007, Iwate, Japan):S76-S87.
53. Strehl R, Schumacher K, de Vries U, & Minuth WW (2002) Proliferating cells versus differentiated cells in tissue engineering. *Tissue Eng* 8(1):37-42.
54. Thomson JA, Itskovitz-Eldor J, Shapiro SS, Waknitz MA, Swiergiel JJ, Marshall VS, & Jones JM (1998) Embryonic stem cell lines derived from human blastocysts. *Science* 282(5391):1145-1147.
55. Jiang Y, Jahagirdar BN, Reinhardt RL, Schwartz RE, Keene CD, Ortiz-Gonzalez XR, Reyes M, Lenvik T, Lund T, Blackstad M, Du J, Aldrich S, Lisberg A, Low WC, Largaespada DA, & Verfaillie CM (2002) Pluripotency of mesenchymal stem cells derived from adult marrow. *Nature* 418(6893):41-49.
56. Friedenstein AJ (1976) Precursor cells of mechanocytes. *Int Rev Cytol* 47:327-359.
57. Owen M & Friedenstein AJ (1988) Stromal stem cells: marrow-derived osteogenic precursors. *Ciba Found Symp* 136:42-60.
58. Oh SH, Hatch HM, & Petersen BE (2002) Hepatic oval 'stem' cell in liver regeneration. *Semin Cell Dev Biol* 13(6):405-409.
59. Herrera MB, Bruno S, Buttiglieri S, Tetta C, Gatti S, Deregibus MC, Bussolati B, & Camussi G (2006) Isolation and characterization of a stem cell population from adult human liver. *Stem Cells* 24(12):2840-2850.
60. Toma JG, Akhavan M, Fernandes KJ, Barnabe-Heider F, Sadikot A, Kaplan DR, & Miller FD (2001) Isolation of multipotent adult stem cells from the dermis of mammalian skin. *Nat Cell Biol* 3(9):778-784.
61. Tumber T, Guasch G, Greco V, Blanpain C, Lowry WE, Rendl M, & Fuchs E (2004) Defining the epithelial stem cell niche in skin. *Science* 303(5656):359-363.
62. Zuk PA, Zhu M, Ashjian P, De Ugarte DA, Huang JI, Mizuno H, Alfonso ZC, Fraser JK, Benhaim P, & Hedrick MH (2002) Human adipose tissue is a source of multipotent stem cells. *Mol Biol Cell* 13(12):4279-4295.
63. Bunnell BA, Flaat M, Gagliardi C, Patel B, & Ripoll C (2008) Adipose-derived stem cells: isolation, expansion and differentiation. *Methods* 45(2):115-120.

64. Temple S (2001) The development of neural stem cells. *Nature* 414(6859):112-117.
65. Gage FH (2000) Mammalian neural stem cells. *Science* 287(5457):1433-1438.
66. Morrison SJ, White PM, Zock C, & Anderson DJ (1999) Prospective identification, isolation by flow cytometry, and in vivo self-renewal of multipotent mammalian neural crest stem cells. *Cell* 96(5):737-749.
67. Caplan AI (1991) Mesenchymal stem cells. *J Orthop Res* 9(5):641-650.
68. Pittenger MF, Mackay AM, Beck SC, Jaiswal RK, Douglas R, Mosca JD, Moorman MA, Simonetti DW, Craig S, & Marshak DR (1999) Multilineage potential of adult human mesenchymal stem cells. *Science* 284(5411):143-147.
69. Tocci A & Forte L (2003) Mesenchymal stem cell: use and perspectives. *Hematol J* 4(2):92-96.
70. Beyer Nardi N & da Silva Meirelles L (2006) Mesenchymal stem cells: isolation, in vitro expansion and characterization. *Handb Exp Pharmacol* (174):249-282.
71. Jaiswal N, Haynesworth SE, Caplan AI, & Bruder SP (1997) Osteogenic differentiation of purified, culture-expanded human mesenchymal stem cells in vitro. *J Cell Biochem* 64(2):295-312.
72. Ducy P, Zhang R, Geoffroy V, Ridall AL, & Karsenty G (1997) Osf2/Cbfa1: a transcriptional activator of osteoblast differentiation. *Cell* 89(5):747-754.
73. Jager M, Fischer J, Dohrn W, Li X, Ayers DC, Czibere A, Prall WC, Lensing-Hohn S, & Krauspe R (2008) Dexamethasone modulates BMP-2 effects on mesenchymal stem cells in vitro. *J Orthop Res* 26(11):1440-1448.
74. Cohen MM, Jr. (2006) The new bone biology: pathologic, molecular, and clinical correlates. *Am J Med Genet A* 140(23):2646-2706.
75. Ducy P, Schinke T, & Karsenty G (2000) The osteoblast: a sophisticated fibroblast under central surveillance. *Science* 289(5484):1501-1504.
76. Nakashima K & de Crombrughe B (2003) Transcriptional mechanisms in osteoblast differentiation and bone formation. *Trends Genet* 19(8):458-466.
77. Miyama K, Yamada G, Yamamoto TS, Takagi C, Miyado K, Sakai M, Ueno N, & Shibuya H (1999) A BMP-inducible gene, *dlx5*, regulates osteoblast differentiation and mesoderm induction. *Dev Biol* 208(1):123-133.
78. Newberry EP, Latifi T, & Towler DA (1998) Reciprocal regulation of osteocalcin transcription by the homeodomain proteins *Msx2* and *Dlx5*. *Biochemistry* 37(46):16360-16368.
79. Ryoo HM, Hoffmann HM, Beumer T, Frenkel B, Towler DA, Stein GS, Stein JL, van Wijnen AJ, & Lian JB (1997) Stage-specific expression of *Dlx-5* during osteoblast differentiation: involvement in regulation of osteocalcin gene expression. *Mol Endocrinol* 11(11):1681-1694.

80. Ulsamer A, Ortuno MJ, Ruiz S, Susperregui AR, Osses N, Rosa JL, & Ventura F (2008) BMP-2 induces Osterix expression through up-regulation of Dlx5 and its phosphorylation by p38. *J Biol Chem* 283(7):3816-3826.
81. Nakashima K, Zhou X, Kunkel G, Zhang Z, Deng JM, Behringer RR, & de Crombrughe B (2002) The novel zinc finger-containing transcription factor osterix is required for osteoblast differentiation and bone formation. *Cell* 108(1):17-29.
82. Bain G, Muller T, Wang X, & Papkoff J (2003) Activated beta-catenin induces osteoblast differentiation of C3H10T1/2 cells and participates in BMP2 mediated signal transduction. *Biochem Biophys Res Commun* 301(1):84-91.
83. Gong Y, Slee RB, Fukai N, Rawadi G, Roman-Roman S, Reginato AM, Wang H, Cundy T, Glorieux FH, Lev D, Zacharin M, Oexle K, Marcelino J, Suwairi W, Heeger S, Sabatakos G, Apte S, Adkins WN, Allgrove J, Arslan-Kirchner M, Batch JA, Beighton P, Black GC, Boles RG, Boon LM, Borrone C, Brunner HG, Carle GF, Dallapiccola B, De Paepe A, Floege B, Halfhide ML, Hall B, Hennekam RC, Hirose T, Jans A, Juppner H, Kim CA, Keppler-Noreuil K, Kohlschuetter A, LaCombe D, Lambert M, Lemyre E, Letteboer T, Peltonen L, Ramesar RS, Romanengo M, Somer H, Steichen-Gersdorf E, Steinmann B, Sullivan B, Superti-Furga A, Swoboda W, van den Boogaard MJ, Van Hul W, Vikkula M, Votruba M, Zabel B, Garcia T, Baron R, Olsen BR, & Warman ML (2001) LDL receptor-related protein 5 (LRP5) affects bone accrual and eye development. *Cell* 107(4):513-523.
84. Harada S & Rodan GA (2003) Control of osteoblast function and regulation of bone mass. *Nature* 423(6937):349-355.
85. Patel MS & Karsenty G (2002) Regulation of bone formation and vision by LRP5. *N Engl J Med* 346(20):1572-1574.
86. Grzesik WJ & Robey PG (1994) Bone matrix RGD glycoproteins: immunolocalization and interaction with human primary osteoblastic bone cells in vitro. *J Bone Miner Res* 9(4):487-496.
87. McBeath R, Pirone DM, Nelson CM, Bhadriraju K, & Chen CS (2004) Cell shape, cytoskeletal tension, and RhoA regulate stem cell lineage commitment. *Dev Cell* 6(4):483-495.
88. Ross FP, Chappel J, Alvarez JI, Sander D, Butler WT, Farach-Carson MC, Mintz KA, Robey PG, Teitelbaum SL, & Cheresch DA (1993) Interactions between the bone matrix proteins osteopontin and bone sialoprotein and the osteoclast integrin alpha v beta 3 potentiate bone resorption. *J Biol Chem* 268(13):9901-9907.
89. Engler AJ, Sen S, Sweeney HL, & Discher DE (2006) Matrix elasticity directs stem cell lineage specification. *Cell* 126(4):677-689.
90. Discher DE, Janmey P, & Wang YL (2005) Tissue cells feel and respond to the stiffness of their substrate. *Science* 310(5751):1139-1143.
91. Park KW, Halperin DS, & Tontonoz P (2008) Before they were fat: adipocyte progenitors. *Cell Metab* 8(6):454-457.

92. Beresford JN, Bennett JH, Devlin C, Leboy PS, & Owen ME (1992) Evidence for an inverse relationship between the differentiation of adipocytic and osteogenic cells in rat marrow stromal cell cultures. *J Cell Sci* 102 (Pt 2):341-351.
93. Dorheim MA, Sullivan M, Dandapani V, Wu X, Hudson J, Segarini PR, Rosen DM, Aulthouse AL, & Gimble JM (1993) Osteoblastic gene expression during adipogenesis in hematopoietic supporting murine bone marrow stromal cells. *J Cell Physiol* 154(2):317-328.
94. Jaiswal RK, Jaiswal N, Bruder SP, Mbalaviele G, Marshak DR, & Pittenger MF (2000) Adult human mesenchymal stem cell differentiation to the osteogenic or adipogenic lineage is regulated by mitogen-activated protein kinase. *J Biol Chem* 275(13):9645-9652.
95. Moerman EJ, Teng K, Lipschitz DA, & Lecka-Czernik B (2004) Aging activates adipogenic and suppresses osteogenic programs in mesenchymal marrow stroma/stem cells: the role of PPAR-gamma2 transcription factor and TGF-beta/BMP signaling pathways. *Aging Cell* 3(6):379-389.
96. Gimble JM, Morgan C, Kelly K, Wu X, Dandapani V, Wang CS, & Rosen V (1995) Bone morphogenetic proteins inhibit adipocyte differentiation by bone marrow stromal cells. *J Cell Biochem* 58(3):393-402.
97. Gori F, Thomas T, Hicok KC, Spelsberg TC, & Riggs BL (1999) Differentiation of human marrow stromal precursor cells: bone morphogenetic protein-2 increases OSF2/CBFA1, enhances osteoblast commitment, and inhibits late adipocyte maturation. *J Bone Miner Res* 14(9):1522-1535.
98. Thomas T, Gori F, Khosla S, Jensen MD, Burguera B, & Riggs BL (1999) Leptin acts on human marrow stromal cells to enhance differentiation to osteoblasts and to inhibit differentiation to adipocytes. *Endocrinology* 140(4):1630-1638.
99. Bennett CN, Longo KA, Wright WS, Suva LJ, Lane TF, Hankenson KD, & MacDougald OA (2005) Regulation of osteoblastogenesis and bone mass by Wnt10b. *Proc Natl Acad Sci U S A* 102(9):3324-3329.
100. Rosen ED & MacDougald OA (2006) Adipocyte differentiation from the inside out. *Nat Rev Mol Cell Biol* 7(12):885-896.
101. Gurnell M, Wentworth JM, Agostini M, Adams M, Collingwood TN, Provenzano C, Browne PO, Rajanayagam O, Burris TP, Schwabe JW, Lazar MA, & Chatterjee VK (2000) A dominant-negative peroxisome proliferator-activated receptor gamma (PPARgamma) mutant is a constitutive repressor and inhibits PPARgamma-mediated adipogenesis. *J Biol Chem* 275(8):5754-5759.
102. Masugi J, Tamori Y, & Kasuga M (1999) Inhibition of adipogenesis by a COOH-terminally truncated mutant of PPARgamma2 in 3T3-L1 cells. *Biochem Biophys Res Commun* 264(1):93-99.
103. Tontonoz P, Hu E, & Spiegelman BM (1994) Stimulation of adipogenesis in fibroblasts by PPAR gamma 2, a lipid-activated transcription factor. *Cell* 79(7):1147-1156.

104. Berger J & Moller DE (2002) The mechanisms of action of PPARs. *Annu Rev Med* 53:409-435.
105. Tontonoz P, Graves RA, Budavari AI, Erdjument-Bromage H, Lui M, Hu E, Tempst P, & Spiegelman BM (1994) Adipocyte-specific transcription factor ARF6 is a heterodimeric complex of two nuclear hormone receptors, PPAR gamma and RXR alpha. *Nucleic Acids Res* 22(25):5628-5634.
106. Tontonoz P, Hu E, Graves RA, Budavari AI, & Spiegelman BM (1994) mPPAR gamma 2: tissue-specific regulator of an adipocyte enhancer. *Genes Dev* 8(10):1224-1234.
107. Tontonoz P, Hu E, Devine J, Beale EG, & Spiegelman BM (1995) PPAR gamma 2 regulates adipose expression of the phosphoenolpyruvate carboxykinase gene. *Mol Cell Biol* 15(1):351-357.
108. Schoonjans K, Watanabe M, Suzuki H, Mahfoudi A, Krey G, Wahli W, Grimaldi P, Staels B, Yamamoto T, & Auwerx J (1995) Induction of the acyl-coenzyme A synthetase gene by fibrates and fatty acids is mediated by a peroxisome proliferator response element in the C promoter. *J Biol Chem* 270(33):19269-19276.
109. Schoonjans K, Peinado-Onsurbe J, Lefebvre AM, Heyman RA, Briggs M, Deeb S, Staels B, & Auwerx J (1996) PPARalpha and PPARgamma activators direct a distinct tissue-specific transcriptional response via a PPRE in the lipoprotein lipase gene. *EMBO J* 15(19):5336-5348.
110. Nakamura T, Shiojima S, Hirai Y, Iwama T, Tsuruzoe N, Hirasawa A, Katsuma S, & Tsujimoto G (2003) Temporal gene expression changes during adipogenesis in human mesenchymal stem cells. *Biochem Biophys Res Commun* 303(1):306-312.
111. Muruganandan S, Roman AA, & Sinal CJ (2009) Adipocyte differentiation of bone marrow-derived mesenchymal stem cells: cross talk with the osteoblastogenic program. *Cell Mol Life Sci* 66(2):236-253.
112. Wu Z, Rosen ED, Brun R, Hauser S, Adelmant G, Troy AE, McKeon C, Darlington GJ, & Spiegelman BM (1999) Cross-regulation of C/EBP alpha and PPAR gamma controls the transcriptional pathway of adipogenesis and insulin sensitivity. *Mol Cell* 3(2):151-158.
113. Rosen ED, Hsu CH, Wang X, Sakai S, Freeman MW, Gonzalez FJ, & Spiegelman BM (2002) C/EBPalpha induces adipogenesis through PPARgamma: a unified pathway. *Genes Dev* 16(1):22-26.
114. Janderova L, McNeil M, Murrell AN, Mynatt RL, & Smith SR (2003) Human mesenchymal stem cells as an in vitro model for human adipogenesis. *Obes Res* 11(1):65-74.
115. Rodriguez Fernandez JL & Ben-Ze'ev A (1989) Regulation of fibronectin, integrin and cytoskeleton expression in differentiating adipocytes: inhibition by extracellular matrix and polylysine. *Differentiation* 42(2):65-74.
116. Hollister SJ (2005) Porous scaffold design for tissue engineering. *Nat Mater* 4(7):518-524.

117. Hutmacher DW & Cool S (2007) Concepts of scaffold-based tissue engineering--the rationale to use solid free-form fabrication techniques. *J Cell Mol Med* 11(4):654-669.
118. Hutmacher DW (2001) Scaffold design and fabrication technologies for engineering tissues--state of the art and future perspectives. *J Biomater Sci Polym Ed* 12(1):107-124.
119. Dee KC & Bizios R (1996) Mini-review: Proactive biomaterials and bone tissue engineering. *Biotechnology and Bioengineering* 50(4):438-442.
120. Peppas NA & Langer R (1994) New challenges in biomaterials. *Science* 263(5154):1715-1720.
121. Langer R & Tirrell DA (2004) Designing materials for biology and medicine. *Nature* 428(6982):487-492.
122. Anderson DG, Burdick JA, & Langer R (2004) Materials science. Smart biomaterials. *Science* 305(5692):1923-1924.
123. Kohn J (2004) New approaches to biomaterials design. *Nat Mater* 3(11):745-747.
124. Brocchini S (2001) Combinatorial chemistry and biomedical polymer development. *Adv Drug Deliv Rev* 53(1):123-130.
125. Brocchini S, James K, Tangpasuthadol V, & Kohn J (1997) A combinatorial approach for polymer design. *Journal of the American Chemical Society* 119(19):4553-4554.
126. Meier MAR & Schubert US (2006) Selected successful approaches in combinatorial materials research. *Soft Matter* 2(5):371-376.
127. Schubert US & Amis EJ (2004) Combinatorial and High-Throughput Approaches in Polymer and Materials Science: Hype or Real Paradigm Shift? *Macromolecular Rapid Communications* 25(1):19.
128. Becker ML (2006) Combinatorial Biomaterials: opportunitites beyond synthesis. *Biomater Forum* 3:8-11.
129. Meredith JC, Sormana JL, Keselowsky BG, Garcia AJ, Tona A, Karim A, & Amis EJ (2003) Combinatorial characterization of cell interactions with polymer surfaces. *J Biomed Mater Res A* 66(3):483-490.
130. Kennedy SB, Washburn NR, Simon CG, Jr., & Amis EJ (2006) Combinatorial screen of the effect of surface energy on fibronectin-mediated osteoblast adhesion, spreading and proliferation. *Biomaterials* 27(20):3817-3824.
131. Lin NJ, Drzal PL, & Lin-Gibson S (2007) Two-dimensional gradient platforms for rapid assessment of dental polymers: A chemical, mechanical and biological evaluation. *Dent Mater* 23(10):1211-1220.
132. Lin-Gibson S, Landis FA, & Drzal PL (2006) Combinatorial investigation of the structure-properties characterization of photopolymerized dimethacrylate networks. *Biomaterials* 27(9):1711-1717.
133. Simon CG, Jr., Eidelman N, Kennedy SB, Sehgal A, Khatri CA, & Washburn NR (2005) Combinatorial screening of cell proliferation on poly(L-lactic acid)/poly(D,L-lactic acid) blends. *Biomaterials* 26(34):6906-6915.

134. Washburn NR, Yamada KM, Simon CG, Jr., Kennedy SB, & Amis EJ (2004) High-throughput investigation of osteoblast response to polymer crystallinity: influence of nanometer-scale roughness on proliferation. *Biomaterials* 25(7-8):1215-1224.
135. Woodfield TB, Blitterswijk CA, Wijn JD, Sims TJ, Hollander AP, & Riesle J (2005) Polymer Scaffolds Fabricated with Pore-Size Gradients as a Model for Studying the Zonal Organization within Tissue-Engineered Cartilage Constructs. *Tissue Eng* 11(9-10):1297-1311.
136. Zapata P, Su J, Garcia AJ, & Meredith JC (2007) Quantitative High-Throughput Screening of Osteoblast Attachment, Spreading, and Proliferation on Demixed Polymer Blend Micropatterns. *Biomacromolecules*.
137. Anderson DG, Putnam D, Lavik EB, Mahmood TA, & Langer R (2005) Biomaterial microarrays: rapid, microscale screening of polymer-cell interaction. *Biomaterials* 26(23):4892-4897.
138. Abramson SD, Alexe G, Hammer PL, & Kohn J (2005) A computational approach to predicting cell growth on polymeric biomaterials. *J Biomed Mater Res A* 73(1):116-124.
139. Dobkowski J, Kolos R, Kaminski J, & Kowalczyńska HM (1999) Cell adhesion to polymeric surfaces: Experimental study and simple theoretical approach. *Journal of Biomedical Materials Research* 47(2):234-242.
140. Kholodovych V, Smith JR, Knight D, Abramson S, Kohn J, & Welsh WJ (2004) Accurate predictions of cellular response using QSPR: a feasibility test of rational design of polymeric biomaterials. *Polymer* 45(22):7367-7379.
141. Smith JR, Kholodovych V, Knight D, Kohn J, & Welsh WJ (2005) Predicting fibrinogen adsorption to polymeric surfaces in silico: a combined method approach. *Polymer* 46(12):4296-4306.
142. Smith JR, Kholodovych V, Knight D, Welsh WJ, & Kohn J (2005) QSAR models for the analysis of bioresponse data from combinatorial libraries of biomaterials. *Qsar & Combinatorial Science* 24(1):99-113.
143. Smith JR, Knight D, Kohn J, Rasheed K, Weber N, Kholodovych V, & Welsh WJ (2004) Using surrogate modeling in the prediction of fibrinogen adsorption onto polymer surfaces. *Journal of Chemical Information and Computer Sciences* 44(3):1088-1097.
144. Smith JR, Seyda A, Weber N, Knight D, Abramson S, & Kohn J (2004) Integration of combinatorial synthesis, rapid screening, and computational modeling in biomaterials development. *Macromolecular Rapid Communications* 25(1):127-140.
145. Gubskaya AV, Kholodovych V, Knight D, Kohn J, & Welsh WJ (2007) Prediction of fibrinogen adsorption for biodegradable polymers: Integration of molecular dynamics and surrogate modeling. *Polymer* 48(19):5788-5801.
146. Kholodovych V, Gubskaya AV, Bohrer M, Harris N, Knight D, Kohn J, & Welsh WJ (2008) Prediction of biological response for large combinatorial

- libraries of biodegradable polymers: Polymethacrylates as a test case. *Polymer* 49(10):2435-2439.
147. Kohn J, Smith JR, Seyda A, Weber N, Abramson S, & Knight D (2004) Combinatorial synthesis, rapid screening, and computational modeling in biomaterials development. *Abstracts of Papers of the American Chemical Society* 227:U557-U557.
 148. Holmes PF, Bohrer M, & Kohn J (2008) Exploration of polymethacrylate structure-property correlations: Advances towards combinatorial and high-throughput methods for biomaterials discovery. *Prog Polym Sci* 33(8):787-796.
 149. Schmatloch S, Meier MAR, & Schubert US (2003) Instrumentation for Combinatorial and High-Throughput Polymer Research: A Short Overview. *Macromolecular Rapid Communications* 24(1):33-46.
 150. Flaim CJ, Chien S, & Bhatia SN (2005) An extracellular matrix microarray for probing cellular differentiation. *Nat Methods* 2(2):119-125.
 151. MacBeath G & Schreiber SL (2000) Printing proteins as microarrays for high-throughput function determination. *Science* 289(5485):1760-1763.
 152. Weber N, Bolikal D, Bourke SL, & Kohn J (2004) Small changes in the polymer structure influence the adsorption behavior of fibrinogen on polymer surfaces: validation of a new rapid screening technique. *J Biomed Mater Res A* 68(3):496-503.
 153. Marie R, Beech JP, Voros J, Tegenfeldt JO, & Hook F (2006) Use of PLL-g-PEG in micro-fluidic devices for localizing selective and specific protein binding. *Langmuir* 22(24):10103-10108.
 154. Anselme K, Bigerelle M, Noel B, Dufresne E, Judas D, Iost A, & Hardouin P (2000) Qualitative and quantitative study of human osteoblast adhesion on materials with various surface roughnesses. *J Biomed Mater Res* 49(2):155-166.
 155. Dadsetan M, Jones JA, Hiltner A, & Anderson JM (2004) Surface chemistry mediates adhesive structure, cytoskeletal organization, and fusion of macrophages. *J Biomed Mater Res A* 71(3):439-448.
 156. Dalby MJ, Riehle MO, Johnstone HJ, Affrossman S, & Curtis AS (2002) Polymer-demixed nanotopography: control of fibroblast spreading and proliferation. *Tissue Eng* 8(6):1099-1108.
 157. Kapur R & Rudolph AS (1998) Cellular and cytoskeleton morphology and strength of adhesion of cells on self-assembled monolayers of organosilanes. *Exp Cell Res* 244(1):275-285.
 158. Kato S, Kidoaki S, & Matsuda T (2004) Substrate-dependent cellular behavior of Swiss 3T3 fibroblasts and activation of Rho family during adhesion and spreading processes. *J Biomed Mater Res A* 68(2):314-324.
 159. Shah AK, Sinha RK, Hickok NJ, & Tuan RS (1999) High-resolution morphometric analysis of human osteoblastic cell adhesion on clinically relevant orthopedic alloys. *Bone* 24(5):499-506.
 160. Abraham VC, Taylor DL, & Haskins JR (2004) High content screening applied to large-scale cell biology. *Trends Biotechnol* 22(1):15-22.

161. Perlman ZE, Slack MD, Feng Y, Mitchison TJ, Wu LF, & Altschuler SJ (2004) Multidimensional drug profiling by automated microscopy. *Science* 306(5699):1194-1198.
162. Price JH, Goodacre A, Hahn K, Hodgson L, Hunter EA, Krajewski S, Murphy RF, Rabinovich A, Reed JC, & Heynen S (2002) Advances in molecular labeling, high throughput imaging and machine intelligence portend powerful functional cellular biochemistry tools. *J Cell Biochem Suppl* 39:194-210.
163. Tanaka M, Bateman R, Rauh D, Vaisberg E, Ramachandani S, Zhang C, Hansen KC, Burlingame AL, Trautman JK, Shokat KM, & Adams CL (2005) An unbiased cell morphology-based screen for new, biologically active small molecules. *PLoS Biol* 3(5):e128.
164. Yi Q & Coppelino MG (2006) Automated classification and quantification of F-actin-containing ruffles in confocal micrographs. *Biotechniques* 40(6):745-746, 748, 750 passim.
165. Halhuber KJ & Konig K (2003) Modern laser scanning microscopy in biology, biotechnology and medicine. *Ann Anat* 185(1):1-20.
166. Paddock SW (2000) Principles and practices of laser scanning confocal microscopy. *Mol Biotechnol* 16(2):127-149.
167. Paddock SW (1999) Confocal laser scanning microscopy. *Biotechniques* 27(5):992-996, 998-1002, 1004.
168. Oheim M, Michael DJ, Geisbauer M, Madsen D, & Chow RH (2006) Principles of two-photon excitation fluorescence microscopy and other nonlinear imaging approaches. *Adv Drug Deliv Rev* 58(7):788-808.
169. Diaspro A, Bianchini P, Vicidomini G, Faretta M, Ramoino P, & Usai C (2006) Multi-photon excitation microscopy. *Biomed Eng Online* 5:36.
170. Ingber DE (1993) Cellular tensegrity: defining new rules of biological design that govern the cytoskeleton. *J Cell Sci* 104 (Pt 3):613-627.
171. Ingber DE (1997) Tensegrity: the architectural basis of cellular mechanotransduction. *Annu Rev Physiol* 59:575-599.
172. Ingber DE (2000) Opposing views on tensegrity as a structural framework for understanding cell mechanics. *J Appl Physiol* 89(4):1663-1670.
173. Ingber DE (2003) Tensegrity I. Cell structure and hierarchical systems biology. *J Cell Sci* 116(Pt 7):1157-1173.
174. Ingber DE (1998) Cellular basis of mechanotransduction. *Biol Bull* 194(3):323-325; discussion 325-327.
175. Choquet D, Felsenfeld DP, & Sheetz MP (1997) Extracellular matrix rigidity causes strengthening of integrin-cytoskeleton linkages. *Cell* 88(1):39-48.
176. Ingber DE (2003) Mechanosensation through integrins: cells act locally but think globally. *Proc Natl Acad Sci U S A* 100(4):1472-1474.
177. Wang N, Butler JP, & Ingber DE (1993) Mechanotransduction across the cell surface and through the cytoskeleton. *Science* 260(5111):1124-1127.
178. Janmey PA (1998) The cytoskeleton and cell signaling: component localization and mechanical coupling. *Physiol Rev* 78(3):763-781.

179. Chen CS, Alonso JL, Ostuni E, Whitesides GM, & Ingber DE (2003) Cell shape provides global control of focal adhesion assembly. *Biochem Biophys Res Commun* 307(2):355-361.
180. Schoenwaelder SM & Burridge K (1999) Bidirectional signaling between the cytoskeleton and integrins. *Curr Opin Cell Biol* 11(2):274-286.
181. Chen CS, Mrksich M, Huang S, Whitesides GM, & Ingber DE (1997) Geometric control of cell life and death. *Science* 276(5317):1425-1428.
182. Huang S & Ingber DE (2002) A discrete cell cycle checkpoint in late G(1) that is cytoskeleton-dependent and MAP kinase (Erk)-independent. *Exp Cell Res* 275(2):255-264.
183. Mammoto A, Huang S, Moore K, Oh P, & Ingber DE (2004) Role of RhoA, mDia, and ROCK in cell shape-dependent control of the Skp2-p27kip1 pathway and the G1/S transition. *J Biol Chem* 279(25):26323-26330.
184. Chen CS, Brangwynne C, & Ingber DE (1999) Pictures in cell biology: squaring up to the cell-shape debate. *Trends Cell Biol* 9(7):283.
185. Huang S, Chen CS, & Ingber DE (1998) Control of cyclin D1, p27(Kip1), and cell cycle progression in human capillary endothelial cells by cell shape and cytoskeletal tension. *Mol Biol Cell* 9(11):3179-3193.
186. Carvalho RS, Schaffer JL, & Gerstenfeld LC (1998) Osteoblasts induce osteopontin expression in response to attachment on fibronectin: demonstration of a common role for integrin receptors in the signal transduction processes of cell attachment and mechanical stimulation. *J Cell Biochem* 70(3):376-390.
187. Solursh M (1989) Extracellular matrix and cell surface as determinants of connective tissue differentiation. *Am J Med Genet* 34(1):30-34.
188. Spiegelman BM & Ginty CA (1983) Fibronectin modulation of cell shape and lipogenic gene expression in 3T3-adipocytes. *Cell* 35(3 Pt 2):657-666.
189. Sordella R, Jiang W, Chen GC, Curto M, & Settleman J (2003) Modulation of Rho GTPase signaling regulates a switch between adipogenesis and myogenesis. *Cell* 113(2):147-158.
190. Jaffe AB & Hall A (2005) Rho GTPases: biochemistry and biology. *Annu Rev Cell Dev Biol* 21:247-269.
191. Hall A (1998) Rho GTPases and the actin cytoskeleton. *Science* 279(5350):509-514.
192. Nobes CD & Hall A (1995) Rho, rac, and cdc42 GTPases regulate the assembly of multimolecular focal complexes associated with actin stress fibers, lamellipodia, and filopodia. *Cell* 81(1):53-62.
193. Ridley AJ & Hall A (1992) The small GTP-binding protein rho regulates the assembly of focal adhesions and actin stress fibers in response to growth factors. *Cell* 70(3):389-399.
194. Ridley AJ, Paterson HF, Johnston CL, Diekmann D, & Hall A (1992) The small GTP-binding protein rac regulates growth factor-induced membrane ruffling. *Cell* 70(3):401-410.
195. Amano M, Ito M, Kimura K, Fukata Y, Chihara K, Nakano T, Matsuura Y, & Kaibuchi K (1996) Phosphorylation and activation of myosin by Rho-associated kinase (Rho-kinase). *J Biol Chem* 271(34):20246-20249.

196. Kawano Y, Fukata Y, Oshiro N, Amano M, Nakamura T, Ito M, Matsumura F, Inagaki M, & Kaibuchi K (1999) Phosphorylation of myosin-binding subunit (MBS) of myosin phosphatase by Rho-kinase in vivo. *J Cell Biol* 147(5):1023-1038.
197. Kimura K, Ito M, Amano M, Chihara K, Fukata Y, Nakafuku M, Yamamori B, Feng J, Nakano T, Okawa K, Iwamatsu A, & Kaibuchi K (1996) Regulation of myosin phosphatase by Rho and Rho-associated kinase (Rho-kinase). *Science* 273(5272):245-248.
198. Anastasiadis PZ, Moon SY, Thoreson MA, Mariner DJ, Crawford HC, Zheng Y, & Reynolds AB (2000) Inhibition of RhoA by p120 catenin. *Nat Cell Biol* 2(9):637-644.
199. Edwards DC, Sanders LC, Bokoch GM, & Gill GN (1999) Activation of LIM-kinase by Pak1 couples Rac/Cdc42 GTPase signalling to actin cytoskeletal dynamics. *Nat Cell Biol* 1(5):253-259.
200. Maekawa M, Ishizaki T, Boku S, Watanabe N, Fujita A, Iwamatsu A, Obinata T, Ohashi K, Mizuno K, & Narumiya S (1999) Signaling from Rho to the actin cytoskeleton through protein kinases ROCK and LIM-kinase. *Science* 285(5429):895-898.
201. Sumi T, Matsumoto K, Takai Y, & Nakamura T (1999) Cofilin phosphorylation and actin cytoskeletal dynamics regulated by rho- and Cdc42-activated LIM-kinase 2. *J Cell Biol* 147(7):1519-1532.
202. Watanabe N, Kato T, Fujita A, Ishizaki T, & Narumiya S (1999) Cooperation between mDia1 and ROCK in Rho-induced actin reorganization. *Nat Cell Biol* 1(3):136-143.
203. Li F & Higgs HN (2003) The mouse Formin mDia1 is a potent actin nucleation factor regulated by autoinhibition. *Curr Biol* 13(15):1335-1340.
204. Gao J, Zoller KE, Ginsberg MH, Brugge JS, & Shattil SJ (1997) Regulation of the pp72syk protein tyrosine kinase by platelet integrin alpha IIb beta 3. *Embo J* 16(21):6414-6425.
205. Ren XD, Kiosses WB, & Schwartz MA (1999) Regulation of the small GTP-binding protein Rho by cell adhesion and the cytoskeleton. *Embo J* 18(3):578-585.
206. Mulzer SR & Brash JL (1990) Analysis of proteins adsorbed to glass from human plasma using immunoblotting methods. *J Biomater Sci Polym Ed* 1(3):173-182.
207. Sigal GB, Bamdad C, Barberis A, Strominger J, & Whitesides GM (1996) A self-assembled monolayer for the binding and study of histidine-tagged proteins by surface plasmon resonance. *Anal Chem* 68(3):490-497.
208. Bhatt AK & Huttenlocher A (2003) Dynamic imaging of cell-substrate contacts. *Methods Enzymol* 361:337-352.
209. Wouters FS, Verveer PJ, & Bastiaens PI (2001) Imaging biochemistry inside cells. *Trends Cell Biol* 11(5):203-211.
210. Hoven VP, Poopattanapong A, & Kohn J (2004) Acid-containing tyrosine-derived polycarbonates: Wettability and surface reactivity. *Macromolecular Symposia* 216(Contributions from 8th Pacific Polymer Conference, 2003):87-97.

211. Macario, Entersz, Bolikal, Kohn, & Nackman (2006) Interaction of endothelial and smooth muscle cells with radiopaque, resorbable polymers. *Journal of Surgical Research* 130(2):267-268.
212. Pulapura S & Kohn J (1992) Tyrosine-derived polycarbonates: backbone-modified "pseudo"-poly(amino acid)s designed for biomedical applications. *Biopolymers* 32(4):411-417.
213. Yu C & Kohn J (1999) Tyrosine-PEG-derived poly(ether carbonate)s as new biomaterials. Part I: synthesis and evaluation. *Biomaterials* 20(3):253-264.
214. Pesnell A (2006) A Focused Library of Tyrosine-derived Polycarbonates for the Discovery of Optimal Polymers for Use in Resorbable Stents. PhD (Rutgers University, Piscataway, NJ).
215. Ertel SI & Kohn J (1994) Evaluation of a series of tyrosine-derived polycarbonates as degradable biomaterials. *J Biomed Mater Res* 28(8):919-930.
216. James K, Levene H, Parsons JR, & Kohn J (1999) Small changes in polymer chemistry have a large effect on the bone-implant interface: evaluation of a series of degradable tyrosine-derived polycarbonates in bone defects. *Biomaterials* 20(23-24):2203-2212.
217. Abramson S, Bolikal D, Levene H, Simon J, & Kohn J (2000) Small changes in polymer structure can dramatically increase degradation rates: The effect of free carboxylate groups on the properties of tyrosine-derived polycarbonates. *Transactions of the Sixth World Biomaterials Congress*, (Society for Biomaterials), p 1164.
218. Tschopp JF, Tolley JO, Malaney T, Mazur C, Bellantoni R, Abramson S, Kohn J, Wang B, & Kemnitzer JE (2000) In vivo resorption profile of matrices from tyrosine-derived polycarbonates with variation in free carboxylate content. *Transactions of the Sixth World Biomaterials Congress*, (Society for Biomaterials), p 1334.
219. Tziampazis E, Kohn J, & Moghe PV (2000) PEG-variant biomaterials as selectively adhesive protein templates: model surfaces for controlled cell adhesion and migration. *Biomaterials* 21(5):511-520.
220. Weber N, Wendel HP, & Kohn J (2005) Formation of viscoelastic protein layers on polymeric surfaces relevant to platelet adhesion. *J Biomed Mater Res A* 72(4):420-427.
221. Edlund M, Lotano MA, & Otey CA (2001) Dynamics of alpha-actinin in focal adhesions and stress fibers visualized with alpha-actinin-green fluorescent protein. *Cell Motil Cytoskeleton* 48(3):190-200.
222. Laukaitis CM, Webb DJ, Donais K, & Horwitz AF (2001) Differential dynamics of alpha 5 integrin, paxillin, and alpha-actinin during formation and disassembly of adhesions in migrating cells. *J Cell Biol* 153(7):1427-1440.
223. Shashidharan P, Chalmers-Redman RM, Carlile GW, Rodic V, Gurvich N, Yuen T, Tatton WG, & Sealfon SC (1999) Nuclear translocation of GAPDH-GFP fusion protein during apoptosis. *Neuroreport* 10(5):1149-1153.

224. Sung HJ, Eskin SG, Sakurai Y, Yee A, Kataoka N, & McIntire LV (2005) Oxidative stress produced with cell migration increases synthetic phenotype of vascular smooth muscle cells. *Ann Biomed Eng* 33(11):1546-1554.
225. Dastoor Z & Dreyer JL (2001) Potential role of nuclear translocation of glyceraldehyde-3-phosphate dehydrogenase in apoptosis and oxidative stress. *J Cell Sci* 114(Pt 9):1643-1653.
226. Lin CW, Jao CY, & Ting AY (2004) Genetically encoded fluorescent reporters of histone methylation in living cells. *J Am Chem Soc* 126(19):5982-5983.
227. Miyawaki A (2003) Visualization of the spatial and temporal dynamics of intracellular signaling. *Dev Cell* 4(3):295-305.
228. Ting AY, Kain KH, Klemke RL, & Tsien RY (2001) Genetically encoded fluorescent reporters of protein tyrosine kinase activities in living cells. *Proc Natl Acad Sci U S A* 98(26):15003-15008.
229. Kozubek S, Lukasova E, Amrichova J, Kozubek M, Liskova A, & Slotova J (2000) Influence of cell fixation on chromatin topography. *Anal Biochem* 282(1):29-38.
230. Martin RM, Leonhardt H, & Cardoso MC (2005) DNA labeling in living cells. *Cytometry A* 67(1):45-52.
231. Riederer BM, Porchet R, Marugg RA, & Binder LI (1993) Solubility of cytoskeletal proteins in immunohistochemistry and the influence of fixation. *J Histochem Cytochem* 41(4):609-616.
232. Shrivastava A, Tiwari M, Sinha RA, Kumar A, Balapure AK, Bajpai VK, Sharma R, Mitra K, Tandon A, & Godbole MM (2006) Molecular iodine induces caspase-independent apoptosis in human breast carcinoma cells involving the mitochondria-mediated pathway. *J Biol Chem* 281(28):19762-19771.
233. Vitale M, Di Matola T, D'Ascoli F, Salzano S, Bogazzi F, Fenzi G, Martino E, & Rossi G (2000) Iodide excess induces apoptosis in thyroid cells through a p53-independent mechanism involving oxidative stress. *Endocrinology* 141(2):598-605.
234. Chang EJ, Kim HH, Huh JE, Kim IA, Seung Ko J, Chung CP, & Kim HM (2005) Low proliferation and high apoptosis of osteoblastic cells on hydrophobic surface are associated with defective Ras signaling. *Exp Cell Res* 303(1):197-206.
235. Weber N, Pesnell A, Bolikal D, Zeltinger J, & Kohn J (2007) Viscoelastic Properties of Fibrinogen Adsorbed to the Surface of Biomaterials Used in Blood-Contacting Medical Devices. *Langmuir*.
236. Stevens MM & George JH (2005) Exploring and engineering the cell surface interface. *Science* 310(5751):1135-1138.
237. Ratner BD & Bryant SJ (2004) Biomaterials: where we have been and where we are going. *Annu Rev Biomed Eng* 6:41-75.
238. Charest JL, Eliason MT, Garcia AJ, & King WP (2006) Combined microscale mechanical topography and chemical patterns on polymer cell culture substrates. *Biomaterials* 27(11):2487-2494.

239. Liu E, Treiser MD, Johnson PA, Patel P, Rege A, Kohn J, & Moghe PV (2007) Quantitative biorelevant profiling of material microstructure within 3D porous scaffolds via multiphoton fluorescence microscopy. *J Biomed Mater Res B Appl Biomater*.
240. Brocchini S, James K, Tangpasuthadol V, & Kohn J (1998) Structure-property correlations in a combinatorial library of degradable biomaterials. *Journal of Biomedical Materials Research* 42(1):66-75.
241. Sung HJ, Su J, Berglund JD, Russ BV, Meredith JC, & Galis ZS (2005) The use of temperature-composition combinatorial libraries to study the effects of biodegradable polymer blend surfaces on vascular cells. *Biomaterials* 26(22):4557-4567.
242. Bailey LO, Becker ML, Stephens JS, Gallant ND, Mahoney CM, Washburn NR, Rege A, Kohn J, & Amis EJ (2006) Cellular response to phase-separated blends of tyrosine-derived polycarbonates. *J Biomed Mater Res A* 76(3):491-502.
243. Zapata P, Su J, Garcia AJ, & Meredith JC (2007) Quantitative high-throughput screening of osteoblast attachment, spreading, and proliferation on demixed polymer blend micropatterns. *Biomacromolecules* 8(6):1907-1917.
244. Meredith JC, Smith AP, Karim A, & Amis EJ (2000) Combinatorial Materials Science for Polymer Thin-Film Dewetting. *Macromolecules* 33(26):9747-9756.
245. Treiser MD, Liu E, Dubin RA, Sung HJ, Kohn J, & Moghe PV (2007) Profiling cell-biomaterial interactions via cell-based fluororeporter imaging. *BioTechniques* 43(3):361-368.
246. Stafford CM, Roskov KE, Epps TH, Iii, & Fasolka MJ (2006) Generating thickness gradients of thin polymer films via flow coating. *Review of Scientific Instruments* 77(2):023908-023907.
247. Ranucci CS & Moghe PV (2001) Substrate microtopography can enhance cell adhesive and migratory responsiveness to matrix ligand density. *J Biomed Mater Res* 54(2):149-161.
248. Chan CM, Ko TM, & Hiraoka H (1996) Polymer surface modification by plasmas and photons. *Surface Science Reports* 24(1/2):1-54.
249. Murthy NS, Prabhu RD, Martin JJ, Zhou L, & Headrick RL (2006) Self-assembled and etched cones on laser ablated polymer surfaces. *Journal of Applied Physics* 100(2):023538/023531-023538/023512.
250. Marletta G, Ciapetti G, Satriano C, Perut F, Salerno M, & Baldini N (2007) Improved osteogenic differentiation of human marrow stromal cells cultured on ion-induced chemically structured poly-epsilon-caprolactone. *Biomaterials* 28(6):1132-1140.
251. Wilson CJ, Clegg RE, Leavesley DI, & Pearcy MJ (2005) Mediation of biomaterial-cell interactions by adsorbed proteins: a review. *Tissue Eng* 11(1-2):1-18.
252. Ryan PL, Foty RA, Kohn J, & Steinberg MS (2001) Tissue spreading on implantable substrates is a competitive outcome of cell-cell vs. cell-substratum adhesivity. *Proc Natl Acad Sci U S A* 98(8):4323-4327.

253. Deng Y, Lin XS, Zheng Z, Deng JG, Chen JC, Ma H, & Chen GQ (2003) Poly(hydroxybutyrate-co-hydroxyhexanoate) promoted production of extracellular matrix of articular cartilage chondrocytes in vitro. *Biomaterials* 24(23):4273-4281.
254. Wang YW, Wu Q, & Chen GQ (2004) Attachment, proliferation and differentiation of osteoblasts on random biopolyester poly(3-hydroxybutyrate-co-3-hydroxyhexanoate) scaffolds. *Biomaterials* 25(4):669-675.
255. Foster R, Hu KQ, Lu Y, Nolan KM, Thissen J, & Settleman J (1996) Identification of a novel human Rho protein with unusual properties: GTPase deficiency and in vivo farnesylation. *Mol Cell Biol* 16(6):2689-2699.
256. Prendergast GC, Davide JP, deSolms SJ, Giuliani EA, Graham SL, Gibbs JB, Oliff A, & Kohl NE (1994) Farnesyltransferase inhibition causes morphological reversion of ras-transformed cells by a complex mechanism that involves regulation of the actin cytoskeleton. *Mol Cell Biol* 14(6):4193-4202.
257. Griffith LG (2000) Polymeric Biomaterials. *Acta Materialia* (48):263-277.
258. Bae YH, Johnson PA, Florek CA, Kohn J, & Moghe PV (2006) Minute changes in composition of polymer substrates produce amplified differences in cell adhesion and motility via optimal ligand conditioning. *Acta Biomater* 2(5):473-482.
259. Thery M, Pepin A, Dressaire E, Chen Y, & Bornens M (2006) Cell distribution of stress fibres in response to the geometry of the adhesive environment. *Cell Motil Cytoskeleton* 63(6):341-355.
260. Juliano RL (2002) Signal transduction by cell adhesion receptors and the cytoskeleton: functions of integrins, cadherins, selectins, and immunoglobulin-superfamily members. *Annu Rev Pharmacol Toxicol* 42:283-323.
261. Balaban NQ, Schwarz US, Riveline D, Goichberg P, Tzur G, Sabanay I, Mahalu D, Safran S, Bershadsky A, Addadi L, & Geiger B (2001) Force and focal adhesion assembly: a close relationship studied using elastic micropatterned substrates. *Nat Cell Biol* 3(5):466-472.
262. Chen J, Fabry B, Schiffrin EL, & Wang N (2001) Twisting integrin receptors increases endothelin-1 gene expression in endothelial cells. *Am J Physiol Cell Physiol* 280(6):C1475-1484.
263. Meyer CJ, Alenghat FJ, Rim P, Fong JH, Fabry B, & Ingber DE (2000) Mechanical control of cyclic AMP signalling and gene transcription through integrins. *Nat Cell Biol* 2(9):666-668.
264. Riveline D, Zamir E, Balaban NQ, Schwarz US, Ishizaki T, Narumiya S, Kam Z, Geiger B, & Bershadsky AD (2001) Focal contacts as mechanosensors: externally applied local mechanical force induces growth of focal contacts by an mDia1-dependent and ROCK-independent mechanism. *J Cell Biol* 153(6):1175-1186.
265. Burridge K & Chrzanowska-Wodnicka M (1996) Focal adhesions, contractility, and signaling. *Annu Rev Cell Dev Biol* 12:463-518.

266. Attawia MA, Devin JE, & Laurencin CT (1995) Immunofluorescence and confocal laser scanning microscopy studies of osteoblast growth and phenotypic expression in three-dimensional degradable synthetic matrices. *J Biomed Mater Res* 29(7):843-848.
267. Semler EJ, Tjia JS, & Moghe PV (1997) Analysis of surface microtopography of biodegradable polymer matrices using confocal reflection microscopy. *Biotechnol Prog* 13(5):630-634.
268. Treiser MD, Liu E, Dubin RA, Sung HJ, Kohn J, & Moghe PV (2007) Profiling cell-biomaterial interactions via cell-based fluororeporter imaging. *Biotechniques* 43(3):361-366, 368.
269. Kohn J, Bolikal D, & Pendharkar SM (2002) Patent assigned to: Rutgers, The State University 6475477.
270. Bourke SL & Kohn J (2003) Polymers derived from the amino acid L-tyrosine: polycarbonates, polyarylates and copolymers with poly(ethylene glycol). *Adv Drug Deliv Rev* 55(4):447-466.
271. Breiman L, Friedman JH, Olshen RA, & Stone CJ (1984) *Classification and Regression Trees* (Wadsworth Inc., Belmont, California); Classification and Regression Trees p 341.
272. Murthy SK (1998) Automatic Construction of Decision Trees from Data: A Multi-Disciplinary Survey. *Data Mining and Knowledge Discovery* 2(4):345-389.
273. Gibb WJ, Auslander DM, & Griffin JC (1993) Selection of myocardial electrogram features for use by implantable devices. *IEEE Trans Biomed Eng* 40(8):727-735.
274. Long WJ, Griffith JL, Selker HP, & D'Agostino RB (1993) A comparison of logistic regression to decision-tree induction in a medical domain. *Comput Biomed Res* 26(1):74-97.
275. Hautaniemi S, Kharait S, Iwabu A, Wells A, & Lauffenburger DA (2005) Modeling of signal-response cascades using decision tree analysis. *Bioinformatics* 21(9):2027-2035.
276. Anderson JA & Rosenfeld E (1988) *Neurocomputing: Foundations of Research* (MIT Press, Cambridge); Neurocomputing: Foundations of Research.
277. McCulloch JL & Pitts W (1943) A Logical Calculus of Ideas Immanent in Nervous Activity. *Bulletin of Mathematical Biophysics* 5:115-133.
278. Abdi H (1994) A Neural Network Primer. *Journal of Biological Systems* 2(3):247-283.
279. Hertz J, Krogh A, & Palmer RG (1991) *Introduction to the theory of neural computation* (Allan M. Wylde, Redwood City, CA); Introduction to the theory of neural computation.
280. Chilkoti A, Schmierer AE, Perez-Luna VH, & Ratner BD (1995) Investigating the relationship between surface chemistry and endothelial cell growth: partial least-squares regression of the static secondary ion mass spectra of oxygen-containing plasma-deposited films. *Anal Chem* 67(17):2883-2891.

281. Perez-Luna VH, Horbett TA, & Ratner BD (1994) Developing correlations between fibrinogen adsorption and surface properties using multivariate statistics. Student Research Award in the Doctoral Degree Candidate Category, 20th annual meeting of the Society for Biomaterials, Boston, MA, April 5-9, 1994. *J Biomed Mater Res* 28(10):1111-1126.
282. Wagner MS, Shen M, Horbett TA, & Castner DG (2003) Quantitative analysis of binary adsorbed protein films by time of flight secondary ion mass spectrometry. *J Biomed Mater Res A* 64(1):1-11.
283. Witten IH & Eibe F (2005) *Data Mining: Practical machine learning tools and techniques* (Morgan Kaufmann, San Francisco); Data Mining: Practical machine learning tools and techniques 2nd Ed.
284. Rodan SB, Imai Y, Thiede MA, Wesolowski G, Thompson D, Bar-Shavit Z, Shull S, Mann K, & Rodan GA (1987) Characterization of a human osteosarcoma cell line (Saos-2) with osteoblastic properties. *Cancer Res* 47(18):4961-4966.
285. Okumura A, Goto M, Goto T, Yoshinari M, Masuko S, Katsuki T, & Tanaka T (2001) Substrate affects the initial attachment and subsequent behavior of human osteoblastic cells (Saos-2). *Biomaterials* 22(16):2263-2271.
286. Wang C, Duan Y, Markovic B, Barbara J, Rolfe Howlett C, Zhang X, & Zreiqat H (2004) Proliferation and bone-related gene expression of osteoblasts grown on hydroxyapatite ceramics sintered at different temperature. *Biomaterials* 25(15):2949-2956.
287. Alcaide M, Serrano MC, Pagani R, Sanchez-Salcedo S, Nieto A, Vallet-Regi M, & Portoles MT (2009) L929 fibroblast and Saos-2 osteoblast response to hydroxyapatite-betaTCP/agarose biomaterial. *J Biomed Mater Res A* 89(2):539-549.
288. Fassina L, Visai L, Asti L, Benazzo F, Speziale P, Tanzi MC, & Magenes G (2005) Calcified matrix production by SAOS-2 cells inside a polyurethane porous scaffold, using a perfusion bioreactor. *Tissue Eng* 11(5-6):685-700.
289. Geckeler K, Wacker R, Martini F, Hack A, & Aicher W (2003) Enhanced biocompatibility for SAOS-2 osteosarcoma cells by surface coating with hydrophobic epoxy resins. *Cell Physiol Biochem* 13(3):155-164.
290. Tuzlakoglu K, Bolgen N, Salgado AJ, Gomes ME, Piskin E, & Reis RL (2005) Nano- and micro-fiber combined scaffolds: a new architecture for bone tissue engineering. *J Mater Sci Mater Med* 16(12):1099-1104.
291. Webb K, Hlady V, & Tresco PA (2000) Relationships among cell attachment, spreading, cytoskeletal organization, and migration rate for anchorage-dependent cells on model surfaces. *J Biomed Mater Res* 49(3):362-368.
292. Ciapetti G, Cenni E, Pratelli L, & Pizzoferrato A (1993) In vitro evaluation of cell/biomaterial interaction by MTT assay. *Biomaterials* 14(5):359-364.
293. Mayr-Wohlfart U, Fiedler J, Gunther KP, Puhl W, & Kessler S (2001) Proliferation and differentiation rates of a human osteoblast-like cell line (SaOS-2) in contact with different bone substitute materials. *J Biomed Mater Res* 57(1):132-139.

294. Keselowsky BG, Byers BA, & Garcia AJ (1999) Modulation of osteoblastic phenotype by substrate-dependent changes in fibronectin conformation. *21st Annual Conf. and the 1999 Annual Fall Meeting of the Biomedical Engineering Soc.*, p 113.
295. Rezanian A & Healy KE (2000) The effect of peptide surface density on mineralization of a matrix deposited by osteogenic cells. *J Biomed Mater Res* 52(4):595-600.
296. Kohn J, Bolikal D, Pesnell A, Zeltinger J, Brandom DK, & Schmid E (2006) Patent assigned to: Rutgers, The State University, USA 2004-952202, 2006034769.
297. Macario DK, Entersz I, Bolikal D, Kohn J, & Nackman GB (2008) Iodine inhibits antiadhesive effect of PEG: implications for tissue engineering. *J Biomed Mater Res B Appl Biomater* 86(1):237-244.
298. Healy KE, Thomas CH, Rezanian A, Kim JE, McKeown PJ, Lom B, & Hockberger PE (1996) Kinetics of bone cell organization and mineralization on materials with patterned surface chemistry. *Biomaterials* 17(2):195-208.
299. Tan J, Gemeinhart RA, Ma M, & Saltzman WM (2005) Improved cell adhesion and proliferation on synthetic phosphonic acid-containing hydrogels. *Biomaterials* 26(17):3663-3671.
300. Sung HJ, Chandra P, Treiser MD, Liu E, Iovine CP, Moghe PV, & Kohn J (2009) Synthetic polymeric substrates as potent pro-oxidant versus anti-oxidant regulators of cytoskeletal remodeling and cell apoptosis. *J Cell Physiol* 218(3):549-557.
301. Manolagas SC (2000) Birth and death of bone cells: basic regulatory mechanisms and implications for the pathogenesis and treatment of osteoporosis. *Endocr Rev* 21(2):115-137.
302. Calvert JW, Marra KG, Cook L, Kumta PN, DiMilla PA, & Weiss LE (2000) Characterization of osteoblast-like behavior of cultured bone marrow stromal cells on various polymer surfaces. *Journal of Biomedical Materials Research* 52(2):279-284.
303. Harbers GM & Healy KE (2005) The effect of ligand type and density on osteoblast adhesion, proliferation, and matrix mineralization. *J Biomed Mater Res A*.
304. Jansen EJ, Sladek RE, Bahar H, Yaffe A, Gijbels MJ, Kuijter R, Bulstra SK, Guldemond NA, Binderman I, & Koole LH (2005) Hydrophobicity as a design criterion for polymer scaffolds in bone tissue engineering. *Biomaterials* 26(21):4423-4431.
305. Song J, Malathong V, & Bertozzi CR (2005) Mineralization of synthetic polymer scaffolds: a bottom-up approach for the development of artificial bone. *J Am Chem Soc* 127(10):3366-3372.
306. Rodriguez JP, Gonzalez M, Rios S, & Cambiasso V (2004) Cytoskeletal organization of human mesenchymal stem cells (MSC) changes during their osteogenic differentiation. *J Cell Biochem* 93(4):721-731.
307. Hausser HJ & Brenner RE (2005) Phenotypic instability of Saos-2 cells in long-term culture. *Biochem Biophys Res Commun* 333(1):216-222.

308. Boyan BD, Hummert TW, Dean DD, & Schwartz Z (1996) Role of material surfaces in regulating bone and cartilage cell response. *Biomaterials* 17(2):137-146.
309. Huang S & Ingber DE (1999) The structural and mechanical complexity of cell-growth control. *Nat Cell Biol* 1(5):E131-138.
310. Levene HB (1999) Analysis of Tyrosine-Derived Novel Synthetic Polymer Scaffold Devices for Guided Tissue Regeneration. Ph.D. (Rutgers, The State University of New Jersey, The Graduate School of Biomedical Sciences of the University of Medicine and Dentistry of New Jersey, Piscataway).
311. Park IH, Zhao R, West JA, Yabuuchi A, Huo H, Ince TA, Lerou PH, Lensch MW, & Daley GQ (2008) Reprogramming of human somatic cells to pluripotency with defined factors. *Nature* 451(7175):141-146.
312. Takahashi K, Tanabe K, Ohnuki M, Narita M, Ichisaka T, Tomoda K, & Yamanaka S (2007) Induction of pluripotent stem cells from adult human fibroblasts by defined factors. *Cell* 131(5):861-872.
313. Yu J, Vodyanik MA, Smuga-Otto K, Antosiewicz-Bourget J, Frane JL, Tian S, Nie J, Jonsdottir GA, Ruotti V, Stewart R, Slukvin, II, & Thomson JA (2007) Induced pluripotent stem cell lines derived from human somatic cells. *Science* 318(5858):1917-1920.
314. Bianco P & Robey PG (2001) Stem cells in tissue engineering. *Nature* 414(6859):118-121.
315. Curran JM, Chen R, & Hunt JA (2006) The guidance of human mesenchymal stem cell differentiation in vitro by controlled modifications to the cell substrate. *Biomaterials* 27(27):4783-4793.
316. Wakitani S, Saito T, & Caplan AI (1995) Myogenic cells derived from rat bone marrow mesenchymal stem cells exposed to 5-azacytidine. *Muscle Nerve* 18(12):1417-1426.
317. Gang EJ, Jeong JA, Hong SH, Hwang SH, Kim SW, Yang IH, Ahn C, Han H, & Kim H (2004) Skeletal myogenic differentiation of mesenchymal stem cells isolated from human umbilical cord blood. *Stem Cells* 22(4):617-624.
318. Baksh D, Song L, & Tuan RS (2004) Adult mesenchymal stem cells: characterization, differentiation, and application in cell and gene therapy. *J Cell Mol Med* 8(3):301-316.
319. Kulterer B, Friedl G, Jandrositz A, Sanchez-Cabo F, Prokesch A, Paar C, Scheideler M, Windhager R, Preisegger KH, & Trajanoski Z (2007) Gene expression profiling of human mesenchymal stem cells derived from bone marrow during expansion and osteoblast differentiation. *BMC Genomics* 8:70.
320. Olson AC, Larson NM, & Heckman CA (1980) Classification of cultured mammalian cells by shape analysis and pattern recognition. *Proc Natl Acad Sci U S A* 77(3):1516-1520.
321. Mangoubi K, Jeffreys C, Copeland A, Desai M, & Sammak P (2007) Non-Invasive Image Based Support Vector Machine Classification of Human Embryonic Stem Cells. *Biomedical Imaging: From Nano to Macro, 2007. ISBI 2007. 4th IEEE International Symposium*, pp 284-287.

322. Pockwinse SM, Stein JL, Lian JB, & Stein GS (1995) Developmental stage-specific cellular responses to vitamin D and glucocorticoids during differentiation of the osteoblast phenotype: interrelationship of morphology and gene expression by in situ hybridization. *Exp Cell Res* 216(1):244-260.
323. Sikavitsas VI, Temenoff JS, & Mikos AG (2001) Biomaterials and bone mechanotransduction. *Biomaterials* 22(19):2581-2593.
324. Thomas CH, Collier JH, Sfeir CS, & Healy KE (2002) Engineering gene expression and protein synthesis by modulation of nuclear shape. *Proc Natl Acad Sci U S A* 99(4):1972-1977.
325. Taguchi YH & Oono Y (2005) Relational patterns of gene expression via non-metric multidimensional scaling analysis. *Bioinformatics* 21(6):730-740.
326. Cox TF & Cox MAA (2001) *Multidimensional scaling* (Chapman & Hall/CRC, Boca Raton); Multidimensional scaling 2nd Ed pp xi, 308 p.
327. Cortes C & Vapnik V (1995) Support-vector networks. *Machine Learning* 20(3):273-297.
328. Briggs T, Treiser MD, Holmes PF, Kohn J, Moghe PV, & Arinzeh TL (2008) Osteogenic differentiation of human mesenchymal stem cells on poly(ethylene glycol)-variant biomaterials. *J Biomed Mater Res A*.
329. Hung SC, Chang CF, Ma HL, Chen TH, & Low-Tone Ho L (2004) Gene expression profiles of early adipogenesis in human mesenchymal stem cells. *Gene* 340(1):141-150.
330. Sekiya I, Larson BL, Smith JR, Pochampally R, Cui JG, & Prockop DJ (2002) Expansion of human adult stem cells from bone marrow stroma: conditions that maximize the yields of early progenitors and evaluate their quality. *Stem Cells* 20(6):530-541.
331. Bruder SP, Jaiswal N, & Haynesworth SE (1997) Growth kinetics, self-renewal, and the osteogenic potential of purified human mesenchymal stem cells during extensive subcultivation and following cryopreservation. *J Cell Biochem* 64(2):278-294.
332. Jaishankar A & Vrana KE (2009) Emerging molecular approaches in stem cell biology. *Biotechniques Special Issue* 46(5):367-371.
333. Yanaka N, Imai Y, Kawai E, Akatsuka H, Wakimoto K, Nogusa Y, Kato N, Chiba H, Kotani E, Omori K, & Sakurai N (2003) Novel membrane protein containing glycerophosphodiester phosphodiesterase motif is transiently expressed during osteoblast differentiation. *J Biol Chem* 278(44):43595-43602.
334. Kustermans G, Piette J, & Legrand-Poels S (2008) Actin-targeting natural compounds as tools to study the role of actin cytoskeleton in signal transduction. *Biochem Pharmacol* 76(11):1310-1322.
335. Nemeth ZH, Deitch EA, Davidson MT, Szabo C, Vizi ES, & Hasko G (2004) Disruption of the actin cytoskeleton results in nuclear factor-kappaB activation and inflammatory mediator production in cultured human intestinal epithelial cells. *J Cell Physiol* 200(1):71-81.

336. Rodriguez-Viciana P, Warne PH, Khwaja A, Marte BM, Pappin D, Das P, Waterfield MD, Ridley A, & Downward J (1997) Role of phosphoinositide 3-OH kinase in cell transformation and control of the actin cytoskeleton by Ras. *Cell* 89(3):457-467.
337. Rivas FV, O'Keefe JP, Alegre ML, & Gajewski TF (2004) Actin cytoskeleton regulates calcium dynamics and NFAT nuclear duration. *Mol Cell Biol* 24(4):1628-1639.
338. Kukalev A, Nord Y, Palmberg C, Bergman T, & Percipalle P (2005) Actin and hnRNP U cooperate for productive transcription by RNA polymerase II. *Nat Struct Mol Biol* 12(3):238-244.
339. McBride SH & Knothe Tate ML (2008) Modulation of stem cell shape and fate A: the role of density and seeding protocol on nucleus shape and gene expression. *Tissue Eng Part A* 14(9):1561-1572.
340. Schneider RK, Neuss S, Stainforth R, Laddach N, Bovi M, Knuechel R, & Perez-Bouza A (2008) Three-dimensional epidermis-like growth of human mesenchymal stem cells on dermal equivalents: contribution to tissue organization by adaptation of myofibroblastic phenotype and function. *Differentiation* 76(2):156-167.
341. Woodbury D, Schwarz EJ, Prockop DJ, & Black IB (2000) Adult rat and human bone marrow stromal cells differentiate into neurons. *J Neurosci Res* 61(4):364-370.
342. Xu W, Zhang X, Qian H, Zhu W, Sun X, Hu J, Zhou H, & Chen Y (2004) Mesenchymal stem cells from adult human bone marrow differentiate into a cardiomyocyte phenotype in vitro. *Exp Biol Med (Maywood)* 229(7):623-631.
343. Toma C, Pittenger MF, Cahill KS, Byrne BJ, & Kessler PD (2002) Human mesenchymal stem cells differentiate to a cardiomyocyte phenotype in the adult murine heart. *Circulation* 105(1):93-98.
344. Harmey D, Stenbeck G, Nobes CD, Lax AJ, & Grigoriadis AE (2004) Regulation of osteoblast differentiation by *Pasteurella multocida* toxin (PMT): a role for Rho GTPase in bone formation. *J Bone Miner Res* 19(4):661-670.
345. Settleman J (2004) Tension precedes commitment-even for a stem cell. *Mol Cell* 14(2):148-150.
346. Hofmann WA, Stojiljkovic L, Fuchsova B, Vargas GM, Mavrommatis E, Philimonenko V, Kysela K, Goodrich JA, Lessard JL, Hope TJ, Hozak P, & de Lanerolle P (2004) Actin is part of pre-initiation complexes and is necessary for transcription by RNA polymerase II. *Nat Cell Biol* 6(11):1094-1101.
347. Uebersax L, Hagenmuller H, Hofmann S, Gruenblatt E, Muller R, Vunjak-Novakovic G, Kaplan DL, Merkle HP, & Meinel L (2006) Effect of scaffold design on bone morphology in vitro. *Tissue Eng* 12(12):3417-3429.
348. Rentsch C, Rentsch B, Breier A, Hofmann A, Manthey S, Scharnweber D, Biewener A, & Zwipp H (2009) Evaluation of the osteogenic potential and vascularization of 3D poly(3)hydroxybutyrate scaffolds subcutaneously implanted in nude rats. *J Biomed Mater Res A*.

349. Neuss S, Stainforth R, Salber J, Schenck P, Bovi M, Knuchel R, & Perez-Bouza A (2008) Long-term survival and bipotent terminal differentiation of human mesenchymal stem cells (hMSC) in combination with a commercially available three-dimensional collagen scaffold. *Cell Transplant* 17(8):977-986.
350. Xin X, Hussain M, & Mao JJ (2007) Continuing differentiation of human mesenchymal stem cells and induced chondrogenic and osteogenic lineages in electrospun PLGA nanofiber scaffold. *Biomaterials* 28(2):316-325.
351. Wang Y, Kim UJ, Blasioli DJ, Kim HJ, & Kaplan DL (2005) In vitro cartilage tissue engineering with 3D porous aqueous-derived silk scaffolds and mesenchymal stem cells. *Biomaterials* 26(34):7082-7094.
352. Wozniak MA, Modzelewska K, Kwong L, & Keely PJ (2004) Focal adhesion regulation of cell behavior. *Biochim Biophys Acta* 1692(2-3):103-119.
353. Docheva D, Popov C, Mutschler W, & Schieker M (2007) Human mesenchymal stem cells in contact with their environment: surface characteristics and the integrin system. *J Cell Mol Med* 11(1):21-38.
354. Cukierman E, Pankov R, Stevens DR, & Yamada KM (2001) Taking cell-matrix adhesions to the third dimension. *Science* 294(5547):1708-1712.
355. Hishikawa K, Miura S, Marumo T, Yoshioka H, Mori Y, Takato T, & Fujita T (2004) Gene expression profile of human mesenchymal stem cells during osteogenesis in three-dimensional thermoreversible gelation polymer. *Biochem Biophys Res Commun* 317(4):1103-1107.
356. Li WJ, Tuli R, Huang X, Laquerriere P, & Tuan RS (2005) Multilineage differentiation of human mesenchymal stem cells in a three-dimensional nanofibrous scaffold. *Biomaterials* 26(25):5158-5166.
357. Hanks SK, Calalb MB, Harper MC, & Patel SK (1992) Focal adhesion protein-tyrosine kinase phosphorylated in response to cell attachment to fibronectin. *Proc Natl Acad Sci U S A* 89(18):8487-8491.
358. Schaller MD, Borgman CA, Cobb BS, Vines RR, Reynolds AB, & Parsons JT (1992) pp125FAK a structurally distinctive protein-tyrosine kinase associated with focal adhesions. *Proc Natl Acad Sci U S A* 89(11):5192-5196.
359. Assoian RK (1997) Anchorage-dependent cell cycle progression. *J Cell Biol* 136(1):1-4.
360. Cary LA & Guan JL (1999) Focal adhesion kinase in integrin-mediated signaling. *Front Biosci* 4:D102-113.
361. Lauffenburger DA & Horwitz AF (1996) Cell migration: a physically integrated molecular process. *Cell* 84(3):359-369.
362. Pirone DM, Liu WF, Ruiz SA, Gao L, Raghavan S, Lemmon CA, Romer LH, & Chen CS (2006) An inhibitory role for FAK in regulating proliferation: a link between limited adhesion and RhoA-ROCK signaling. *J Cell Biol* 174(2):277-288.
363. Ruoslahti E & Reed JC (1994) Anchorage dependence, integrins, and apoptosis. *Cell* 77(4):477-478.

- 364. Howe A, Aplin AE, Alahari SK, & Juliano RL (1998) Integrin signaling and cell growth control. *Curr Opin Cell Biol* 10(2):220-231.
- 365. Lin TH, Aplin AE, Shen Y, Chen Q, Schaller M, Romer L, Aukhil I, & Juliano RL (1997) Integrin-mediated activation of MAP kinase is independent of FAK: evidence for dual integrin signaling pathways in fibroblasts. *J Cell Biol* 136(6):1385-1395.
- 366. Ridley AJ, Schwartz MA, Burridge K, Firtel RA, Ginsberg MH, Borisy G, Parsons JT, & Horwitz AR (2003) Cell migration: integrating signals from front to back. *Science* 302(5651):1704-1709.
- 367. Wary KK, Mainiero F, Isakoff SJ, Marcantonio EE, & Giancotti FG (1996) The adaptor protein Shc couples a class of integrins to the control of cell cycle progression. *Cell* 87(4):733-743.
- 368. Benecke BJ, Ben-Ze'ev A, & Penman S (1978) The control of mRNA production, translation and turnover in suspended and reattached anchorage-dependent fibroblasts. *Cell* 14(4):931-939.
- 369. Chicurel ME, Singer RH, Meyer CJ, & Ingber DE (1998) Integrin binding and mechanical tension induce movement of mRNA and ribosomes to focal adhesions. *Nature* 392(6677):730-733.
- 370. Farmer SR, Ben-Ze'av A, Benecke BJ, & Penman S (1978) Altered translatability of messenger RNA from suspended anchorage-dependent fibroblasts: reversal upon cell attachment to a surface. *Cell* 15(2):627-637.
- 371. Gschwind R, Umbricht CB, Torhorst J, & Oberholzer M (1986) Evaluation of shape descriptors for the morphometric analysis of cell nuclei. *Pathol Res Pract* 181(2):213-222.

8 CURRICULUM VITA

MATTHEW DAVID TREISER

treiser@rci.rutgers.edu

EDUCATION

RUTGERS, THE STATE UNIVERSITY OF NEW JERSEY, New Brunswick, NJ
Doctor of Philosophy in Biomedical Engineering: Degree Received Oct. 2009

COLUMBIA UNIVERSITY IN THE CITY OF NEW YORK, New York, NY
Bachelor of Science in Chemical Engineering with Concentration in Biomedical Engineering: Degree Received May 2003

EXPERIENCE

RUTGERS UNIVERSITY, THE STATE UNIVERSITY OF NEW JERSEY,
 BIOMEDICAL ENGINEERING DEPARTMENT, New Brunswick, NJ
Graduate Fellow: 2005 - present

UNIVERSITY OF MEDICINE AND DENTISTRY OF NEW JERSEY, ROBERT
 WOOD JOHNSON MEDICAL SCHOOL, Piscataway, NJ
Medical Student: 2003 - present

PUBLICATIONS

1. Johnson, P.A., A. Luk, A. Demtchouk, H. Patel, H.J. Sung, M.D. Treiser, S. Gordonov, L. Sheihet, D. Bolikal, J. Kohn, and P.V. Moghe, *Interplay of Anionic Charge, Poly(ethylene glycol), and Iodinated Tyrosine Incorporation within Tyrosine-derived Polycarbonates: Effects on Vascular Smooth Muscle Cell Adhesion, Proliferation and Motility*. Journal of Biomedical Materials Research: Part A, in press.
2. Liu, E., M.D. Treiser, H. Patel, H.J. Sung, K.E. Roskov, J. Kohn, M.L. Becker, and P.V. Moghe, *High-content profiling of cell responsiveness to graded substrates based on combinatorially variant polymers* Combinatorial Chemistry and High-throughput Screening - Special Issue on Combinatorial and High-Throughput Screening of Cell Response to Biomaterials, 2009. **12**(6).
3. Sung, H.J., P. Chandra, M.D. Treiser, E. Liu, C.P. Iovine, P.V. Moghe, and J. Kohn, *Synthetic polymeric substrates as potent pro-oxidant versus anti-oxidant regulators of cytoskeletal remodeling and cell apoptosis*. J Cell Physiol, 2009. **218**(3): p. 549-57.

4. Briggs, T., M.D. Treiser, P.F. Holmes, J. Kohn, P.V. Moghe, and T.L. Arinzeh, *Osteogenic differentiation of human mesenchymal stem cells on poly(ethylene glycol)-variant biomaterials*. J Biomed Mater Res A, 2008.
5. Liu, E., M.D. Treiser, P.A. Johnson, P. Patel, A. Rege, J. Kohn, and P.V. Moghe, *Quantitative biorelevant profiling of material microstructure within 3D porous scaffolds via multiphoton fluorescence microscopy*. J Biomed Mater Res B Appl Biomater, 2007. **82**(2): p. 284-97.
6. Treiser, M.D., E. Liu, R.A. Dubin, H.J. Sung, J. Kohn, and P.V. Moghe, *Profiling cell-biomaterial interactions via cell-based fluororeporter imaging*. Biotechniques, 2007. **43**(3): p. 361-6, 368.
7. Sit, P.S., D. Bolikal, J.H. Melman, M.D. Treiser, and J. Kohn, *Surface modification with a new silanated tetraethylene glycol for biotechnological applications*. Abstracts of Papers of the American Chemical Society, 2004. **227**: p. U841-U841.